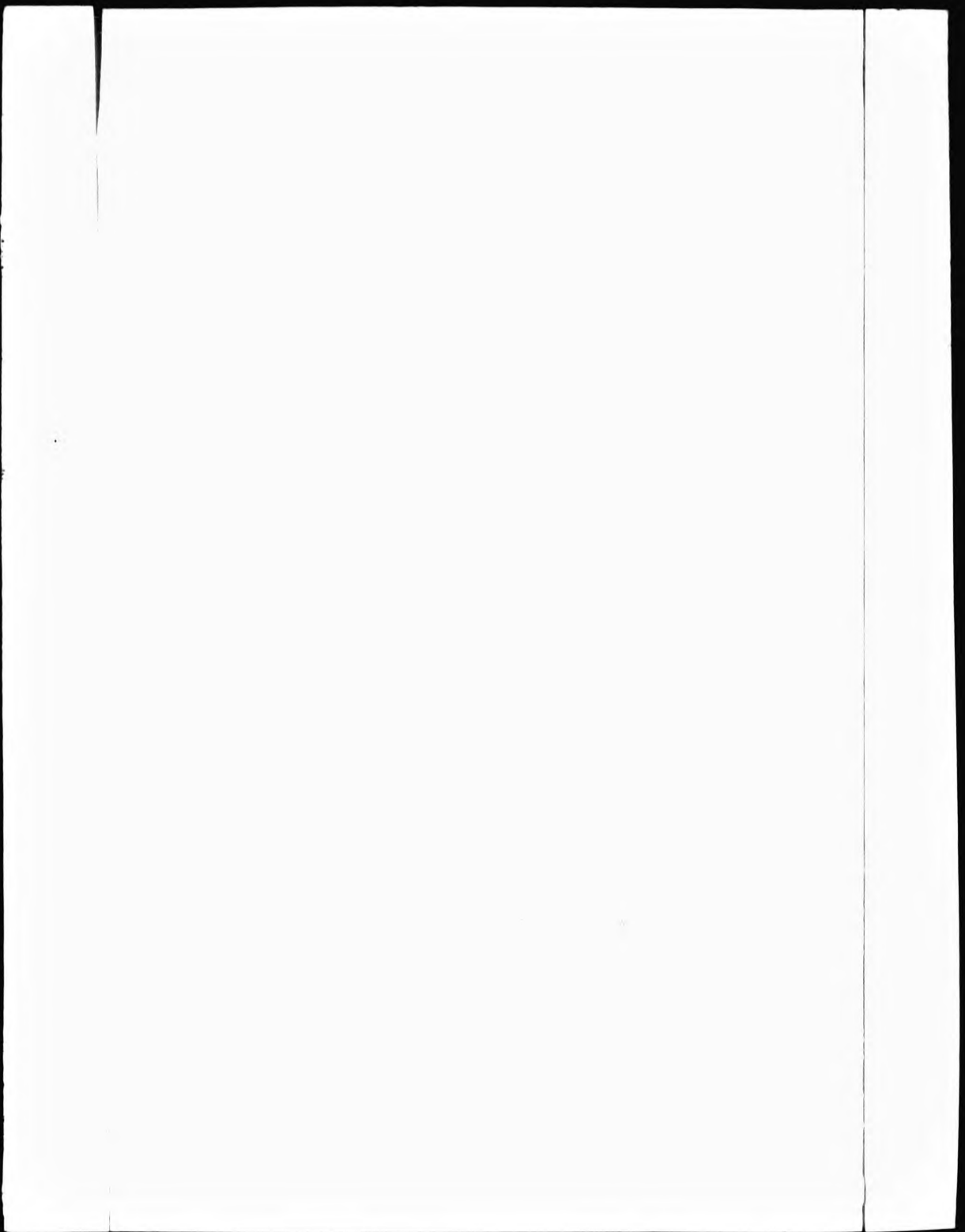
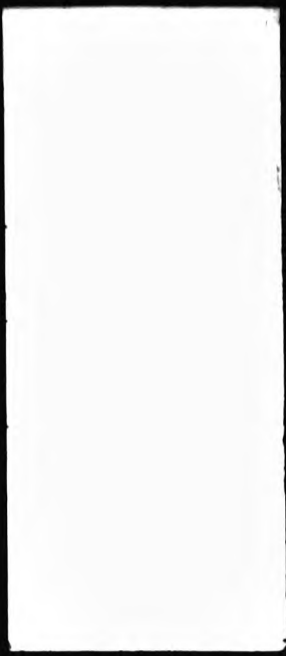


This PDF was created from the British Library's microfilm copy of the original thesis. As such the images are greyscale and no colour was captured.

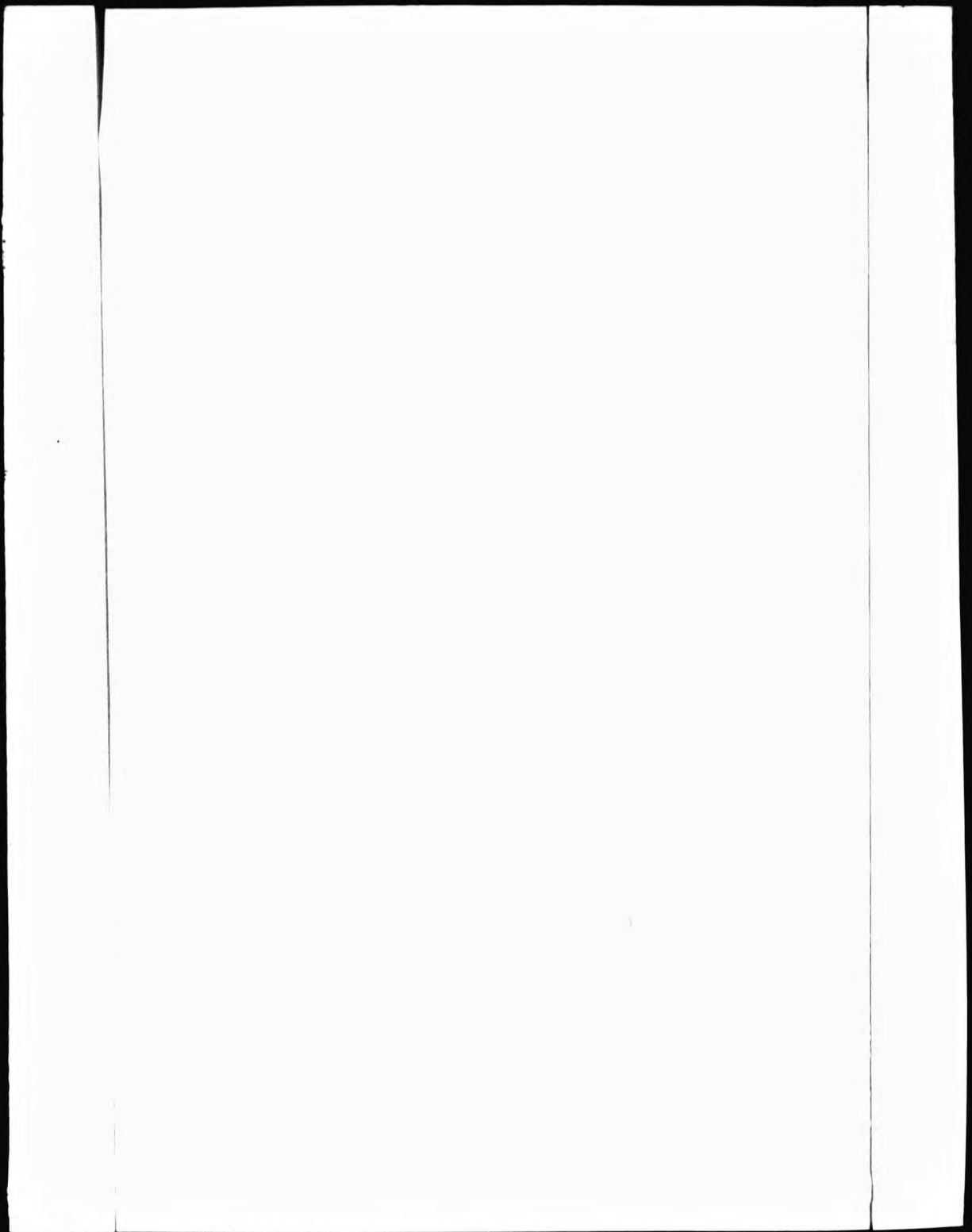
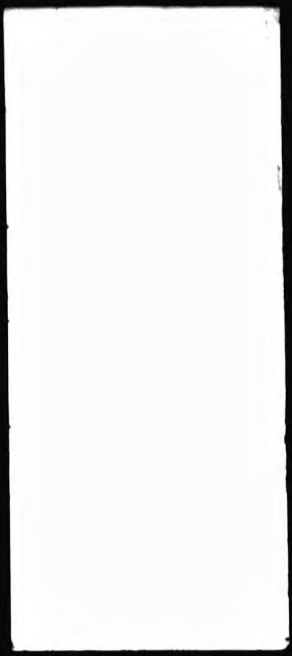
Due to the scanning process, an area greater than the page area is recorded and extraneous details can be captured.

This is the best available copy



DX

96117



THE BRITISH LIBRARY DOCUMENT SUPPLY CENTRE

TITLE

AN EXPERIMENTAL INVESTIGATION OF DIFFUSE OPTICAL
SCATTERING FROM STATIONARY AND FLOWING DISPERSIONS

AUTHOR

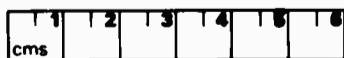
Peter Robert Wood

INSTITUTION
and DATE

City of London Polytechnic
London EC3 1991. C.N.A.A

Attention is drawn to the fact that the copyright of
this thesis rests with its author.

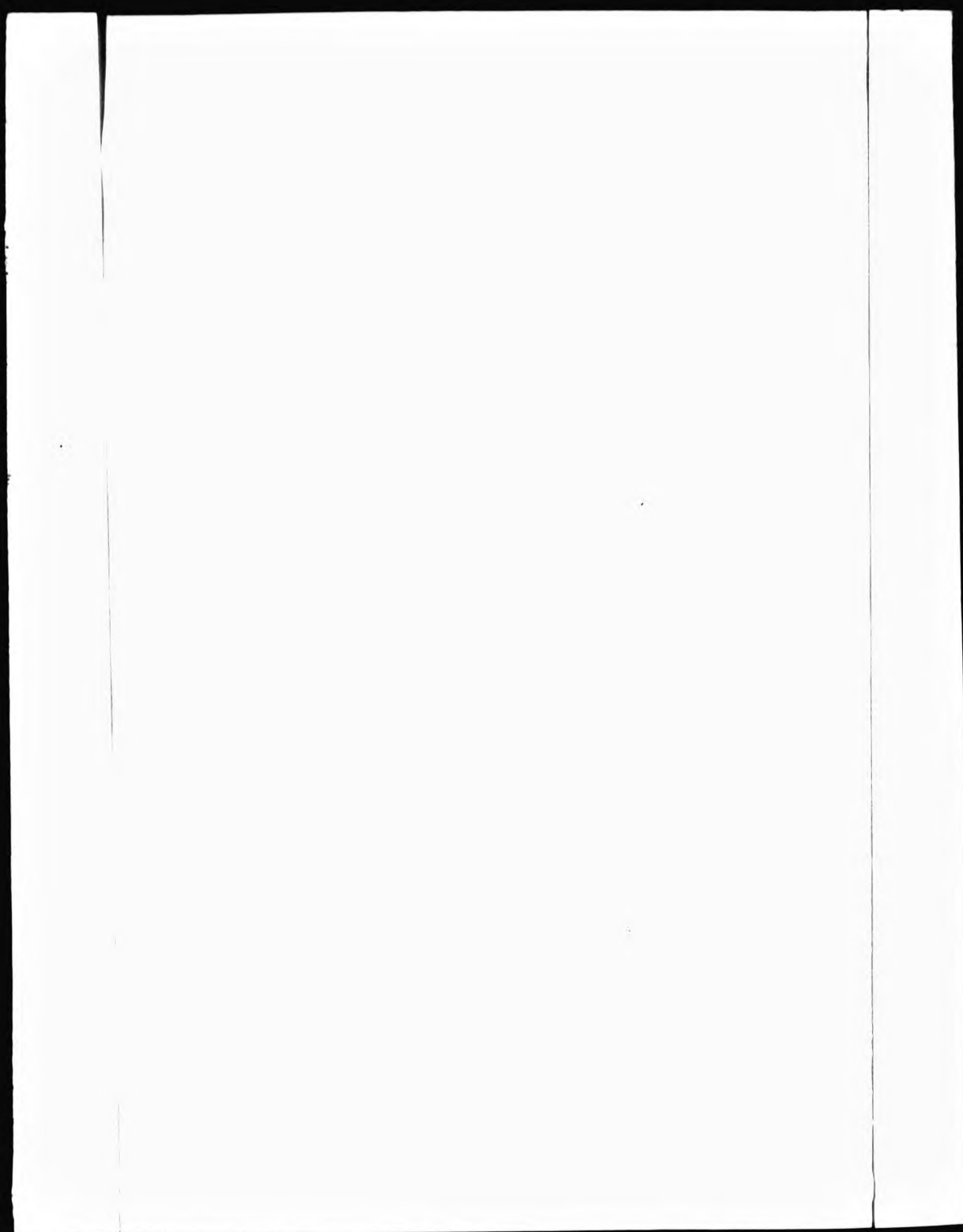
This copy of the thesis has been supplied on condition
that anyone who consults it is understood to recognise
that its copyright rests with its author and that no
information derived from it may be published without
the author's prior written consent.



THE BRITISH LIBRARY
DOCUMENT SUPPLY CENTRE
Boston Spa, Wetherby
West Yorkshire
United Kingdom

REDUCTION X 20

CAMERON 2.



AN EXPERIMENTAL INVESTIGATION OF DIFFUSE OPTICAL
SCATTERING FROM STATIONARY AND FLOWING DISPERSIONS

by

Peter Robert Wood

A thesis submitted in partial fulfilment of the CNAA degree of
Doctor of Philosophy
City of London Polytechnic

June 1991

Department of Physics
City of London Polytechnic
London EC3

THE BRITISH LIBRARY DOCUMENT SUPPLY CENTRE

BRITISH THESES NOTICE

The quality of this reproduction is heavily dependent upon the quality of the original thesis submitted for microfilming. Every effort has been made to ensure the highest quality of reproduction possible.

If pages are missing, contact the university which granted the degree.

Some pages may have indistinct print, especially if the original pages were poorly produced or if the university sent us an inferior copy.

Previously copyrighted materials (journal articles, published texts, etc.) are not filmed.

Reproduction of this thesis, other than as permitted under the United Kingdom Copyright Designs and Patents Act 1988, or under specific agreement with the copyright holder, is prohibited.

THIS THESIS HAS BEEN MICROFILMED EXACTLY AS RECEIVED

**THE BRITISH LIBRARY
DOCUMENT SUPPLY CENTRE
Boston Spa, Wetherby
West Yorkshire, LS23 7BQ
United Kingdom**

An Experimental Investigation of Diffuse Optical
Scattering from Stationary and Flowing Dispersions

Peter R. Wood

Abstract

This Thesis describes the measurement and interpretation of diffuse optical scattering from concentrated colloidal dispersions. Novel measurement techniques using optical fibres are investigated. These are applied to monodisperse spherical latexes where the results are compared with theories of radiative transport, and also to plate-like kaolinite particles where non-random particle orientation by shear flow is studied at small and large Reynolds number.

For the spherical latex dispersions various fibre configurations are investigated, the results being compared with multiple scattering predictions of the inverse scattering length S . All configurations give values of S which show the theoretical particle size dependence, but the single fibre bundle gives S in good absolute agreement with that calculated from an accepted approximate solution to the radiative transport equation. Comparisons of S between the single fibre bundle and the conventional integrating sphere method show good agreement, but only after making large specular reflectance corrections in the latter case. Measurements made on latex volume fractions (v) up to 0.4 showed a maximum in S at about $v = 0.2$, interpreted as non-random destructive interference between ordered particles.

For the kaolinite dispersions S is measured as a function of shear rate, volume fraction, particle size, pH and deflocculant concentration. Using the anomalous diffraction and Rayleigh-Gans light scattering approximations, calculations are given which support a mode of particle orientation expected below the critical Reynolds number from the particle hydrodynamics over a wide range of rotational Peclet number. The results for concentric cylinder flow above the critical Reynolds number are explicable in terms of Taylor vortices. The shear-induced changes in S in laminar flow are shown to be a useful practical measure of the state of flocculation of the dispersion.

Acknowledgements

I would like to thank my supervisors, Dr. G.H. Meeten and Dr. J.V. Champion for their unceasing help, support and encouragement throughout the course of this work. In addition I would like to thank Dr. N.E. Sherman and Mr. S. Dodd for their interesting discussions.

I would also like to thank Dr. Mohammadi of Unilever for providing highly concentrated monodisperse latex dispersions, and Dr. L. Gate of English China Clays for providing all the kaolinite samples used in this investigation and for many useful discussions.

Finally I would like to thank my family and in particular Miss Valerie Driver for their support and the City of London Polytechnic for the research assistantship whilst conducting this work.

CONTENTS.

CHAPTER 1: INTRODUCTION.

(1.1) Introduction.	1
(1.2) The scattering process.	2
(1.2.1) Light scattering from groups of particles.	3
(1.2.2) Single, multiple and dependent scattering.	4
(1.2.3) Extinction, scattering, absorption and asymmetry parameters.	6
(1.3) Scattering samples.	8
(1.3.1) Latex samples.	8
(1.3.2) Kaolinite clay samples.	9

CHAPTER 2: THEORY.

(2.1) Introduction.	13
(2.2) Mie theory.	13
(2.3) Multiple scattering theories.	23
(2.3.1) Introduction.	23
(2.3.2) Kubelka-Munk theory.	24
(2.3.3) Radiative transfer theory.	31
(2.3.4) Comparison of radiative transfer theory with Kubelka-Munk theory.	35
(2.3.5) Four-Flux theory.	39
(2.3.6) Photon diffusion theory.	41
(2.3.7) Comparison of multiple scattering theories.	43

CHAPTER 3: BIFURCATED OPTICAL FIBRE MEASUREMENT OF S.

(3.1) Experimental system.	47
(3.2) Initial experiments.	51
(3.3) S as a function of particle size.	54
(3.4) S as a function of sample concentration.	58
(3.5) Experiments with fibres of different numerical aperture.	61
(3.6) Conclusion.	67

(3.7) Discussion.	68
(3.7.1) Effect of non-isotropic scattering.	68
(3.7.2) Effect of sample geometry.	69
(3.7.3) Effect of non-diffuse illumination.	70
(3.7.4) Interfacial reflections.	74

CHAPTER 4: SINGLE OPTICAL FIBRE EXPERIMENTS.

(4.1) Introduction.	76
(4.2) Fixed path length, separate fibre system.	76
(4.2.1) Results.	78
(4.2.2) Analysis of Results.	79
(4.2.3) Conclusion.	82
(4.3) Variable path length, separate fibre system.	82
(4.3.1) Results.	84
(4.3.2) Conclusion.	89

CHAPTER 5: SINGLE OPTICAL FIBRE BUNDLE AND BEAMSPLITTER EXPERIMENTS.

(5.1) Large diameter bundle.	90
(5.1.1) S as a function of particle size.	93
(5.1.2) S as a function of concentration.	95
(5.2) Small diameter bundle.	97
(5.2.1) S as a function of particle size.	98
(5.3) Conclusion.	98

CHAPTER 6: THE INTEGRATING SPHERE.

(6.1) Introduction.	100
(6.2) Experimental method.	103
(6.3) Results.	105
(6.4) Conclusion.	108

CHAPTER 7: ABSORPTION MEASUREMENTS.

(7.1) Introduction.	109
(7.2) Initial experiments.	109
(7.3) Absorption measurements on scattering samples.	113

(7.4) Absorption measurements on non-scattering samples.	116
(7.5) Conclusion.	119

CHAPTER 8: CONCENTRATION EFFECTS.

(8.1) Introduction.	121
(8.2) Experimental procedure.	122
(8.3) Results.	122
(8.4) Analysis of results.	127
(8.5) Discussion.	133
(8.6) Conclusion.	135

CHAPTER 9: FLOW EFFECTS IN CONCENTRATED COLLOIDAL SYSTEMS.

(9.1) Introduction.	137
(9.1.1) Kaolinite clay samples.	140
(9.1.2) Previous multiple scattering rheo-optical measurements.	140
(9.1.3) Aims of rheo-optical experiments.	144
(9.2) Slot-flow cell.	146
(9.2.1) Spherical latex samples.	150
(9.2.2) Kaolinite samples.	156
(9.2.3) Flocculation detection.	164
(9.2.4) Flocculation induced by pH adjustment.	164
(9.2.5) Flocculation induced by Dispex dose adjustment.	166
(9.3) Concentric cyclinder shear cell.	170
(9.3.1) Spherical latex samples.	174
(9.3.2) Broad size fraction kaolinite samples.	177
(9.3.3) Concentration dependence.	185
(9.3.4) Fractionated kaolinite samples.	186
(9.3.5) Conclusion.	197

CHAPTER 10: DISCUSSION AND CONCLUSION.

(10.1) Overview of investigation.	199
(10.2) Conclusions.	204
(10.2.1) Spherical and randomly orientated particles.	204
(10.2.2) Shear orientated kaolinite particles.	206

APPENDIX I: Calculation of Mie scattering coefficients.	208
APPENDIX II: Internal diffuse reflectance of a window.	216
APPENDIX III: Calculation of asymmetry parameter of kaolinite particles from Rayleigh-Gans theory.	220
APPENDIX IV: Calculation of scattering cross- section of kaolinite particles from Anomalous diffraction theory.	223
References.	226

CHAPTER 1: INTRODUCTION.

(1.1) Introduction.

Single scattering from dilute dispersions of spherical particles is well characterized theoretically. The majority of the optical experimental work carried out on colloidal dispersions has been confined to this regime. Little quantitative work has been done on well-characterized concentrated samples where the observed light can be considered to have undergone more than one scattering event. This is an area of considerable practical importance in for example paints or food, where the appearance of the sample is of prime importance. Such a sample will not be described using single scattering theory.

The work in this thesis investigates new methods of measuring multiple scattering in samples using incoherent optical fibres. The agreement between experiment and theory is investigated by the use of well-characterized samples, (i.e. monodisperse spherical particles of known size, illuminated by monochromatic light), and by making comparisons between the optical fibre methods and the classical integrating sphere method. In the latter part of the investigation it is shown that optical fibres can be usefully employed to measure flow-orientational effects in concentrated non-spherical colloidal dispersions.

(1.2) The scattering process.

When an obstacle such as an atom, molecule, solid or liquid particle is illuminated by an electro-magnetic wave, electric charges within the object are set in oscillatory motion by the electric field of the incident wave. The accelerated electric charges emit electro-magnetic energy. This secondary radiation is termed the scattered radiation. The particle may also convert some of the incident energy into another form, such as heat. This process is known as absorption. The interaction between the incident wave and scattering particle may therefore be seen as a purely electro-magnetic phenomena, and hence can in principle be characterized by the application of Maxwell's laws [1]. In practice the application of Maxwell's laws to the interaction of radiation with particles, of even simple geometries, leads to solutions that are highly complex [2,3]. It has only recently proved possible with the advent of cheap and fast computing, to evaluate the solutions to these equations quickly and easily within the laboratory. Previous to this tabulated results had to be used to provide reasonable approximations to the actual scattering sample. The application of Maxwell's laws to the interaction of an electro-magnetic wave and a single spherical particle, (widely known as Mie theory [3]), has proved highly successful for single scattering calculations.

However, Mie theory only considers a single particle illuminated by monochromatic radiation: an idealised situation which is rarely achieved in situations of practical importance,

where the scattering particles may be such that the mean free path length of a photon within the sample is very much less than the sample thickness. An understanding of the scattering processes involved in these materials is highly desirable. It is the scattering and absorption of light that determines the appearance of the material.

(1.2.1) Light scattering from groups of particles.

Mie theory can be applied to groups of particles so long as the following conditions are fulfilled:

- (a) The particles are of known size (or size distribution), and known refractive index.
- (b) The mean free path length of a photon within the sample is significantly greater than the thickness of the sample under consideration. (The thickness of a sample being the distance within the sample between the illuminating source and the observer).
- (c) The particles are randomly positioned, or alternatively are such that the repeat distance is longer than the coherence length of the illuminating radiation.
- (d) The average separation of the time averaged positions of the particles is greater than the coherence length of the illuminating radiation.

Condition (a) arises from the simple consideration that we

must know what we are looking at to be able to predict what will happen. Condition (b) ensures that the majority of light will have been scattered once and once only, i.e. the sample under consideration is dominantly single scattering. Conditions (c) and (d) ensure that no instantaneous coherent phase relationship between light scattered by differing particles will exist, i.e. light scattered from one particle will not in general interfere either constructively or destructively with light scattered from another. Under these conditions the applications of Mie theory is relatively straight-forward, and hence Mie theory can be easily applied to optically thin samples with large interparticle separations.

However, single particle (Mie) theory is inapplicable to optically thick samples, where a large proportion of the observed scattered light has undergone more than one scattering event, and to samples where interference effects between light scattered by neighbouring particles becomes important. It is important here to distinguish between these three types of scattering.

(1.2.2) Single, multiple and dependent scattering.

Single scattering occurs when observations are made through an optically thin sample. The term optically thin is here strictly defined as meaning that the sample thickness between the source and the observer is much less than the mean free path length of a photon within the sample.

Multiple scattering is where the observed radiation can be considered to have undergone, (on average), more than one scattering event. This occurs in samples that are optically thick. The term optically thick is here strictly defined as meaning that the sample thickness between the source and the observer is much greater than the mean free path length of a photon within the sample.

Dependent scattering occurs when interference takes place between light scattered from neighbouring particles. This implies that the neighbouring particles are at a separation less than the coherence length of the scattered light. This in turn implies that the particle separation is less than the coherence length of the illuminating radiation, (the coherence length of the scattered light cannot be greater than the coherence length of the illuminating light).

Multiple scattering samples may therefore scatter light dependently or independently depending upon the coherence length of the illuminating radiation. The coherence length of the illuminating radiation is given by the expression [4],

$$\text{Coherence length} \approx \frac{\bar{\lambda}^2}{\Delta\lambda}$$

where $\bar{\lambda}$ = wavelength of illuminating radiation,

$\Delta\lambda$ = bandwidth of illuminating radiation.

The more concentrated the sample, the lower the inter-particle separation, and hence the more likely that

dependent scattering will occur. If the particles within the sample are in motion, then at some instant in time there will be particles with low enough separations for their scattered light to interfere. This will result in temporal fluctuations in the observed scattered light as the particles move together and apart within the sample. However, if the illuminated portion of the sample is large enough, or the observation time long enough, these temporal fluctuations will be averaged out.

For a brief introduction to the subject of multiple scattering see reference [5].

(1.2.3) Extinction, scattering, absorption and asymmetry parameters.

A scattering particle will remove some energy from the incident beam. If there are no particles present an observer would detect a power P . If a particle is placed between the observer and the source, the observer will now detect a power P_1 , where $P_1 < P$. We say that this drop in detected power is due to extinction of the beam. This extinction may be due to either scattering or absorption by the particle, or a combination of both. If we define W_{abs} as the amount of power absorbed by the particle, W_{ext} as the amount of power removed from the incident beam by the particle, and W_{scat} as the amount of energy scattered from the incident beam by the particle, then:

$$W_{ext} = W_{abs} + W_{scat} . \quad \dots(1.2.1)$$

The ratio of the power removed to the incident intensity, I ,

defines a quantity with units of area. The areas C_{ext} , C_{scn} and C_{abs} , (the extinction, scattering and absorption cross sections respectively), are defined as:

$$W_{ext}/I_0 = C_{ext}, \quad W_{scn}/I_0 = C_{scn} \quad \text{and} \quad W_{abs}/I_0 = C_{abs} .$$

The efficiencies for extinction, scattering and absorption are defined thus:

$$Q_{ext} = C_{ext}/A, \quad Q_{scn} = C_{scn}/A \quad \text{and} \quad Q_{abs} = C_{abs}/A ,$$

where A is the scattering particle cross-sectional area projected onto a plane normal to the direction of propagation of the incident beam. It therefore follows from equation (1.2.1) that;

$$Q_{ext} = Q_{scn} + Q_{abs}$$

The asymmetry parameter g is defined as;

$$g = \overline{\cos\theta} = \int \cos\theta p(\theta) d(\cos\theta),$$

where $p(\theta)$ optical power (for unit irradiance) scattered into a unit solid angle θ , θ being defined as the angle made by the scattered light to the forward (incident) beam direction.

The quantity $p(\theta)$ is usually termed the phase function, or the scattering diagram. The asymmetry parameter describes the angular dependence of the light scattered from the particle. If the particle scatters light equally in the forward and backward directions, g is equal to zero. If the particle scatters light more strongly in the forward direction; $0 < g < 1$, if the light is scattered more strongly in the backward direction; $0 > g > -1$.

A further useful scattering parameter Q_p is defined by,

$$Q_p = Q_{ext} - Q_{scn} \overline{\cos\theta}.$$

(1.3) Scattering Samples.

(1.3.1) Latex Samples.

Monodisperse spherical latex particles suspended in water provide a nearly ideal sample for studying multiple scattering. The low size dispersion allows for easy sample characterization. The low relative density 1.05, means that settling effects within the sample are minimized. The refractive index of the latex particles is 1.60, (manufacturer's data, at 589 nm). Latex samples used in this investigation were provided from three sources;

- (i) Polysciences U.K.,
- (ii) Sigma Chemicals,
- (iii) Unilever.

The Polysciences samples were provided at a quoted concentration of 2.5 % by weight, corresponding to a volume fraction of 0.0238. This was checked by weighing and drying of the samples. They were provided surfactant free. All the Polysciences samples had a quoted standard deviation in particle size of less than 5 %. The Sigma samples were identical to the Polysciences samples except that they were provided at a concentration of 10 % by weight, (a volume fraction of 0.096). The samples obtained from Unilever consisted of two highly concentrated samples. They were provided with a long chain polymer surfactant added to the dispersion. The exact composition of the surfactant was unknown. The Unilever samples were only used for the experimental investigation into highly concentrated scattering systems, (chapter 8).

All samples were observed to be stable, no evidence being detected for particle aggregation in fresh samples. Some settling of particles was noted for particle diameters larger than 1 micron, however agitation of the sample appeared to return the sample to normal.

(1.3.2) Kaolinite clay samples.

It is not the purpose of this text to provide a detailed account of kaolin chemistry. The reader is referred to references [6], [7] and [8] for a more complete introduction to the subject. However for the purposes of understanding the rheo-optical behaviour of the kaolinite clays a brief introduction to the subject is given here. The following text is largely indebted to Molloy [9].

Kaolin is a naturally occurring aluminium silicate clay with a two-layered crystalline structure. The unit layer consists of an octahedral sheet of oxygen and aluminium atoms linked by covalent bonds to a tetrahedral sheet of oxygen and silicon atoms. [6]. The basal spacing of kaolinite is 0.72 nm between corresponding sheets in stacked unit layers, [6]. The layers are held together by Van der Waals' forces. These being comparatively weak, cleavage of the layers will occur along the parallel planes between them. This produces the flat plate-like structure observed in electron micrographs. Kaolinite particles are approximately hexagonal platelets, they can be approximated to by flat thin discs with an aspect ratio of approximately 10:1 [8]. The charge on the

particle face is always negative [6], due to isomorphous substitution. At the edges of the kaolin particle the surface is made up of the disrupted sheets of silica and alumina. It is similar to the oxide surfaces of silica and alumina, hence the charge-determining mechanism of the edge is that of an oxide surface. Thus the edge is positively charged below pH 7 and negatively charged above pH 7. The mode of aggregation is therefore pH dependent. For low pH the particles can flocculate in a face-to-edge mode due to the interaction of oppositely charged electrical double layers. This gives rise to a 'house-of-cards' floc structure [8]. At high pH, as a result of the interaction of extended double layers, a similar 'house-of-cards' may be formed, [10]. This model accounts well for the change in viscosity with pH as observed in clay suspensions.

Measurements of the refractive index of kaolinite clay particles by differential refractometry give a value of 1.57, [9]. The optical absorption of the particles is very low. It has been reported [12] that kaolinite particles suspended in an index-matching fluid were transparent up to concentrations of 50 %. The relative density of kaolinite is 2.60.

The main sample used in this investigation (SPS grade kaolinite), were of a broad size fraction, see fig (1.3.1). The samples were provided by English China Clays, and were prepared, (unless otherwise stated), according to their instructions to achieve maximum deflocculation of the clay particles in suspension.

The clay was suspended in de-ionized water and the pH adjusted to 8.5. 0.21 % by dry weight of clay of sodium polyacrylate, (in the form of Dispex, a commercial surfactant), was then added. The samples were then thoroughly mixed, using a magnetic stirrer, for at least half an hour. The sample pH was then checked and re-adjusted to 8.5 if necessary. Each sample was then left for at least 24 hours and mixed again immediately prior to an experiment, the pH was again checked and if necessary re-adjusted to 8.5.

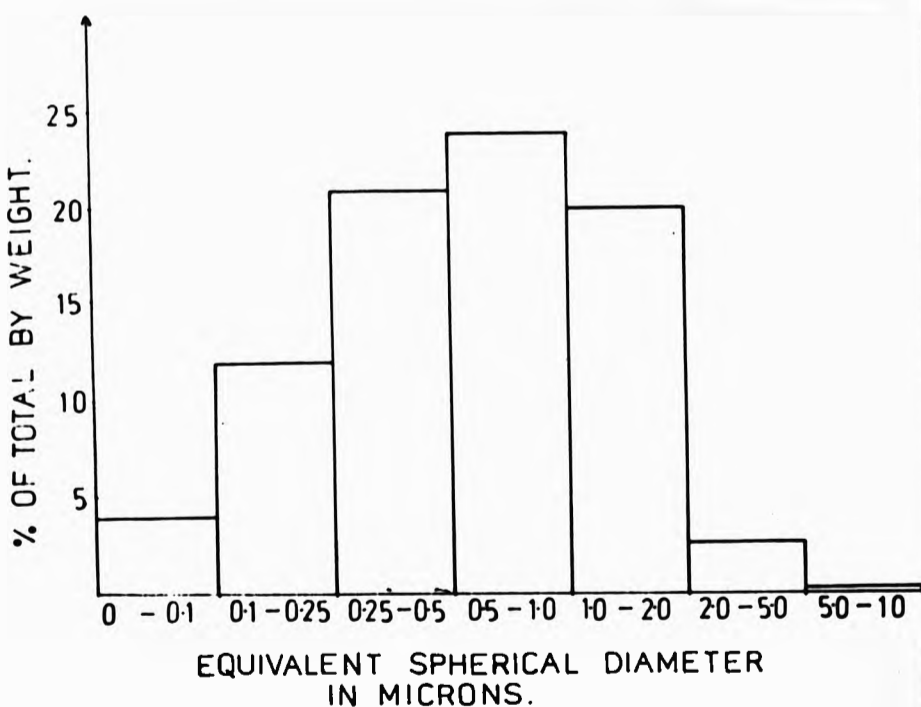


Fig (1.3.1)
Equivalent spherical diameter of kaolin particles in SPS sample. The equivalent spherical diameter is determined by measuring the settling rate of a given size fraction, and equating it to the settling rate of a spherical particle.

The large size distribution of the sample, the particle shape, and its high relative density limits the usefulness of using kaolinite clays to study multiple scattering. However, their plate-like shape, large axis ratio and low optical absorption make kaolinite useful for studying rheo-optical effects. The large axis ratio maximises the hydrodynamic forces acting upon the sample, and hence maximises the change of scattering parameter on flow. The low absorption of the sample minimises the attenuation of light. Hence the use of kaolinite is largely confined to the investigations of flow effects in concentrated colloidal systems.

CHAPTER 2: THEORY.

(2.1) Introduction.

This chapter is intended to provide a brief review of multiple scattering theory. A useful starting point for this is the single scattering theory of Mie [2,3]. Mie theory provides exact calculations of the scattering efficiencies for single particles. These prove useful in quantifying multiply scattering samples.

(2.2) Mie theory.

It is not intended to provide a rigorous derivation of Mie theory here. This is more than adequately covered elsewhere. The reader is referred to standard texts [2,3] for a full derivation. Mie theory is essentially Maxwell's laws of electro-magnetic propagation [1,4] as applied to a spherical particle. Mie theory allows the scattering properties of the particles, (Q_{ext} , Q_{ext} , Q_{abs} and g), to be evaluated from the particle size and its refractive index (relative to the surrounding medium). These properties are described by,

(a) the particle size parameter, x ,

$$x = 2\pi a / \lambda,$$

where; a = the particle radius, and

λ = the wavelength of the illuminating radiation in the continuous phase.

(b) The relative refractive index of the particle, m ,

$$m = n_1/n_2,$$

where; n_1 = the refractive index of the particle, and
 n_2 = the refractive index of the continuous phase.

If n_1 is complex then the particle is absorbing, i.e. non-absorbing particles have a real refractive index.

From Mie theory we obtain the following series summations to calculate the scattering efficiencies.

$$Q_{\text{scat}} = \frac{2}{x^2} \sum_{n=0}^{\infty} (2n+1) [|a_n|^2 + |b_n|^2] \quad \dots(2.2.1)$$

$$Q_{\text{ext}} = \frac{2}{x^2} \sum_{n=0}^{\infty} (2n+1) \text{Re}(a_n + b_n) \quad \dots(2.2.2)$$

$$Q_{\text{ext}} \cos \theta = \frac{4}{x^2} \sum_{n=0}^{\infty} \frac{n(n+2)}{n+1} \text{Re}[a_n a_n + b_n b_n] + \frac{2n+1}{n(n+1)} \text{Re}(a_n b_n) \quad \dots(2.2.3)$$

$$\text{where; } a_n = \frac{x \psi_n'(y) \psi_n(x) - y \psi_n'(x) \psi_n(y)}{x \psi_n'(y) \xi_n(x) - y \xi_n'(x) \psi_n(y)}, \quad \dots(2.2.4)$$

$$b_n = \frac{y \psi_n'(y) \psi_n(x) - x \psi_n'(x) \psi_n(y)}{y \psi_n'(y) \xi_n(x) - x \xi_n'(x) \psi_n(y)}. \quad \dots(2.2.5)$$

and $y = mx$.

The primes denote differentiation with respect to the argument.

The functions $\psi_n(x)$ and $\xi_n(x)$ are defined in terms of $J_n(z)$, the

spherical Bessel function of order n , i.e.

$$\psi_n(z) = \left(\frac{nz}{2}\right)^{1/2} J_{n+1/2}(z) \quad \dots(2.2.6)$$

and
$$\zeta_n(z) = \left(\frac{nz}{2}\right)^{1/2} [J_{n+1/2}(z) + J_{n-1/2}(z)] \quad \dots(2.2.7)$$

Also
$$\xi_n(z) = \psi_n(z) + i \chi_n(z)$$

where
$$\chi_n(z) = (-1)^n \left(\frac{nz}{2}\right)^{1/2} J_{n+1/2}(z) \quad \dots(2.2.8)$$

The factors a_n and b_n may be calculated using the expressions:

$$a_n = \frac{\left[\frac{A_n(y)}{m} + \frac{n}{x}\right] \operatorname{Re}[\zeta_n(x)] - \operatorname{Re}[\zeta_{n-1}(x)]}{\left[\frac{A_n(y)}{m} + \frac{n}{x}\right] \zeta_n(x) - \zeta_{n-1}(x)} \quad \dots(2.2.9)$$

$$b_n = \frac{\left[mA_n(y) + \frac{n}{x}\right] \operatorname{Re}[\zeta_n(x)] - \operatorname{Re}[\zeta_{n-1}(x)]}{\left[mA_n(y) + \frac{n}{x}\right] \zeta_n(x) - \zeta_{n-1}(x)} \quad \dots(2.2.10)$$

where $A_n(y) = \psi_n(y) / \psi_n'(y)$

The basic computational procedure for evaluating the scattering parameters, from m and x , is to calculate the values of ζ_n and A_n for each n from the following recurrence relationships. The quantities a_n and b_n may then be calculated, and the series summed to obtain the required scattering efficiencies. The recurrence relationships necessary to calculate A_n and ζ_n are,



$$A_n(y) = -n/y + (n/y - A_{n-1}(y)),$$

where

$$A_0(y) = \cos(y)/\sin(y),$$

and

$$\zeta_n(x) = (2n-1/x)\zeta_{n-1}(x) - \zeta_{n-2}(x)$$

where

$$\zeta_0(x) = \sin x + i \cos x,$$

$$\zeta_{-1}(x) = \cos x - i \sin x.$$

Care must be taken when calculating the efficiency factors as the recurrence relation for $\zeta_n(x)$ can become unstable for large values of n , leading to large errors [13]. It is also advisable to use a downward recurrence relation to calculate A_n [13]. Equations (2.2.1), (2.2.2) and (2.2.3) require summations to infinity, however it has been shown that the series quickly converges to a limiting value in a little over x terms [13]. It has been shown that [13] to obtain 4 figure accuracy the number of terms required is approximately $x + 4x^{1/3} + 2$.

A double precision Fortran programme was written to evaluate the scattering efficiencies, the programme coding is given in appendix I.

The values of Q_{ext} , Q_{pr} and $\overline{\cos\theta}$ calculated by the programme were initially compared with the tabulated values of Wickramasinghe [14]. Wickramasinghe gives tabulated values of Q_{ext} , Q_{pr} and $\overline{\cos\theta}$ (for both absorbing and non-absorbing spheres), for values of m ranging from 1.1 to 2.0 and values of x ranging from 0.1 to 15.0. It was noted that excellent agreement between the programme results and the tabulated values of Wickramasinghe was obtained for all Q_{ext} values. However, large discrepancies were observed between the tabulated and computed values of Q_{pr} and $\overline{\cos\theta}$.

Careful checking revealed no coding or theoretical error in the programme. Comparisons of values of $\overline{\cos\theta}$ and Q_{pr} were made with those of other authors. These were; Blevin and Brown [15], Brinkworth [16], Irvine [17,18] and Mehta [19]. In all cases excellent agreement was noted for all values of Q_{sm} , Q_{pr} and $\overline{\cos\theta}$. (The values of m in the published values ranges from 1.2 to 2.4. The values of x ranges from 0.2 to 2.4). It was therefore concluded that the programme was correct. It follows that Wickramasinghe's values of Q_{pr} and $\overline{\cos\theta}$ are incorrect. There follows a brief explanation as to the meaning of Wickramasinghe's values.

The asymmetry parameter $\overline{\cos\theta}$ (frequently denoted by g), is defined as [3],

$$\overline{\cos\theta} = \int_{-1}^1 \cos\theta p(\theta) d(\cos\theta), \quad \dots(2.2.11)$$

where $p(\theta)$ = the phase function of the scattering particle,
 = the optical power (for unit irradiance) scattered into a unit solid angle about a given direction θ , θ being the angle between the scattered light and the incident beam.

$p(\theta)$ is normalized such that,

$$\int_{-1}^1 p(\theta) d(\cos\theta) = 1 \quad \dots(2.2.12)$$

The quantities Q_{pr} and $\overline{\cos\theta}$ are related (by definition) to the normalized scattering and extinction cross-sections Q_{sm} and Q_{ext} by the equation [3],

$$Q_{pr} = Q_{ext} - Q_{sm} \overline{\cos\theta} \quad \dots(2.2.13)$$

For non-absorbing particles this simplifies to,

$$Q_{pr} = Q_{sca}(1 - \overline{\cos\theta}), \quad \dots(2.2.14)$$

as

$$Q_{ext} = Q_{sca}.$$

It is instructive here to consider the scattered radiation from large spheres. From Van de Hulst [3] the following table is reproduced. It separates the contributions to Q_{ext} , Q_{sca} and $\overline{\cos\theta}$ into that from scattered light and that from diffracted light.

	Diffracted Light	Reflected & Refracted	Both
Q_{ext}	1	1	2
Q_{sca}	1	w	1+w
$\overline{\cos\theta}$	1	g_r	$(1+wg_r)/(1+w)$

Where; w = the albedo, or whiteness of the particle,

g_r = the value of $\overline{\cos\theta}$ when diffraction effects are excluded.

Substituting the values of Q_{ext} , Q_{sca} and $\overline{\cos\theta}$ from the above tables for both diffraction and scattering, we obtain from (2.2.13),

$$Q_{pr} = 1 - wg_r. \quad \dots(2.2.15)$$

If we now perform the same operation, but exclude the diffracted contribution we obtain,

$$Q_{pr} = 1 - wg_r. \quad \dots(2.2.16)$$

Equations (2.2.15) and (2.2.16) are identical, it therefore follows that the diffracted contribution to the value of Q_{pr} is zero. It follows from the previous table that for very large, non-absorbing particles, (i.e. $x \gg 1$ and $w=1$),

$$\begin{aligned} \overline{\cos\theta} &= (1+g_r)/2 \\ g_r &= 2\overline{\cos\theta} - 1 \end{aligned} \quad \dots(2.2.17)$$

Comparisons of $\overline{\cos\theta}$ as calculated by the programme given in appendix I and those tabulated by Wickramasinghe, for large non-absorbing particles, to a good approximation, agree with equation (2.2.17) when g is replaced by the Wickramasinghe value of $\overline{\cos\theta}$. It would therefore appear that Wickramasinghe has calculated his value of $\overline{\cos\theta}$ neglecting the contributions from diffraction. This is not stated in his text. He states that his value of $\overline{\cos\theta}$ is calculated from the expression,

$$\overline{\cos\theta} = \frac{4}{Q_{\text{scat}}} \sum_{n=0}^{\infty} \frac{n(n+2)}{(n+1)} \text{Re} [a_n a_{n+1} + b_n b_{n+1}] + \frac{2n+1}{n(n+1)} \text{Re} [a_n b_n]$$

This expression is identical to that used to calculate $\overline{\cos\theta}$ by the Fortran programme. This is inconsistent with his results.

In summary then it would appear that Wickramasinghe has excluded the diffraction contribution to $\overline{\cos\theta}$ in his tabulated values. This contribution has not been excluded from his values of Q_{scat} , the resulting computation of Q_{pr} using these two values is therefore incorrect. It can be seen from the fact that equations (2.2.15) and (2.2.16) are identical that Q_{pr} may be calculated from values of Q_{scat} and $\overline{\cos\theta}$ either both including or both excluding the diffraction contributions. However neglecting the contribution in either Q_{scat} or $\overline{\cos\theta}$ and then including it in the other will lead to incorrect computations of Q_{pr} . This would appear to be Wickramasinghe's error.

Figs (2.1.1), (2.1.2) and (2.1.3) illustrate the calculated values of Q_{scat} , Q_{pr} and $\overline{\cos\theta}$ (respectively) as a function of particle

size for a relative refractive index of 1.2 and no absorption.

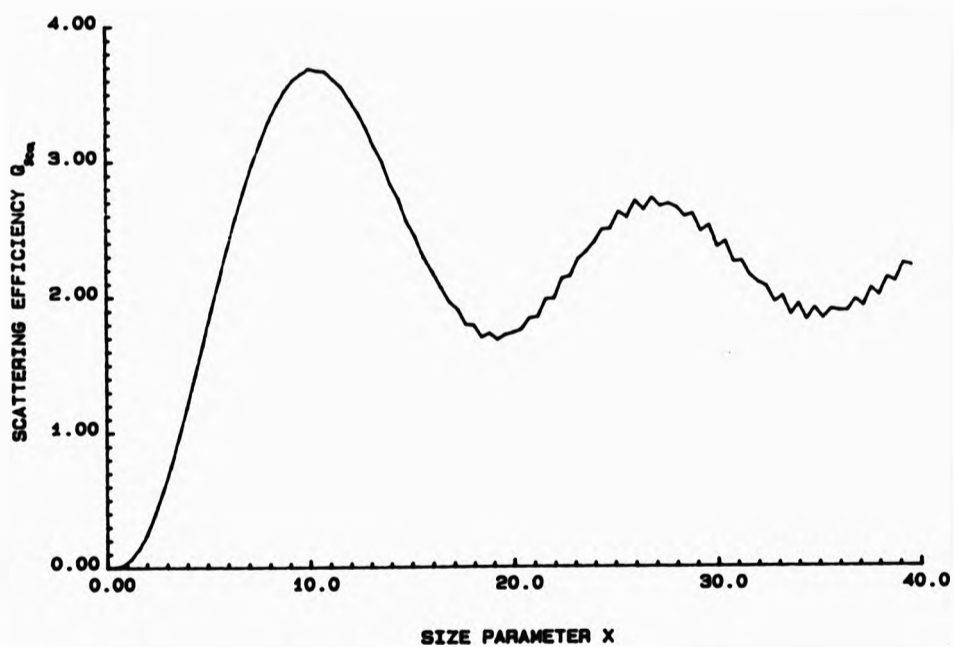


Fig (2.2.1)
 Q_{sca} as a function of particle size.
Relative refractive index = 1.20.

The 'scatter' of points evident in fig (2.2.1) for $x > 15$ is in fact due to a low amplitude ripple in Q_{sca} . This has been widely reported elsewhere (2,3,13,14).

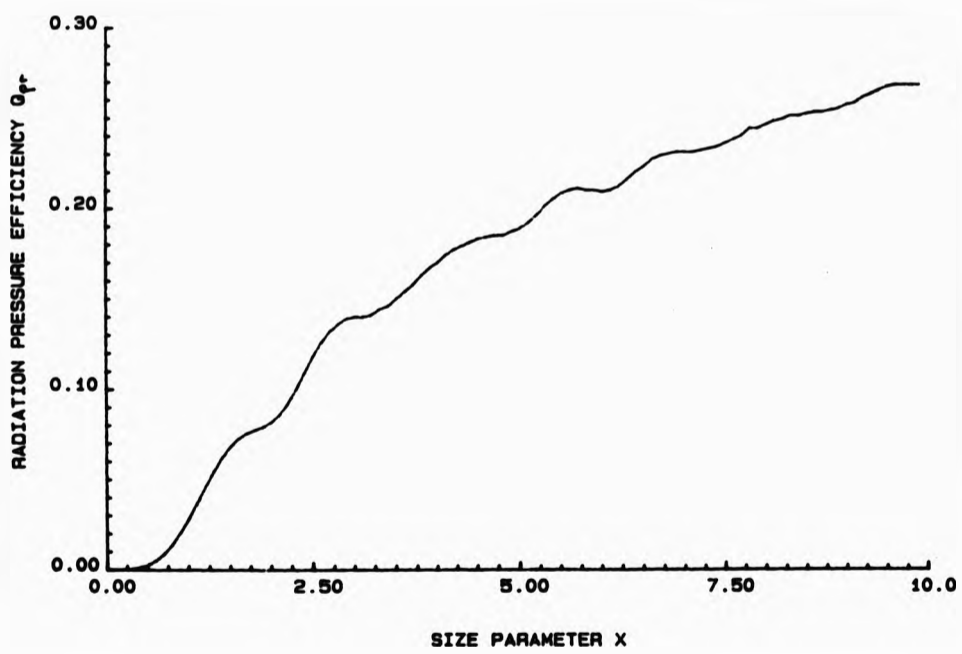


Fig (2.2.2)
 Q_{pr} as a function of particle size.
Relative refractive index = 1.20.

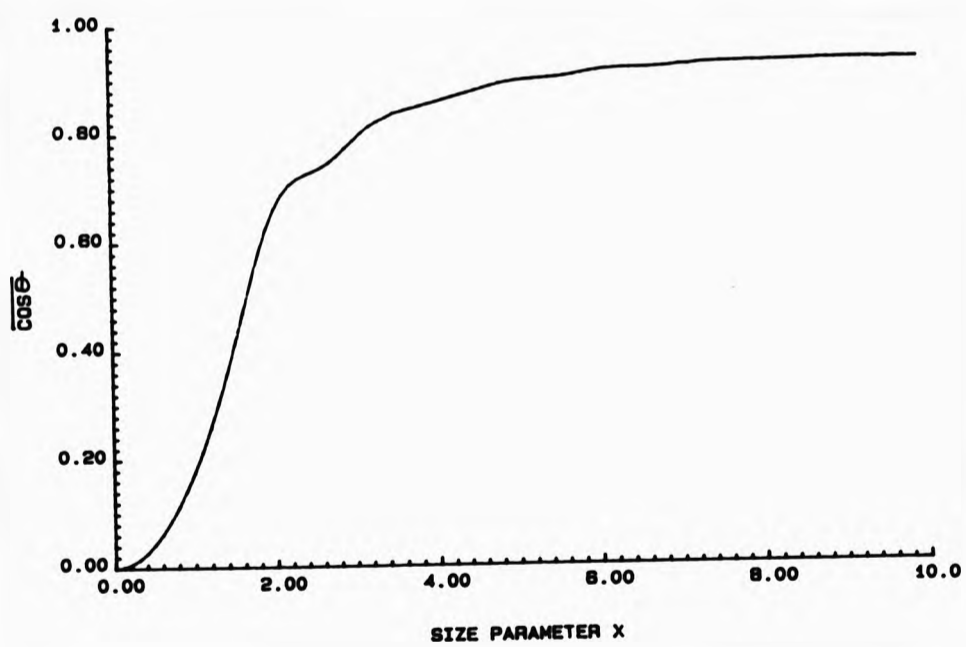


Fig (2.2.3)
 $\overline{\cos\theta}$ as a function of particle size.
Relative refractive index = 1.20.

(2.3) Multiple scattering theories.

(2.3.1) Introduction.

The scattering properties of a sample are determined by the scattering efficiencies of the constituent particles, (i.e. how much incident light is scattered by the particles), and the angular dependence of the scattered light, (i.e. how 'scattered' is the scattered light). These quantities can be determined for particles in the single scattering regime from Mie theory. It is highly desirable that the exact nature of the relationship between the scattering power of a sample, and the scattering efficiency and scattering asymmetry, be discovered. Some advances have been made in this area by Brinkworth [20], and others [21,22,23]. There still remains the question as to whether these quantities may be calculated from single scattering theories, and if so over what range of particle separations it is valid to do so.

The following text presents some multiple scattering theories, and by comparison of them, seeks to find a suitable method of determining the scattering power of a sample from a knowledge of the constituent particle properties.

Recently some work has been done using highly mathematically complex [24,25,26] or computationally intensive [27,28,29] models to describe multiple scattering in particular situations. These models are not considered here as they are not particularly instructive, and do not aid an intuitive understanding of the multiple scattering

process due to their specific nature.

(2.3.2) Kubelka-Munk theory.

The Kubelka-Munk theory [30,31] is widely used in the paints and coatings industry to evaluate the scattering properties of materials [32,33,34]. Its wide use stems from its ease of calculation and its relatively good agreement with experimental results. The theory assumes that light is scattered isotropically by the particles, and that the scattering sample may be characterized using only two parameters, the absorption coefficient K , and the scattering coefficient S . The use of only two parameters to characterize a sample makes the theory simple to manipulate and evaluate in comparison with many other multiple scattering theories, but it must also be in error when applied to samples that differ from the ideal of perfectly isotropic scatterers.

We shall consider a parallel sided layer of material that is infinite in lateral extent and of finite thickness, illuminated by an isotropic diffuse flux over the whole extent of one of the parallel faces. The material is considered to be perfectly homogeneous, in that the inhomogeneities necessarily present for scattering to take place are negligibly small in comparison with dimensions of the system. There are assumed to be two oppositely travelling diffuse fluxes within the sample. One of these fluxes travels in the forward direction, (in the direction of the illuminating flux), the other in the backward direction. These fluxes are denoted by the symbols i and j respectively. It is

assumed that in traversing a thickness dz of sample that the forward and backward fluxes are reduced by an amount $iKdz$ and $jKdz$ respectively due to absorption. This defines the absorption coefficient K . Similarly, the forward and backward fluxes are reduced by an amount $iSdz$ and $jSdz$ respectively due to scattering of the diffuse fluxes. This defines the scattering coefficient S .

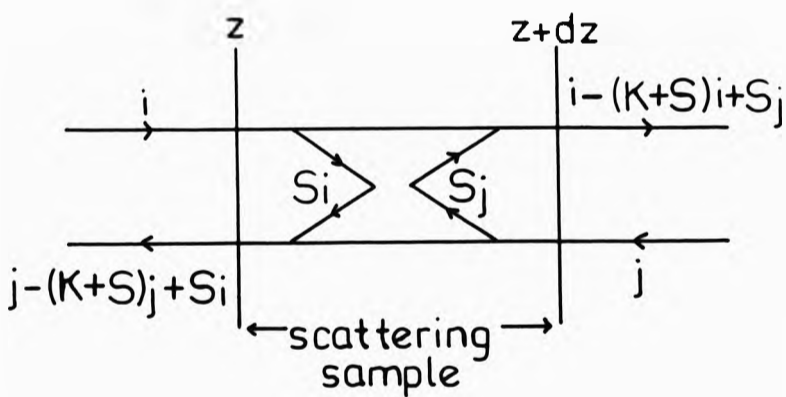


Fig (2.3.1)
Forward and backward diffuse fluxes
traversing a sample thickness dz .

Considering the change in the forward flux i , in traversing a thickness dz of sample

$$di = -iKdz - iSdz + jSdz , \quad \dots(2.3.1)$$

and similarly for the backward flux j

$$-dj = -jKdz - jSdz + iSdz . \quad \dots(2.3.2)$$

Solving these equations simultaneously gives,

$$i'' - (K(K+2S))i = 0 ,$$

and

$$j'' - (K(K+2S))j = 0 ,$$

where the primes denote differentiation with respect to z .

$$\text{Hence, } j = C_1 \exp(\alpha z) + C_2 \exp(-\alpha z) \quad \dots(2.3.3)$$

$$\text{and } i = C_3 \exp(\alpha z) + C_4 \exp(-\alpha z), \quad \dots(2.3.4)$$

where; $\alpha = \sqrt{K(K+2S)}$, $C_1 = C_2(\alpha-K)/(\alpha+K)$ and $C_3 = C_4(\alpha+K)/(\alpha-K)$.

This gives the general solutions for the two fluxes within the sample. To obtain a particular solution we must apply the appropriate boundary conditions. As the formation of the Kubelka-Munk equations envisages a one-dimensional problem it is necessary to apply one-dimensional boundary conditions, i.e. the sample is considered to be infinite in lateral extent, the boundary conditions may not vary over this extent. Suitable boundary conditions are that;

(a) the sample is illuminated by a constant forward flux i_0 , along one boundary over the whole of its lateral extent and,

(b) the sample is backed by an absorbing plane surface at a distance d from the first boundary.

Expressing these boundary conditions mathematically; (a) at $z=0$ $i=i_0$, (b) at $z=d$ $j=0$. Hence the following equations for C_1 and C_2 are obtained;

$$C_1 = \frac{i_0}{\frac{(\alpha+K)}{(\alpha-K)} - \exp(-2\alpha d) \frac{(\alpha-K)}{(\alpha+K)}}$$

$$C_1 = \frac{1 \cdot \exp(-2\alpha d)}{\frac{(\alpha+K) - \exp(-2\alpha d)(\alpha-K)}{(\alpha-K)} \frac{(\alpha-K)}{(\alpha+K)}}$$

The diffuse reflectance R of the sample is given by; $j(0)/i(0)$, hence,

$$R = \frac{S \cdot \sinh(\alpha d)}{(K+S) \sinh(\alpha d) + \alpha \cosh(\alpha d)} \quad \dots (2.3.5)$$

The diffuse reflectance R of the sample as a function of sample thickness is presented in fig (2.3.2) and fig (2.3.3).

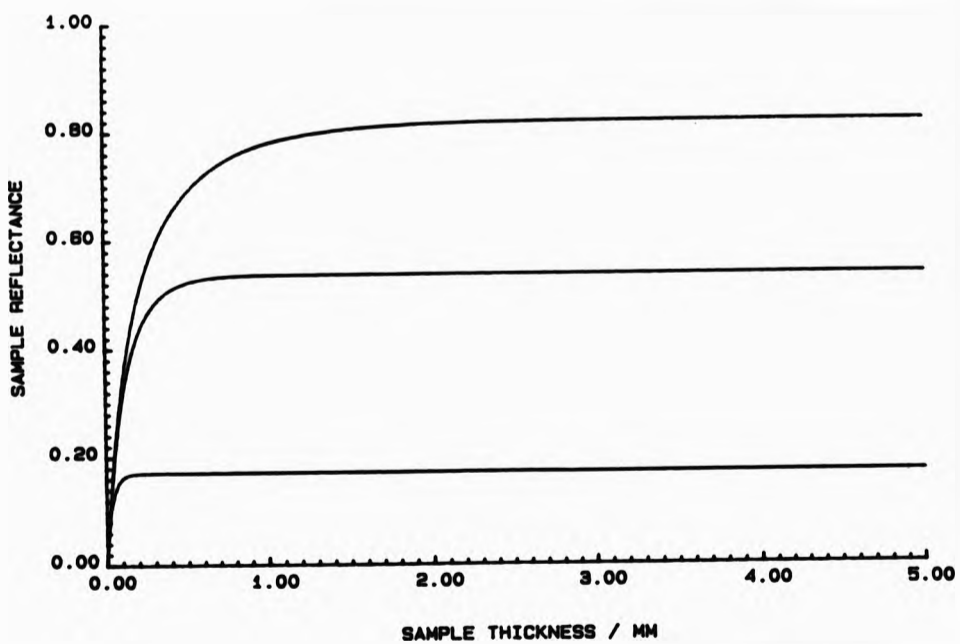


Fig (2.3.2)
The calculated diffuse reflectance of sample as a function of illuminated sample thickness. $S = 5 \text{ mm}^{-1}$ for all curves. Upper curve $K = 0.1 \text{ mm}^{-1}$, middle curve $K = 1 \text{ mm}^{-1}$, lower curve $K = 10 \text{ mm}^{-1}$.

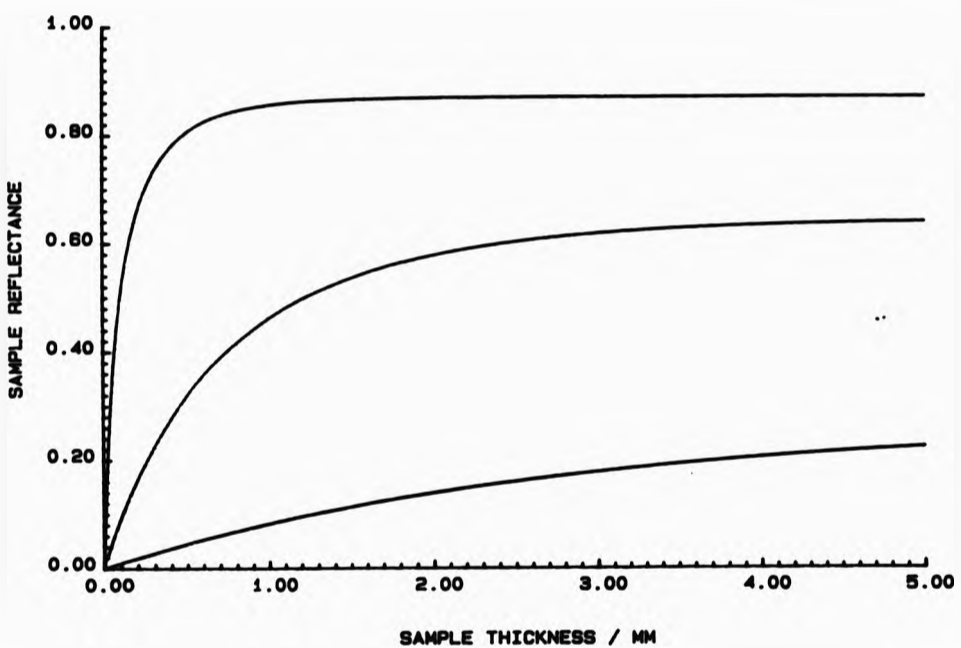


Fig (2.3.3)
 The calculated diffuse reflectance of sample as a function of illuminated sample thickness. $K = 0.1 \text{ mm}^{-1}$ for all curves. Upper curve $S = 10 \text{ mm}^{-1}$; middle curve $S = 1 \text{ mm}^{-1}$; lower curve $S = 0.1 \text{ mm}^{-1}$.

This expression may be greatly simplified if $K \ll S$, i.e. the absorption of the sample is negligible in comparison with the scattering. We cannot let K tend to zero directly in equation (2.3.5): if K tends to zero, α tends to zero and R tends to 1, i.e. R is independent of the sample thickness. However, by expanding the sinh and cosh terms in equation (2.3.5) and neglecting powers of K^2 and above we obtain,

$$R = \frac{Sd}{(K+S)d+3(1+KSd)/(3+KSd)} .$$

Letting K now tend to zero gives,

$$R = \frac{Sd}{(1+Sd)} \quad \dots(2.3.6)$$

The expression (2.3.6) may also be derived from equations (2.3.1) and (2.3.2) by putting $K=0$. Fig (2.3.6) illustrates equation (2.3.4) for various values of S.

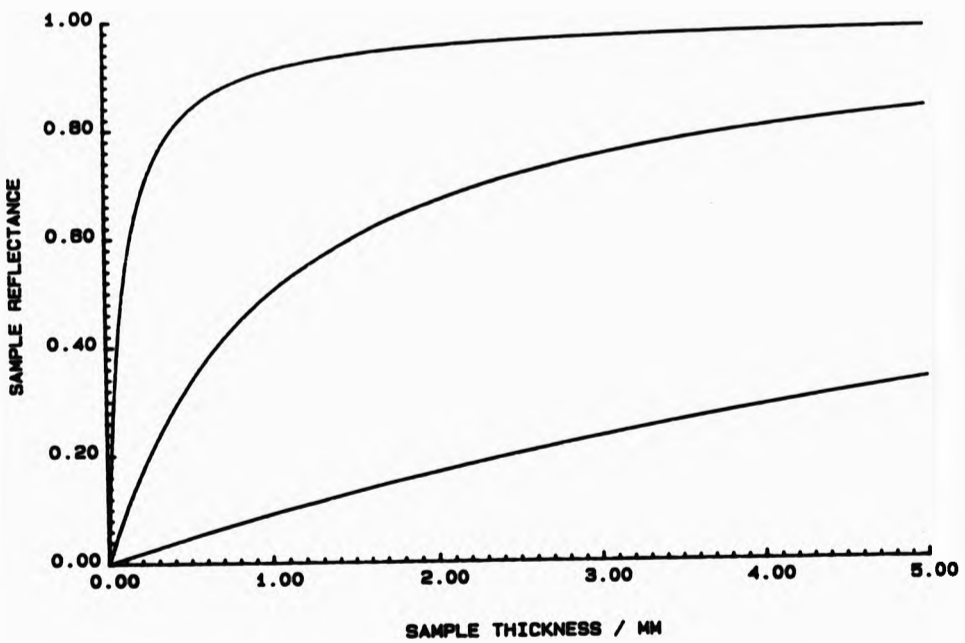



Fig (2.3.4)
 Calculated diffuse reflectance of sample as a function of illuminated sample thickness, (no absorption).
 Upper curve $S = 10 \text{ mm}^{-1}$, middle curve $S = 1 \text{ mm}^{-1}$, lower curve $S = 0.1 \text{ mm}^{-1}$.



Latimer and Noh [35] have shown that significant errors are present in Kubelka-Munk theory when applied to highly absorbing samples, (i.e. $K \approx S$). However, the application of the Kubelka-Munk theory is restricted in this investigation to cases of $S \gg K$, hence their observations are not pertinent to this work.

(2.3.3) Radiative transfer theory.

Radiative transfer theory [36,37] considers the transport of energy across a medium, (the carrier or matrix). However, the medium has embedded within it particles which may both scatter and absorb the incident radiation. The radiative transfer equation arises from the consideration of the energy interchanges between beams of energy traversing the scattering sample.

Consider a beam of energy, defined as travelling within the range of angles between $\theta+d\theta$ and $\theta-d\theta$, (where $d\theta$ is vanishingly small), of intensity $I(x,\theta)$, where x is the lateral penetration of the sample, (the sample is assumed to be plane parallel, infinite in lateral extent, and of thickness d). The intensity of the beam will be attenuated due to any absorption or scattering by the particles. This may be expressed by the equation;

$$dI(x,\theta) = -(K+S)I(x,\theta)dl, \quad \dots(2.3.7)$$

where $dI(x,\theta)$ is the loss in intensity due to scattering and absorption in traversing a path length dl within the sample. Equation (2.3.7) defines the scattering and absorption coefficients, S and K respectively. The beam under consideration will also gain by scattering from other beams traversing the sample. It is necessary here to introduce the phase function $P(\theta,\theta')$. This gives the intensity scattered from a beam $I(\theta')$ into the beam $I(\theta)$. $I(\theta')$ is defined analogously to $I(\theta)$. The phase function is normalized such that,

$$\frac{1}{4\pi} \int_{\omega'} P(\theta,\theta') d\omega' = \frac{1}{4\pi} \int_{\omega} P(\theta,\theta') d\omega = 1,$$

where dw is defined;

$$dw = \sin\theta d\theta d\phi = -\mu d\phi,$$

where ϕ is the azimuth angle around the axis, and $\mu = \cos\theta$.

The gain of $I(x, \theta)$ due to scattering from other beams is therefore,

$$dI(x, \theta) = S dl \int_{\omega'} P(\theta, \theta') I(x, \theta') d\omega' \quad \dots(2.3.8)$$

Adding equations (2.3.7) and (2.3.8) the total change in intensity of $I(x, \theta)$ in traversing a path length within the sample of dl is obtained, i.e.,

$$\frac{dI}{dl} = -(K+S)I(x, \theta) + \frac{S}{4\pi} \int_{\omega'} P(\theta, \theta') I(x, \theta') d\omega', \quad \dots(2.3.9)$$

or,

$$\mu \frac{dI}{dx} = -(K+S)I(x, \mu) + \frac{S}{2} \int_{-1}^1 P(\mu, \mu') I(x, \mu') d\mu'. \quad \dots(2.3.10)$$

The expression,

$$J(x, \mu) = \frac{1}{2} \int_{-1}^1 P(\mu, \mu') I(x, \mu') d\mu'$$

is termed the source function.

Equation (2.3.10) may be simplified by assuming isotropic scattering. If the scattering is isotropic then the phase function reduces to,

$$P(\mu, \mu') = 1.$$

Therefore the source function is

$$J(x, \mu) = \frac{1}{2} \int_{-1}^1 I(x, \mu') d\mu',$$

and hence the equation of radiative transfer becomes,

$$\mu \frac{dI}{dx} = -(K+S)I(x, \mu) + \frac{1}{2} \int_{-1}^1 I(x, \mu') d\mu'. \quad \dots(2.3.11)$$

The source function may be written,

$$J(x, \mu) = \frac{1}{2} \int_{-1}^1 I(x, \mu') d\mu' = \frac{1}{2} \int_0^1 I(x, \mu') d\mu' + \frac{1}{2} \int_{-1}^0 I(x, \mu') d\mu'.$$

Now the forward and backward diffuse fluxes are

$$I_+(x) = \int_0^1 I(x, \mu') d\mu' \quad \text{and} \quad I_-(x) = \int_{-1}^0 I(x, \mu') d\mu'. \quad \dots(2.3.12)$$

Hence the source function may be written

$$J(x) = \frac{1}{2} I_+(x) + \frac{1}{2} I_-(x)$$

Equation (2.3.11) then becomes,

$$\mu \frac{dI}{dx} = -(K+S)I(x, \mu) + \frac{S}{2} [I_+(x) + I_-(x)] \quad \dots(2.3.13)$$

Equation (2.3.13) may be integrated to obtain two dependent differential equations, in terms of the forward and backward diffuse fluxes,

$$\frac{d}{dx} \int_0^1 \mu I(x, \mu > 0) d\mu = -(K+S) \int_0^1 I(x, \mu > 0) d\mu + \frac{S}{2} [I_+(x) + I_-(x)] \quad \dots(2.3.14)$$

$$\frac{d}{dx} \int_{-1}^0 \mu I(x, \mu < 0) d\mu = -(K+S) \int_{-1}^0 I(x, \mu < 0) d\mu + \frac{S}{2} [I_+(x) + I_-(x)] \quad \dots(2.3.15)$$

The terms on the left hand side of equations (2.3.14) and (2.3.15) may be evaluated using the Schwarzschild approximation [37],

$$\int_0^1 \mu I(x, \mu) d\mu \approx \frac{1}{2} \int_0^1 I(x, \mu) d\mu = \frac{1}{2} I_+(x),$$

$$\int_{-1}^0 \mu I(x, \mu) d\mu \approx \frac{1}{2} \int_{-1}^0 I(x, \mu) d\mu = \frac{1}{2} I_-(x).$$

Hence, equations (2.3.14) and (2.3.15) become,

$$\frac{1}{2} \frac{dI_+}{dx} = -(2K+S)I_+ + SI_-, \quad \dots(2.3.16)$$

$$-\frac{1}{2} \frac{dI}{dx} = -(2K+S)I - SI_+ \quad \dots(2.3.17)$$

Equations (2.3.16) and (2.3.17) have the form of the expressions derived by Schuster [38] and Kubelka and Munk [30].

Equations (2.3.16) and (2.3.17) represent approximate solutions to the radiative transfer equation, equation (2.3.11). An exact solution to the radiative transfer equation may be obtained using the source function calculated from the approximate solution. Assuming zero absorption, (i.e. $K=0$),

$$\frac{1}{2} \frac{dI_+}{dx} = -S(I_+ - I_-),$$

$$\frac{1}{2} \frac{dI_-}{dx} = -S(I_+ - I_-).$$

The solution to these simultaneous differential equations are,

$$I_+ = \frac{I_0(1+S(d-x))}{1+Sd},$$

$$I_- = \frac{IS(d-x)}{1+Sd}.$$

From equation (2.3.12) we may obtain the source function,

$$J(x, \mu) = \frac{1}{2}(I_+ + I_-) = \frac{I_0(1/2 + S(d-x))}{1+Sd} \quad \dots(2.3.18)$$

Equation (2.3.10) may be integrated to obtain expressions for the forward ($\mu > 0$) and backward ($\mu < 0$) intensities [36],

$$I(x, \mu > 0) = I(0, \mu > 0) \exp(-(K+S)x/\mu) + \frac{S}{\mu} \int_0^x J(t, \mu) \exp(-(K+S)(x-t)/\mu) dt, \quad \dots(2.3.19)$$

$$I(x, \mu < 0) = I(d, \mu < 0) \exp(-(K+S)(d-x)/\mu) + \frac{S}{\mu} \int_x^d J(t, \mu) \exp(-(K+S)(t-x)/\mu) dt, \quad \dots(2.3.20)$$

where $I(0, \mu > 0)$ is the forward incident intensity at $x=0$, and $I(d, \mu < 0)$ is the backward intensity at $x=d$.

For the non-absorbing case, with no illumination at the distal boundary, (i.e. $K=0$, $I(d, \mu < 0)=0$),

$$I(0, \mu < 0) = \frac{S I_0}{\mu(1+Sd)} \int_0^d [(1/2+Sd)\exp(-St/\mu) - St\exp(-St/\mu)] dt. \dots(2.3.21)$$

Therefore,

$$I(0, \mu < 0) = \frac{I_0}{(1+Sd)} [(1/2-\mu)(1-\exp(-Sd/\mu)) + Sd]. \dots(2.3.22)$$

From equation (2.3.12) the backward flux, I_- is given by;

$$I_- = \int_{-1}^0 I(x, \mu < 0) d\mu.$$

Hence the backward flux at $x=0$ is,

$$I_- = \int_{-1}^0 I(0, \mu < 0) d\mu = \frac{I_0}{(1+Sd)} \int_{-1}^0 [(1/2-\mu)(1-\exp(-Sd/\mu)) + Sd] d\mu. \dots(2.3.23)$$

Hence,

$$I_- = \frac{I_0}{(1+Sd)} [E_1(Sd) \frac{(Sd+(Sd))}{2} + (Sd - \frac{Sd \exp(-Sd)}{2})]. \dots(2.3.24)$$

where the function $E_n(a)$ is defined thus [39];

$$E_n(a) = \int_1^{\infty} \frac{\exp(-ax) dx}{x^n}.$$

Abramowitz and Stegun [39] provide useful approximations for calculating $E_n(a)$.

(2.3.4) Comparison of radiative transfer theory with Kubelka-Munk theory.

The purpose of this section is to examine the limits over

which the Kubelka-Munk equations may be meaningfully applied. The second approximation solution to the equation of radiative transfer is not an exact solution in that it uses an approximate source function. However, Kottler [38] has shown, by comparison of the second approximation with an exact solution, that the second approximation is a good approximation to the exact solution for the non-absorbing isotropically scattering case. Hence a comparison of the second approximation with the Kubelka-Munk theory will be instructive.

Table (2.3.1) compares the diffuse reflectance of a non-absorbing isotropically scattering sample as calculated using equation (2.3.24) and the Kubelka-Munk equation,

$$R = \frac{Sd}{(1+Sd)}$$

It can be seen from table (2.3.1) that for low values of Sd , (i.e. $Sd < 0.1$), there is very poor agreement between the two expressions. However, as Sd is increased the difference between the expressions is rapidly reduced, i.e. when $Sd = 0.50$ the difference between the expressions is 10 %, when Sd is increased to 1.0 the difference is reduced to 3.5 %. It can hence be concluded that the application of Kubelka-Munk theory to samples where $Sd < 1$ will lead to large errors. To evaluate the effects of fitting experimental results obtained over a range of Sd values to the Kubelka-Munk theory, data was generated using equation (2.3.24), (with $S=1 \text{ mm}^{-1}$), and fitted to the Kubelka-Munk equation using a least squares fitting routine. The diffuse reflectance was calculated for path lengths between 0 and $Sd(\text{max})$, in equal steps

of 0.01. Table (2.3.2) illustrates the fitted Kubelka-Munk value of S as a function of Sd(max).

Sd	R(R-T)	R(K-M)	% difference
0.01	0.0252	0.0099	154
0.02	0.0435	0.0196	122
0.03	0.0594	0.0291	104
0.04	0.0736	0.0385	91.4
0.05	0.0867	0.0476	82.0
0.06	0.0988	0.0566	74.6
0.07	0.110	0.0654	68.5
0.08	0.121	0.0741	63.3
0.09	0.131	0.0826	58.9
0.10	0.141	0.0909	55
0.12	0.159	0.107	48.6
0.14	0.176	0.123	43.4
0.16	0.192	0.138	39.1
0.18	0.207	0.153	35.5
0.20	0.221	0.167	32.4
0.25	0.247	0.200	26.3
0.30	0.281	0.231	21.8
0.35	0.307	0.259	18.4
0.40	0.330	0.286	15.7
0.45	0.352	0.310	13.5
0.50	0.372	0.333	11.7
0.60	0.408	0.375	8.91
0.70	0.440	0.412	6.94
0.80	0.469	0.444	5.49
0.90	0.494	0.474	4.39
1.00	0.518	0.500	3.54
1.20	0.558	0.545	2.36
1.40	0.593	0.583	1.62
1.60	0.622	0.615	1.13
1.80	0.648	0.643	0.795
2.00	0.670	0.667	0.569
2.50	0.716	0.714	0.256
3.00	0.751	0.750	0.120
3.50	0.778	0.778	0.058
4.00	0.800	0.800	0.029

Table (2.3.1).

Sd(max)	Fitted value of S/ mm ⁻¹
20	1.028
10	1.032
5	1.048
4	1.050
3	1.062
2	1.075
1.5	1.132
1.0	1.184
0.9	1.193
0.8	1.209
0.7	1.221
0.6	1.240
0.5	1.291
0.4	1.346
0.3	1.434
0.2	1.540
0.1	1.735

Table (2.3.2)

It can be seen from table (2.3.2) that as long as the maximum value of Sd exceeds 4 the fitted value of S should be within 5 % of the actual value. Hence the Kubelka-Munk expression would appear to be a reasonable approximation provided that the values of Sd over which it is applied are large, (i.e. Sd(max) > 4).

(2.3.5) Four-flux theory.

Four-flux theory [40] is similar in its approach to the two flux theory of Kubelka and Munk. The main differences between the two theories arise from the fact that four flux theory considers collimated as well as diffuse fluxes within the sample. The assumptions of four flux theory are essentially the same as those for Kubelka-Munk theory, i.e. the sample is infinite in lateral extent, scatters light isotropically and is homogeneous. However the consideration of collimated flux, as well as diffuse flux, introduces further scattering parameters to account for scattering from the collimated flux to the forward and backward diffuse fluxes. For the purpose of this analysis it is assumed that the sample is negligibly absorbing. As in the Kubelka-Munk theory the interchange between the fluxes is governed by the various scattering parameters. A single scattering parameter S determines the interchange between the forward and backward diffuse fluxes. The scattering parameter S_1 determines the scattering from the forward collimated to forward diffuse flux, and a third scattering parameter S_2 describes the scattering from forward collimated to backward diffuse flux. It is assumed that all the light scattered becomes diffuse, i.e. no light is scattered from the forward or backward diffuse flux into the collimated flux. It is assumed in the following derivation that the backward collimated flux is zero. The forward and backward diffuse fluxes are denoted by i and j respectively, the forward collimated flux is denoted by I . Considering the change in the fluxes in traversing a thickness dz of sample the following equations are obtained,

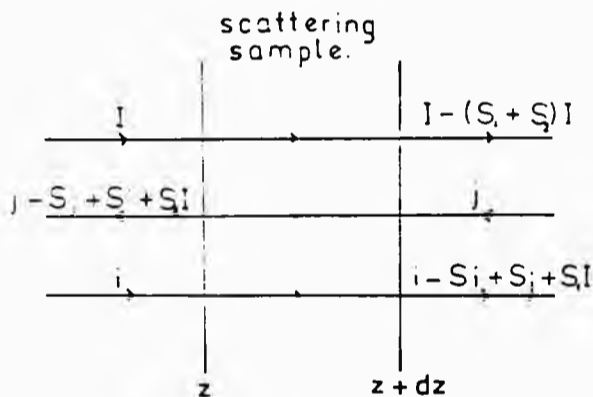
$$dI = -(S_1 + S_2)I dz, \quad \dots(2.3.25)$$

$$dI = (j-1)S dz + S_1 I dz, \quad \dots(2.3.26)$$

and $dj = (j-1)S dz - S_2 I dz. \quad \dots(2.3.27)$

Solving equation (2.3.23) gives,

$$I = C, \exp(-(S_1 + S_2)z).$$



Fig(2.3.5)
Diffuse and collimated fluxes
traversing a sample thickness dz.

Solving equations (2.3.26) and (2.3.27) simultaneously, and applying the boundary conditions that;

- (a) The incident collimated intensity at $z=0$ is I_0 .
- (b) The incident diffuse intensity at $z=0$ is zero.
- (c) The sample is backed by an absorbing surface at $z=d$, gives the expression for the diffuse reflectance R ,

$$R = \frac{(S_2 - S_1)(1 - \exp(-S_2 d)) + (S_1 + S_2)S d}{(1 + S d)(S_1 + S_2)} \quad \dots(2.3.28)$$

where $S_2 = S_1 + S_3$.

(2.3.6) Photon diffusion theory.

The photon diffusion theory [41,42] differs from the two previous theories greatly in its approach to the multiple scattering problem. The theory treats photons in a diffuse flux as if they were molecules of a dilute gas. It is assumed that the photons will diffuse through the scattering medium, under steady state conditions with a time invariant light source, in a manner obeying Fick's law. Standard results for gases give the (analogous) photon flux over a plane to be $nc/4$, (where n is the number of photons per unit volume), and a diffusion coefficient D of $c\Lambda/3$, where Λ is the mean free path length of a photon within the scattering medium. These results have been reached for gases that have only small deviations from isotropy, hence these results can only strictly be applied to photons of an isotropic flux.

The forward and backward diffuse fluxes will be denoted by i and j respectively. Considering the flux across an elemental thickness of sample dz , the total flux density leaving the sample is,

$$i + j + \left(\frac{\partial j}{\partial z}\right) \cdot dz. \quad \dots(2.3.29)$$

and the total flux density entering the sample is,

$$i + j + \left(\frac{\partial i}{\partial z}\right) \cdot dz. \quad \dots(2.3.30)$$

d Where $c = \text{vel. of light}$

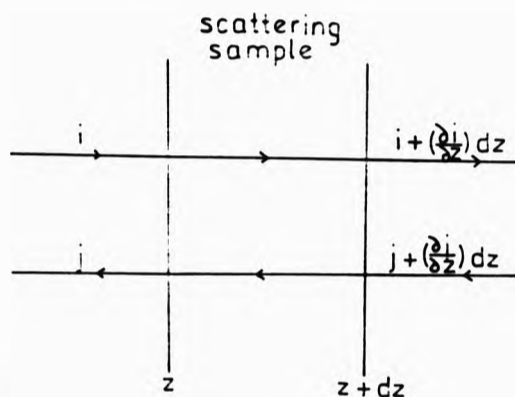


Fig (2.3.6)
Photon flux densities entering and exiting an elemental thickness of sample.

When the sample is in equilibrium the net photon flux into the sample must equal the net photons absorbed by the sample. Denoting the absorption coefficient of the sample as Σ_a then the rate at which photons are absorbed over a unit area of sample is,

$$(i+j)\Sigma_a dz.$$

The factor $2dz$ arises from considering the mean distance travelled by a photon in an isotropic flux in traversing a thickness dz of sample. Hence when the system is in equilibrium,

$$\frac{d}{dz}(i-j) + (i+j)2\Sigma_a = 0. \quad \dots(2.3.31)$$

The photon density along the z -axis may be obtained from Fick's law which states that the photon flux density along any coordinate u is,

$$-D\left(\frac{\partial n}{\partial u}\right)$$

For an isotropic flux u will point in all directions, it can be shown that the flux along the z -axis will then be,

$$-\frac{D}{2} \left(\frac{\partial n}{\partial z} \right)$$

Hence the photon flux densities in the forward and backward directions, (i and j respectively), are;

$$i = \frac{nc}{4} - \frac{D}{2} \left(\frac{\partial n}{\partial z} \right), \quad \dots(2.3.32)$$

$$j = \frac{nc}{4} + \frac{D}{2} \left(\frac{\partial n}{\partial z} \right). \quad \dots(2.3.33)$$

Substituting equations (2.3.32) and (2.3.33) into (2.3.31) gives,

$$\frac{\partial n}{\partial z} = \frac{nc}{D} \sum_s$$

or

$$\frac{\partial n}{\partial z} = \frac{3n}{\Lambda} \sum_s \quad \dots(2.3.34)$$

From neutron diffusion theory Gate [42] obtained,

$$\frac{\partial n}{\partial z} = 3n \sum_s \sum_{s_1} \quad \dots(2.3.35)$$

where \sum_s is the inverse scattering length. Expressions (2.3.16) and (2.3.17) are identical if,

$$\sum_s = 1/\Lambda$$

For isotropic scattering it can be shown that $\sum_s = 1/\Lambda = NC_{sc}$. Gate [41] has solved equation (2.3.34) for a sample infinite in lateral extent and of finite thickness d, backed by an absorbing boundary, to obtain an expression for the diffuse reflectance R, of the sample,

$$R = \frac{1 - \sqrt{\sum_s D} \coth(\sqrt{\sum_s D} d)}{1 + \sqrt{\sum_s D} \coth(\sqrt{\sum_s D} d)} \quad \dots(2.3.36)$$

(2.3.7) Comparison of multiple scattering theories.

Ishimaru [43] has solved the radiative transfer equation, applied to a plane parallel slice of non-absorbing sample, illuminated by collimated flux to obtain the expression,

$$R = \frac{3/4NC_{\text{sc}}(1-\overline{\cos\theta}) \cdot d - 1/4(1-\exp(-NC_{\text{sc}} \cdot d))}{(1 + 3/4NC_{\text{sc}}(1-\overline{\cos\theta}) \cdot d)} \dots(2.3.37)$$

Meeten [40] has shown that this is identical to the four-flux equation,

$$R = \frac{(S_0 - S)(1-\exp(-S_1 d)) + (S_1 + S_2)S \cdot d}{(1+Sd)(S_1 + S_2)} \dots(2.3.38)$$

so long as,

$$S = 3/4NC_{\text{sc}}(1-\overline{\cos\theta}), \dots(2.3.39)$$

$$S_1 = NC_{\text{sc}}(1/2+3/4\overline{\cos\theta}), \dots(2.3.40)$$

$$S_2 = NC_{\text{sc}}(1/2-3/4\overline{\cos\theta}). \dots(2.3.41)$$

The quantities S , S_1 and S_2 may therefore be calculated using Mie theory.

Brinkworth [44], has compared the photon diffusion theory of Gate [42], with the Kubelka-Munk theory, to provide a useful interpretation of the Kubelka-Munk coefficients K and S .

From the photon diffusion theory the forward and backward photon flux densities are,

$$i = \frac{nc}{4} - \frac{D(\partial n)}{2(\partial z)}, \dots(2.3.42)$$

$$j = \frac{nc}{4} + \frac{D(\partial n)}{2(\partial z)}. \dots(2.3.43)$$

Also,

$$\frac{\partial n}{\partial z} = 3n \sum_n \sum_s. \dots(2.3.44)$$

The Kubelka-Munk theory gives forward and backward flux densities of,

$$\frac{di}{dz} = (S+K)i - Sj \dots(2.3.45)$$

and

$$\frac{dj}{dz} = -(S+K)j + Si \dots(2.3.46)$$

It follows that [44],

$$K = \frac{di/dz - dj/dz}{1+j} \quad \dots(2.3.47)$$

$$S = 1/2 \left(\frac{di/dz + dj/dz}{1-j} - \frac{di/dz - dj/dz}{1+j} \right) \quad \dots(2.3.48)$$

Equations (2.3.43), (2.3.44) and (2.3.45) give,

$$1+j = \frac{nc}{2}, \quad 1-j = D \left(\frac{dn}{dz} \right),$$

$$\frac{di}{dz} + \frac{dj}{dz} = \frac{c}{2} \left(\frac{dn}{dz} \right),$$

and

$$\frac{di}{dz} - \frac{dj}{dz} = nc \sum_{s_1}$$

Substituting these values into (2.3.47) and (2.3.48) gives,

$$K = 2 \sum_{s_1} \quad \text{and} \quad S = 3/4 \sum_{s_1} - \sum_{s_1} / \sum_{s_1}$$

It is however an assumption of equation (2.3.44) that $\sum_{s_1} \ll \sum_{s_2}$, hence to a good approximation,

$$S = 3/4 \sum_{s_1}$$

(Note, $\sum_{s_1} = NC_{s_1}$, and $\sum_{s_2} = NC_{s_2}$).

Brinkworth [20] later modified this result to allow for anisotropic scattering to give,

$$S = 3/4 NC_{s_1} (1 - \overline{\cos \theta}).$$

An identical result to that obtained by the comparison of four-flux theory with the radiative transfer theory of Ishimaru.

Mudgett and Richards [22] compared Kubelka-Munk theory with a numerical radiative transfer theory calculation involving 22 fluxes. They obtained the result that,

$$K = 2 \sum_{s_1} \quad \text{and} \quad S = \sum_{s_1} \frac{(3a_{s_1} - a_{s_1})}{4}$$

Where a_{s_1} and a_{s_2} are the first two coefficients of the expression,

$$p(\cos \theta) = \sum_n a_n P_n(\cos \theta),$$

where $P_n(\cos\theta)$ is the Legendre polynomial of order n and degree zero. The function is normalized such that,

$$\frac{1}{2} \int_{-1}^1 p(\cos\theta) d(\cos\theta) = 1$$

giving $a_0 = 1$. Hence,

$$S = 3/4NC_{sa} (1-a_0/3).$$

It is possible to show that [44], $\overline{\cos\theta} = a_0/3$, hence,

$$S = 3/4NC_{sa} (1-\overline{\cos\theta}),$$

an identical result to that obtained above from comparisons of four flux theory with radiative transfer theory, and Kubelka-Munk theory with photon diffusion theory. It is therefore reasonable to conclude that, to a good approximation, (so long as the absorption of the sample is small),

$$S = 3/4NC_{sa} (1-\overline{\cos\theta}), \quad \dots(2.3.49)$$

and

$$K = 2NC_{ab}, \quad \dots(2.3.50)$$

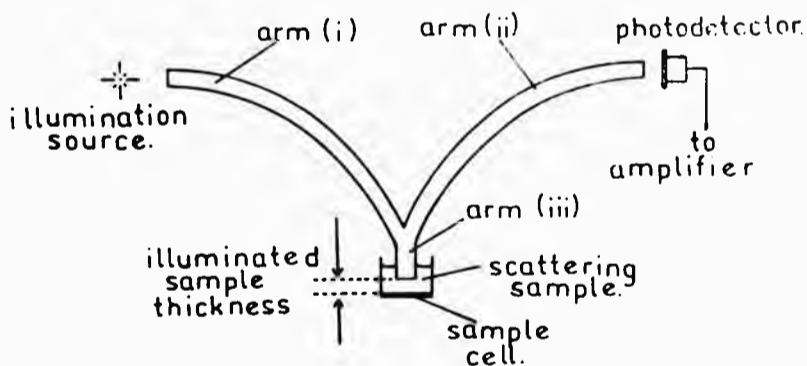
The quantities C_{sa} , $\overline{\cos\theta}$ and C_{ab} may be calculated from single scattering (Mie) theory. It is therefore possible to relate the multiple scattering parameters S and K to calculable single scattering parameters.

It must be noted that equation (2.3.49) is derived assuming that $\sum_1 \ll \sum_2$. This is true for all the samples to which equation (2.3.49) is applied in this investigation. Graaf et al. [23] report more complex expressions for S applicable to more highly absorbing samples.

CHAPTER 3: BIFURCATED OPTICAL FIBRE MEASUREMENTS OF S.

(3.1) Experimental system.

A bifurcated optical fibre bundle was used to both illuminate a scattering sample and to detect flux reflected from it. Arm (i) of the fibre conducted light into the sample. Arm (ii) conducted reflected flux out of the sample to the photodetector. See fig (3.1.1).



Fig(3.1.1)
Bifurcated optical fibre bundle system.

The common arm of the fibre, arm (iii), was centrally placed within the cylindrical glass sample cell, above (and with its face parallel to) the matt black cell base. The parallel slice of sample between the face of the common arm and the cell base was therefore illuminated by the fibre bundle, the thickness of the illuminated slice of sample being controlled by the height of the




common arm above the cell base.

The bifurcated optical fibre bundle was made up from many multi-mode silica fibres with numerical apertures of 0.50, (manufacturer's data, at 589 nm). The diameter of the common end of the fibre bundle was $(6.89 \pm .07)$ mm. The common arm of the fibre, arm (iii), contained a 50-50 split of fibres from arm (i) and arm (ii). They were approximately arranged as two semicircles of equal radii.

The light source consisted of a 100 Watt quartz halogen lamp, driven by a stabilised power supply. The detection system consisted of a silicon photodiode, of active area 100 mm^2 , and wavelength range 350 to 1100 nm. The photodiode was operated in the linear response photoelectric mode, the output was fed to a low input impedance amplifier, giving a four figure readout of received intensity over a six decade range. The sample cell consisted of a glass cylinder of diameter 28 mm, height 25 mm, glued to a flat, matt black, plastic base. Interference filters, (of approximate bandwidth 16 nm), were placed between arm (ii) and the photodetector to filter the detected flux to the required wavelength.

The linearity of response of the detection system was checked by illuminating the photodetector through crossed polarisers. Rotation of the polarisers, (with respect to each other), gave variations in intensity in excellent agreement with Malus' law [4], over all six decade ranges.



The output stability of the illumination system was checked by monitoring the output intensity using the above detection system. Variations of intensity with time of less than 2 % per hour were noted once the lamp had been allowed to warm up for 1/2 hour.

Initial experiments showed that it was important that care was taken to ensure that;

- (a) the face of the common arm of the probe was parallel with the cell base, and
- (b) the point at which the common arm of the optical fibre bundle made contact with the cell base could be accurately determined.

A cell mounting system was designed that allowed the cell base to be aligned parallel with the probe face to within 0.2 degrees.

A movement system was designed utilizing a 1.8 degree per step motor, driving a screw thread of 10 turns per cm. The probe was mounted on a carriage driven by the screw thread. The probe height could thus be altered in 5 micron steps. The stepper motor movement was governed using software controlled output from the microcomputer, via an interface circuit. The microcomputer was also used to collect the intensity data. An analogue output from the photodiode amplifier was fed directly to an analogue input on the microcomputer.

The output from the amplifier was updated every 0.04 seconds,

the software used to collect the data was therefore written with an in-built sampling time of greater than 0.04 seconds. The use of the microcomputer to monitor the received intensity allowed many intensity readings to be averaged for each sample thickness. Thirty intensity readings were averaged for each sample thickness, reducing the r.m.s. noise by a factor of approximately 5.

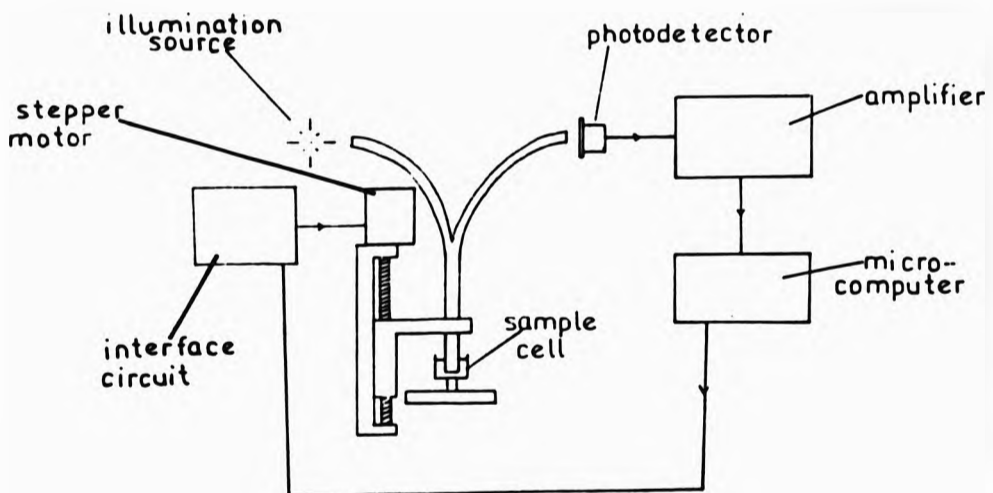


Fig (3.1.2)
Automated experimental system.

Monodisperse spherical latex particles suspended in de-ionized water were used to provide well characterized scattering samples. For particle diameters less than 1.5 microns, no settling could be detected during an experiment.

The experimental procedure was as follows:

- (1) The sample cell was filled with the scattering sample.

- (2) The common arm of the optical fibre bundle was placed within the sample and moved downwards until it was in contact with the base of the cell.
- (3) The common arm was then moved upwards through the sample, and the reflected intensity measured as a function of illuminated sample thickness.

(3.2) Initial experiments.

The data obtained was initially analysed by fitting to the Kubelka-Munk equation for a scattering and absorbing sample [40],

$$I = \frac{A.S.\sinh(\alpha d)}{(K+S)\sinh(\alpha d) + \alpha \cosh(\alpha d)}, \quad \dots(3.2.1)$$

where I is the detected intensity, and A is a constant relating the detected intensity to the reflectance R of the sample.

It was found that the values of K returned by such fits were very small, at least 1000 times smaller than the fitted value of S. It was therefore decided that the non-absorbing expression for the diffuse reflectance R, could safely be used with little loss in accuracy. The data was fitted to the non-absorbing Kubelka-Munk expression,

$$I = \frac{A.Sd}{(1+Sd)}. \quad \dots(3.2.2)$$

The fits themselves were carried out using a least squares fitting programme. Figures (3.2.1) and (3.2.2) illustrate examples of fits to both the absorbing and non-absorbing Kubelka-Munk expressions.

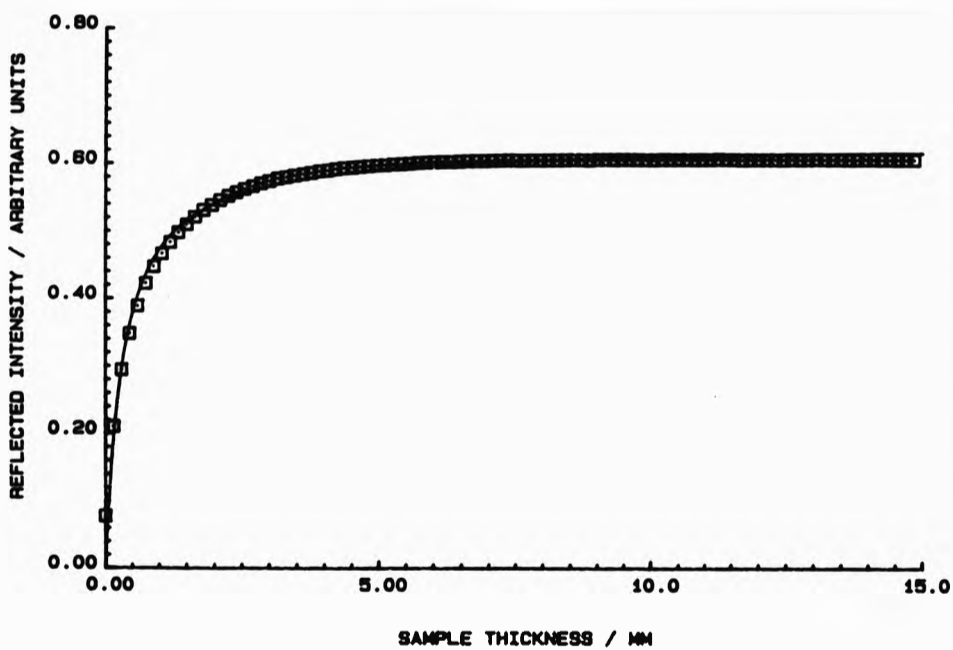


Fig (3.2.1)
 Reflected intensity as a function of probe height. Latex spheres suspended in water. Mean diameter 0.73 μm , volume fraction 0.0238. Wavelength = 589 nm. Solid line shows fitted curve, equation (3.2.1). Fitting results; $S = 2.95 \text{ mm}^{-1}$, $A = 0.63$ (arbitrary units) and $K = 0.0007 \text{ mm}^{-1}$.

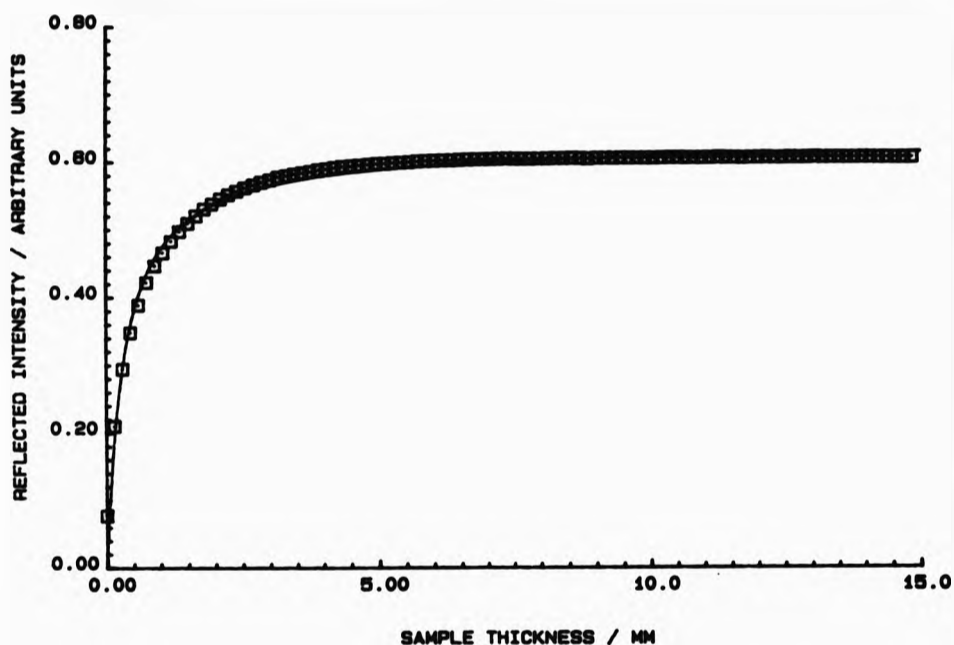


Fig (3.2.2)
 Reflected intensity as a function of probe height. Latex spheres suspended in water. Mean diameter $0.73 \mu\text{m}$, volume fraction 0.0238. Wavelength = 589 nm. Solid line shows fitted curve, equation (3.3.2). Fitting results; $S = 2.85 \text{ mm}$, $A = 0.62$ (arbitrary units).

It can be seen from fig (3.2.2) that a fairly good agreement between the experimental data and the non-absorbing Kubelka-Munk expression is obtained.

It was found that the fitted value of S could be made to vary by up to 30 %, by simply rotating the input arm in the focussed beam from the quartz halogen lamp. This effect was thought to be due to the finite separation between the input and output routes of

the optical flux into and out of the sample. By focussing the lamp on different parts of the input arm, (as is effected by rotating the fibre in the beam of light), the effective separation of the influx and efflux routes is varied. This implies that;

(i) the measured value of S is highly dependent upon the fibre separation, and

(ii) if a perfectly diffuse flux is incident upon the input arm, rotating the fibre in the beam will have no effect on the measured value of S .

A diffuser was fitted over the input arm of the optical fibre. The diffuser was manufactured out of a solid block of PTFE, a highly scattering non-absorbing material [45]. The diffuser was approximately 5 mm thick and of diameter 20 mm. It was made to fit tightly across the input arm of the bifurcated fibres. With the diffuser fitted it was found that repeatable results could be obtained, (no matter how the input arm was rotated in the illuminating beam), if the diffuser was evenly illuminated. The diffuser did however reduce the intensity input to the sample. To counter this a more powerful lamp was employed, a 250 W quartz halogen lamp. The quality of fit appeared to be unaltered by the use of the diffuser.

(3.3) S as a function of particle size.

Intensity readings for sample thicknesses between 0.00 and 14.85 mm were recorded (in equal steps of 0.15 mm), and fitted to equation (3.2.2) for the monodisperse latex samples, (at a volume fraction of 0.0238), for two wavelengths, 589 nm and 546 nm. The

fitting results are given in tables (3.3.1) and (3.3.2). The results are compared with the theoretical values as computed from Mie theory and equation (2.3.49). The experimental value of S quoted in the tables is the mean result from four separate experiments on each sample. The quoted error is the standard error of the four results.

Particle diameter / microns	$S(\text{Mie})/\text{mm}^{-1}$	$S(\text{Exp})/\text{mm}^{-1}$	$S(\text{exp})/S(\text{Mie})$
0.11	2.87	0.56 +/- .02	0.200 +/- .001
0.25	8.19	2.70 +/- .07	0.33 +/- .01
0.37	9.01	3.5 +/- .1	0.39 +/- .01
0.48	8.84	3.1 +/- .1	0.39 +/- .01
0.73	7.03	3.0 +/- .1	0.42 +/- .01
1.05	5.95	2.4 +/- .1	0.41 +/- .01
1.43	5.02	2.25 +/- .05	0.45 +/- .01

Table (3.3.1): Wavelength = 589 nm.

Particle diameter / microns	$S(\text{Mie})/\text{mm}^{-1}$	$S(\text{Exp})/\text{mm}^{-1}$	$S(\text{Exp})/S(\text{Mie})$
0.11	3.94	0.75 +/- .01	0.190 +/- .001
0.25	8.33	3.0 +/- .1	0.36 +/- .01
0.37	10.00	3.5 +/- .1	0.35 +/- .01
0.54	8.57	3.00 +/- .05	0.35 +/- .01
0.77	7.30	3.00 +/- .01	0.411 +/- .001
0.95	6.46	2.65 +/- .05	0.41 +/- .01
1.43	5.12	2.1 +/- .1	0.41 +/- .02

Table (3.3.2): Wavelength = 546 nm.

It can be seen from the above tables that agreement between the experimental and theoretical absolute values of S is very poor. However, the ratio of the experimental to theoretical values remains approximately constant over the whole particle size range, for both wavelengths, at 0.40 +/- .04. The exception to this is the 0.11 micron sample. This might be explained if the size of the

0.11 micron sample has been slightly over-estimated by the manufacturers. This is illustrated in figures (3.3.1) and (3.3.2) which give both the experimental and the theoretical values of S as a function of particle size. Note that the experimental values of S have been multiplied by a common factor of $1/0.40$ to reduce the discrepancy between the absolute experimental and theoretical values of S .

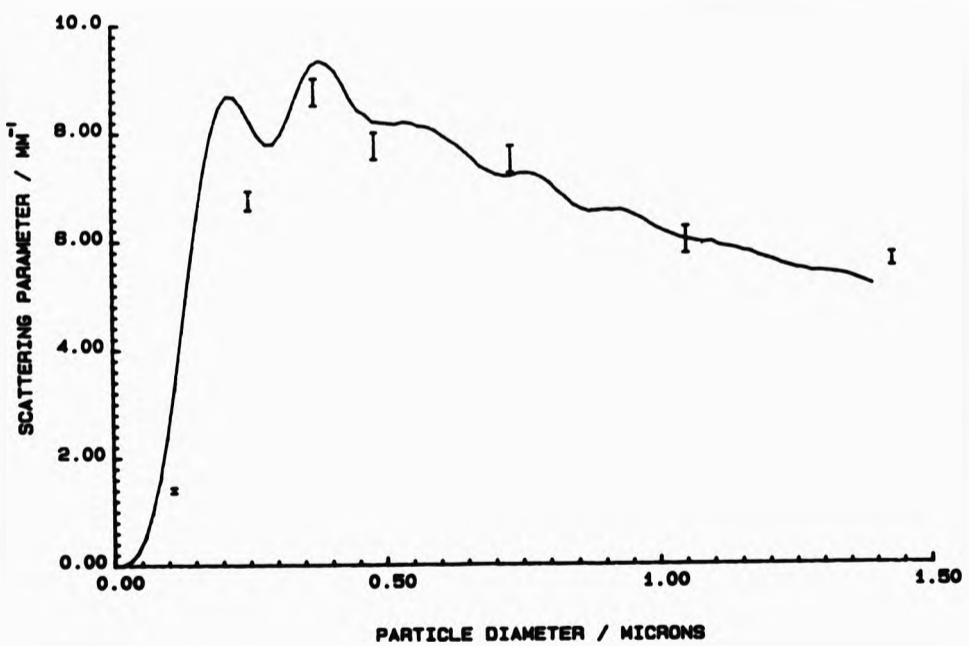
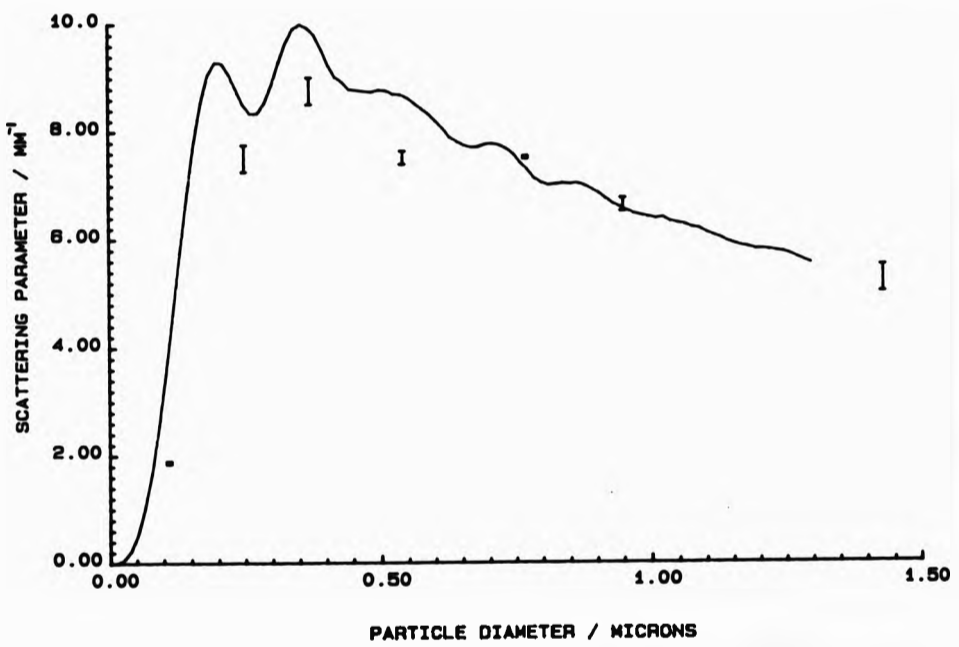


Fig (3.3.1)
 Scattering parameter as a function of mean particle size. Solid line represents theoretical results generated for a constant volume fraction of 0.0238. The experimental values have been multiplied by a factor of 2.5. Wavelength = 589 nm.



Fig(3.3.2)
 Scattering parameter as a function of mean particle size. Solid line represents theoretical results generated for a constant volume fraction of 0.0238. The experimental values have been multiplied by a factor of 2.5. Wavelength = 546 nm.

(3.4) S as a function of sample concentration.

The scattering parameter S of two monodisperse latex samples, (0.54 and 0.73 micron mean diameters), were measured as a function of decreasing sample concentration. The samples were diluted with de-ionized water to decrease their concentrations. The concentration of the samples was measured by drying and weighing.

The experiments were carried out at a wavelength of 589 nm. The illuminated sample thickness was varied between 0.00 and 4.95 mm, for all the samples. The intensity readings being recorded for steps of 0.05 mm in sample thickness. The results were analysed by fitting to equation (3.3.2) The fitting results are given in tables (3.4.1) and (3.4.2), and illustrated in figures (3.4.1) and (3.4.2). The quoted value of S is the mean of the fitting results to four separate experiments on each sample. The quoted error in S is the standard error of the four values of S so obtained.

Volume Fraction ($\pm 3\%$)	S/mm^{-1}
0.0238	2.94 \pm .04
0.0227	2.81 \pm .03
0.0216	2.69 \pm .04
0.0206	2.63 \pm .03
0.0184	2.41 \pm .06
0.0129	1.80 \pm .02
0.0104	1.55 \pm .01
0.0079	1.26 \pm .02
0.0058	1.00 \pm .02
0.0037	0.77 \pm .02

Table (3.4.1)
0.54 micron sample.

Volume Fraction (+/- 3%)	S/mm ⁻¹
0.0238	2.98 +/- .05
0.0214	2.67 +/- .09
0.0185	2.28 +/- .02
0.0162	2.04 +/- .03
0.0135	1.73 +/- .02
0.0124	1.48 +/- .02
0.0090	1.28 +/- .01
0.0074	1.10 +/- .02
0.0044	0.76 +/- .03

Table (3.4.2)
0.73 micron sample.

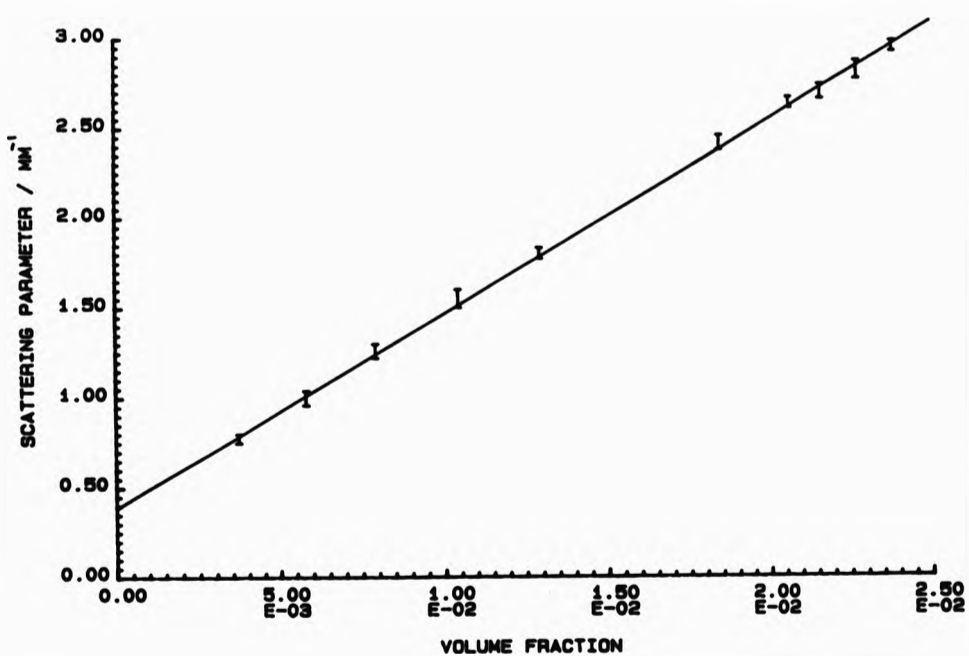


Fig (3.4.1)
Scattering parameter S as a function of volume fraction of sample. Mean particle size = 0.54 microns. Illuminating wavelength = 589 nm.

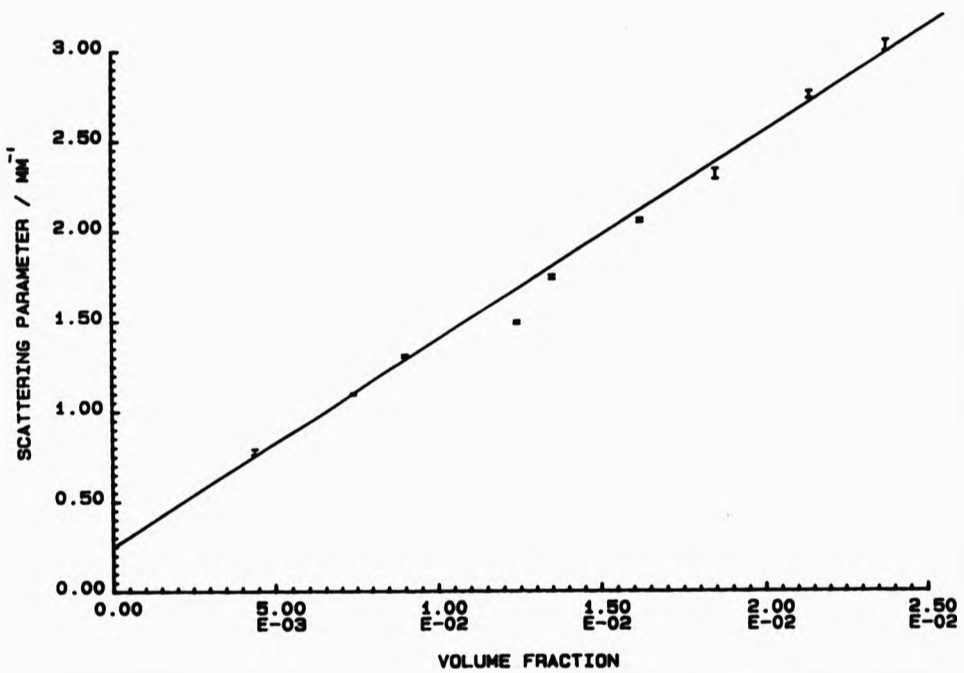


Fig (3.4.2)
 Scattering parameter S as a function of volume fraction
 of sample. Mean particle size = 0.73 microns. Illuminating
 wavelength = 589 nm.

It can be seen from fig (3.4.1) and fig (3.4.2) that to a good approximation, the results lie on a straight line. If the equation $S = \frac{3}{4}NC_{pm} (1 - \overline{\cos\theta})$ is correct then we would expect a linear relationship between S and the volume fraction of the sample, but with the intercept at the origin. Thus the finite intercepts illustrated in fig (3.4.1) and fig (3.4.2) suggests that there is a

flaw in the bifurcated experimental system. The nature of the problem is unclear. However, it was noted earlier that focussing the illumination on different parts of the input arm gave differing values of S . Moving the position of the focal point on the input arm had the effect of varying the separation between the influx and efflux routes within the sample. This implies that the measured value of S is dependent upon the separation between the influx and efflux routes. This effect may be connected with the fact that a non-zero intercept is obtained.

(3.5) Experiments with fibres of different numerical apertures.

Further experiments were carried out using two new bifurcated optical fibre bundles, types K2 and A2, of numerical apertures 0.21 and 0.66 respectively, (manufacturers data, quoted at 589 nm). Both bundles were made up from silica multi-mode step indexed fibres, and were supplied by Schott UK. The diameters of the common end of the bifurcated bundles were $(3.02 \pm .04)$ mm for bundle K2, and $(3.01 \pm .04)$ mm for bundle A2. The mixture of the input and output fibres, at the common end of the bifurcated probe, could be (very) roughly approximated to by two semi-circles of equal radii.

The experiments were carried out at a wavelength of 589 nm. The illuminated sample thickness was varied between 0.00 and 4.95 mm, in 0.05mm steps, for all the samples. The results were analysed by fitting to equation (3.2.2). An example of the fit

obtained for fibres A2 and K2 are illustrated in figures (3.5.1) and (3.5.2). The fitting results are given in table (3.5.1). Table (3.5.2) compares the experimental values of S with the theoretical values. The quoted values of S in the tables is the mean value from four experiments on the same sample. The quoted error is the standard error of the four results.

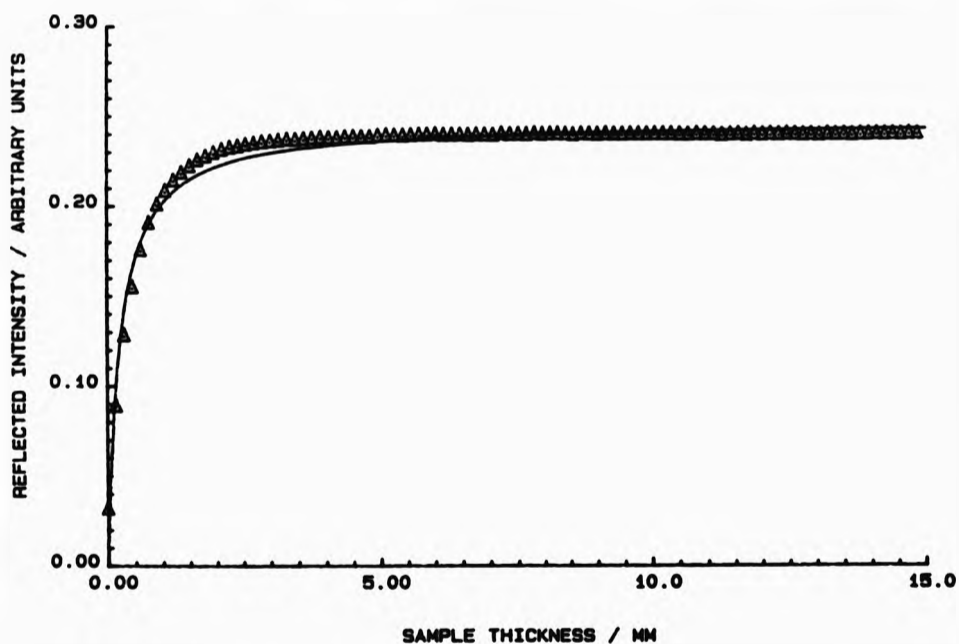


Fig (3.5.1)
 Reflected intensity as a function of illuminated sample thickness. Mean diameter = 0.73 microns. Wavelength = 589 nm. Fibre type K2, (NA=0.66). Solid line illustrates fitted curve, equation (3.3.1) with $A = 0.24$ (arbitrary units) and $S = 4.6 \text{ mm}^{-1}$.

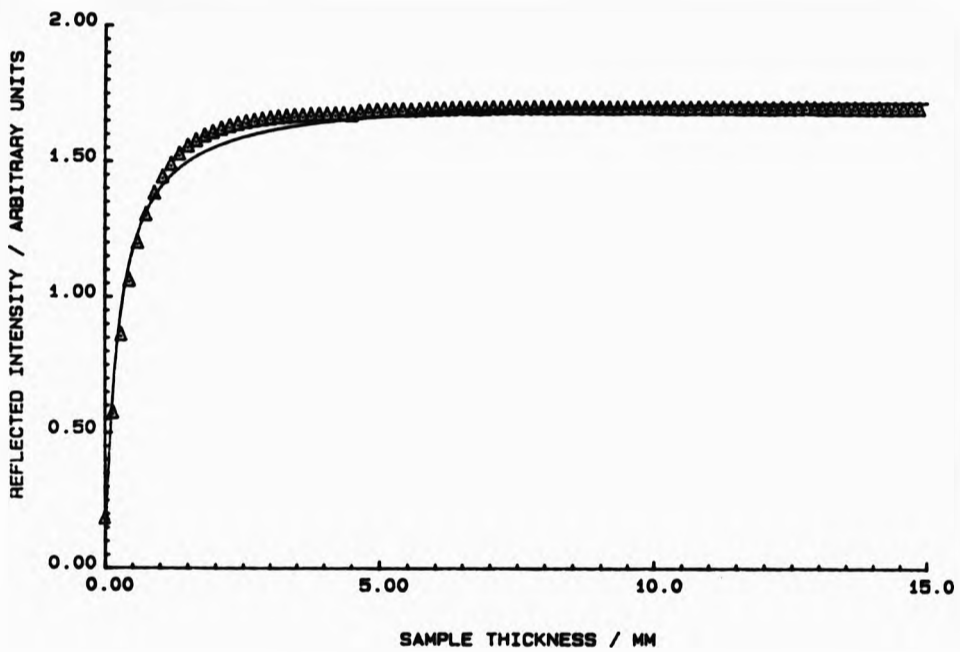


Fig (3.5.2)
 Reflected intensity as a function of illuminated sample thickness. Mean diameter = 0.73 microns. Wavelength = 589 nm. Fibre type A2, (NA=0.21). Solid line illustrates fitted curve, equation (3.3.1) with $A = 1.7$ (arbitrary units) and $S = 4.0 \text{ mm}^{-1}$.

Particle dia./microns	$S(\text{exp})/\text{mm}^{-1}$	
	Fibre K2	Fibre A2
0.11	0.76 +/- .02	0.99 +/- .04
0.25	4.1 +/- .1	3.8 +/- .1
0.37	5.0 +/- .2	4.4 +/- .2
0.48	4.8 +/- .2	4.3 +/- .3
0.73	4.5 +/- .2	4.1 +/- .2
1.05	3.8 +/- .2	3.4 +/- .1
1.43	3.7 +/- .1	3.4 +/- .1

Table (3.5.1).

Particle dia./microns	S(Mie)/mm ⁻¹	S(exp)/S(Mie)	
		Fibre K2	Fibre A2
0.11	2.87	0.26 +/- .01	0.35 +/- .01
0.25	8.19	0.49 +/- .02	0.47 +/- .01
0.37	9.01	0.55 +/- .02	0.48 +/- .02
0.48	8.84	0.60 +/- .02	0.53 +/- .02
0.73	7.03	0.64 +/- .02	0.58 +/- .02
1.05	5.95	0.64 +/- .03	0.58 +/- .02
1.43	5.02	0.70 +/- .02	0.67 +/- .02

Table (3.5.2).

These results are illustrated in fig (3.5.3) and fig (3.5.4). The solid line on these graphs represents the theoretical values of S, as computed from Mie theory and equation (2.3.49). Note, the experimental values of S on the graphs have been multiplied by a correction factor, to reduce the discrepancy between the absolute experimental and theoretical values of S. For fibre K2 the correction factor is 1/0.60. For fibre A2 the correction factor is 1/0.55.

It can be seen from fig (3.5.3) and fig (3.5.4) that the results from the two new fibre bundles broadly reflect the trends predicted by theory, (with the possible exception of the 0.11 micron sample as noted in the previous experiment). However, there is no clear relationship revealed by these experiments between the absolute values of S recorded by each fibre type, and the numerical aperture of that fibre. This is illustrated in the table (3.5.3).

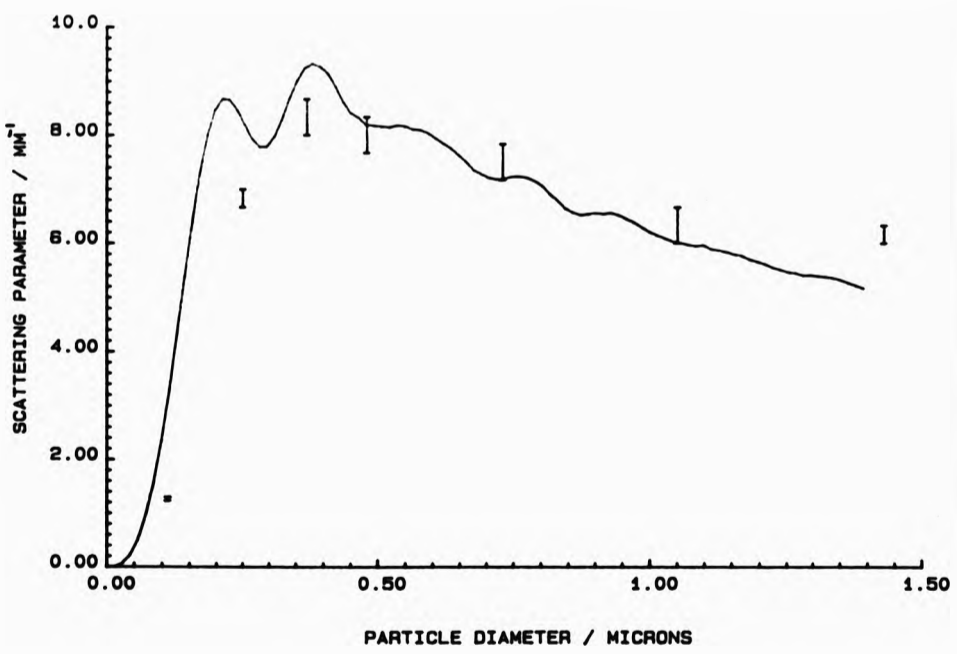


Fig (3.5.3)
Scattering parameter S as a function of mean particle diameter. Bifurcated optical fibre bundle type K2. Solid line represents theoretical curve. Wavelength = 589 nm

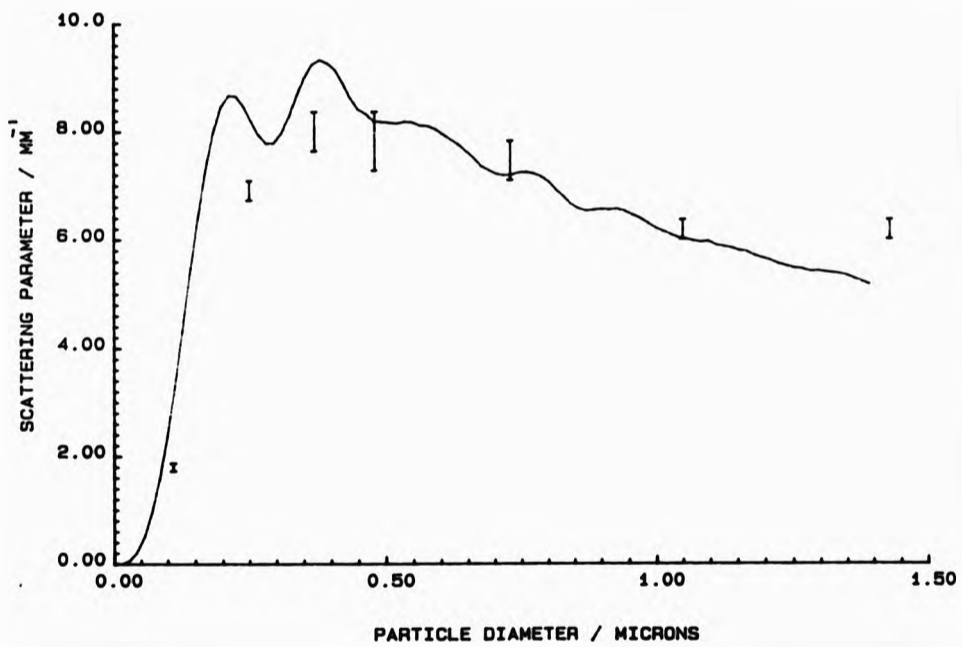


Fig (3.5.4)
 Scattering parameter S as a function of mean particle diameter. Bifurcated optical fibre bundle type A2. Solid line represents theoretical curve. Wavelength = 589 nm

Numerical Aperture	Mean value of $S(\text{the})/S(\text{Mie})$
0.21	0.60 +/- .07
0.50	0.40 +/- .04
0.66	0.55 +/- .07

Table (3.5.3).

(3.6) Conclusion.

It has been shown that the bifurcated optical fibre bundle method can be used to measure changes in the scattering parameter of colloidal dispersions. It has also been noted that the absolute value of S measured by a bifurcated bundle is highly dependent upon the separation between the influx and efflux routes within the sample. There is poor agreement between the absolute theoretical and experimental results, however the changes in S as predicted by theory are accurately reflected in the experimental results. The effect on the absolute value of S of varying the numerical aperture of the bifurcated optical fibre bundle is unclear, presumably this is due to any effect being swamped by changes in the measured value of S due to variation of the finite separation between the influx and efflux routes within the sample, between differing optical fibre bundles.

(3.7) Discussion.

The assumptions of Kubelka-Munk Theory are [40];

- (a) The scattering sample scatters light isotropically.
- (b) The sample is plane parallel, and infinite in lateral extent.
- (c) The illuminating radiation is perfectly diffuse.

It is also an implicit assumption of the boundary condition, that at $z=0$, (where the forward intensity is 1,), the reflected flux, J , is lost to the scattering system, (i.e. it is not returned to be rescattered).

There follows a brief discussion as to whether the experiment fulfills these assumptions, and what effect violations of these assumptions have on the results.

(3.7.1) Effect of non-isotropic scattering.

Anisotropic light scattering means that the light scattered from a particle is scattered preferentially forwards or backwards. Altering the ratio of back-scattering to forward-scattering does not affect the derivation of the Kubelka-Munk equation. However, the Kubelka-Munk equation allows for only two fluxes within the sample, and a single scattering parameter to relate the interchange of flux between them. More meaningful results would be obtained by considering many fluxes within the sample, with different scattering parameters to describe their interchange. The higher the number of scattering parameters,

the better the approximation to a real anisotropically scattering sample. This is essentially the approach of Mudgett and Richards [22], who considered a 22 flux theory. By comparison of their results with Kubelka-Munk theory, they obtained the result that, $S = \frac{3}{4}NC_{sa} (1 - \overline{\cos \Theta})$. Hence, anisotropic scattering modifies the interpretation of the Kubelka-Munk scattering parameter S by the factor $\frac{3}{4}(1 - \overline{\cos \Theta})$.

(3.7.2) Effect of sample geometry.

The sample geometry used in the fibre experiments is neither plane parallel, nor infinite in lateral extent. However, we might define a sample as being effectively infinite in lateral extent if a major proportion of the light travelling within the sample does not reach the horizontal glass cell walls.

From the Kubelka-Munk theory, the reflectance of a thickness d of sample, (above an absorbing boundary), is given by equation (2.3.6), i.e.

$$R = \frac{Sd}{1+Sd}$$

The diameter of the glass cell was 28 mm, the thickness of the common arm of the (thickest) bifurcated probe was approximately 10 mm. The probe to cell wall clearance was therefore approximately 9 mm. For a sample of scattering parameter 3 mm^{-1} , this gives a reflectance of 0.97. Hence for a sample of even moderate scattering, a maximum of only 3% of the input intensity could reach the cell walls. It would therefore seem reasonable to conclude that the errors in S due to the sample being non-infinite

are smaller than the experimental error, (of approximately 4 %).

Experiments were conducted to check this result. The probe to cell wall clearance was reduced to 3 mm, (by using a cell of smaller diameter), and S measured in the usual fashion four times for a latex sample of mean particle diameter 1.43 microns. The mean value of S obtained using the smaller cell was 2.3 mm^{-1} with a standard error of 0.1 mm^{-1} . This compares to a mean value of 2.25 mm^{-1} (with a standard error of 0.05 mm^{-1}), obtained for the larger diameter cell. Hence there is no difference between these results above the combined error.

A further experiment was made to study the dependence of S on the cell geometry outside the parallel slice of sample between the probe and cell base. A white collar, (of diameter 20 mm), was fitted to the common arm of the probe, flush with the probe face. S was then measured in the manner described above. The collar was then replaced with a matt black collar and S re-measured. No change in S was detected above the combined experimental error of 7 %. It would thus appear that the flux behaviour outside of the illuminated parallel slice of sample has a negligible effect on the measured value of S .

(3.7.3) Effect of non-diffuse illumination.

The illuminating radiation cannot be perfectly diffuse. Even if diffuse light were input to the optical fibres, the emergent

beam would be non-diffuse, due to the transmission characteristics of the optical fibre bundle (46).

The illumination within the sample is therefore neither perfectly diffuse, nor perfectly collimated. However if we consider the case of a collimated beam of light traversing an isotropically multiply scattering sample, then it is clear that the scattering will quickly act to diffuse the transmitted intensity. Therefore a non-diffuse illumination should quickly become diffused by the scattering sample. We might therefore expect the effect of non-diffuse illumination will be minimal, except for optical path lengths $< 1/S$, where the averaging effect of multiple scattering has not diffused the illuminating radiation.

A comparison between theories assuming collimated and diffuse illumination illustrates this point. From four-flux theory (40) the diffuse reflectance R of a semi-infinite, plane parallel, non-absorbing sample, backed by an absorbing boundary, illuminated by collimated radiation is, *from 2.3.28*

$$R = \frac{(S_1 - S)(1 - \exp(-(S_1 + S_2)d)) + (S_1 + S_2)Sd}{(1 + Sd)(S_1 + S_2)}, \quad \dots(3.7.1)$$

where S , S_1 , and S_2 are as defined in section (2.3.5).

From the comparison of four flux theory with radiative transfer theory, (section 2.3.7),

$$\begin{aligned} S &= 3/4NC_{\text{scat}}(1 - \overline{\cos\theta}), \\ S_1 &= NC_{\text{scat}}(1/2 + 3/4\overline{\cos\theta}), \\ S_2 &= NC_{\text{scat}}(1/2 - 3/4\overline{\cos\theta}). \end{aligned}$$

For low values of $S_3 d$, (i.e. $S_3 d \ll 1$), we can make the approximation that,

$$1 - \exp(-4/3(S_1 + S_2)d) = 4/3(S_1 + S_2)d$$

hence we obtain,

$$R = \frac{S_2 d}{(1 + Sd)} \quad \dots(3.7.2)$$

For large values of $S_3 d$, (i.e. $S_3 d \gg 1$), we can make the approximation that,

$$1 - \exp(-4/3(S_1 + S_2)d) = 1,$$

hence we obtain,

$$R = \frac{Sd}{(1 + Sd)} \quad \dots(3.7.3)$$

The equivalent expression derived from Kubelka-Munk theory, (which assumes diffuse illumination), is,

$$R = \frac{Sd}{(1 + Sd)} \quad \dots(3.7.4)$$

Hence for samples with $Sd \gg 1$ the observed reflectance is unaltered by the use of collimated or diffuse incident flux, and the reflectance of the sample is as predicted by the Kubelka-Munk equation. However for low values of Sd the reflectance is dependent upon the mode of illumination, and the Kubelka-Munk expression does not accurately predict the reflectance of the sample. In the experiments conducted here the value of Sd is varied, hence an imperfect fit will be obtained when using the Kubelka-Munk equation. For positive values of $\overline{\cos\theta}$ $S_1 < S$, we might therefore expect that the value of S obtained by fitting the results obtained for collimated illumination to the Kubelka-Munk equation will return values of S less than the actual value. This was confirmed by generating reflectance values as a function of sample thickness using the four-flux equation (3.7.1) with $\overline{\cos\theta} = 1$. The

data so generated was fitted to the Kubelka-Munk equation (3.7.4). The fit returned values of S that were dependent upon the maximum value of S_d to which the data was fitted. So long as the maximum value of S_d exceeded 5 the fitted value of S was within 4 % of the value used to generate the data from equation (3.7.1). The fitted value was always less than the value used to generate the data. The quality of the fit obtained was good, better than that obtained between the experimental data and the Kubelka-Munk expression. For all the samples used in the experiments S_d was greater than 5, hence even if total collimation of light is assumed, (the worst possible case), a maximum error of only 4 % is introduced by assuming diffuse illumination, (i.e. fitting to the Kubelka-Munk expression). The degree of collimation of the incident light is dependent upon the numerical aperture of the illuminating fibres. The experiments with fibres of differing numerical apertures might therefore be expected to show an increase in the measured value of S as the numerical aperture is increased. However no clear trend was observed in the results, (see section 3.5).

It is important to note that the optical fibre bundle will not detect the reflected diffuse flux evenly over the whole of its angular range. However if the reflected flux is perfectly diffuse then this will not affect the results. The fibres will simply detect a constant proportion of the reflected diffuse intensity. This does however assume that the reflected flux is perfectly diffuse whatever the sample thickness.

(3.7.4) Interfacial reflections.

We now consider the light that is reflected back into the sample at the probe face due to internal interfacial reflection. If we assume that some fraction α of the reflected diffuse intensity is reflected from the probe end, then the forward flux at the $z=0$ boundary, i.e. the probe end, is not 1, but $1 + \alpha j$. This modifies the boundary conditions applied in the derivation of the Kubelka-Munk equations. Applying the modified boundary condition yields the expression for the observed diffuse reflectance R,

$$R = \frac{(1-\alpha)j(0)}{1} = \frac{(1-\alpha)Sd}{1+(1-\alpha)Sd} \quad \dots(3.7.5)$$

Hence fitting the results to the equation $R=Sd/(1+Sd)$ will return values of S that are a factor $(1-\alpha)$ less than the actual value of S. The diffuse reflectance of the fibre/sample interface was calculated to be 0.028 [47], (see Appendix II). Hence the fitted value of S will be approximately 3 % less than the actual value due to interfacial reflections at the probe/sample interface. This alone cannot account for the large discrepancy between the experimental and theoretical results.

In conclusion then it can be said that:

- (1) The interpretation of the Kubelka-Munk scattering parameter is modified by a factor $3/4(1-\overline{\cos\theta})$ due to anisotropic scattering.
- (2) The effect of the sample being non-infinite and non-parallel over the whole of its lateral extent is negligible, so long as the illuminated thickness of sample is parallel.
- (3) The use of non-diffuse illumination reduces the value of S

obtained by a maximum of 4 % so long as $Sd > 5$.

(4) The effect of internal interfacial reflections, between the sample and probe face, is to reduce the measured value of S by a factor $(1-\alpha)$, where α is the diffuse internal reflectance of the interface. For the fibre bundle used here $\alpha = 0.03$, therefore the reduction in the measured value of S is small, of the order of the experimental error.

The combination of factors (3) and (4) will reduce the measured value of S by a maximum of only 7 % from its actual value. These effects cannot therefore account for the fact that experimental values of S are only approximately 40 % of the theoretical values.

CHAPTER 4: SINGLE OPTICAL FIBRE EXPERIMENTS.

(4.1) Introduction.


In an effort to quantify the effects of having a finite separation between the influx and efflux routes within the samples, experiments were conducted using single, separate optical fibres. This allowed the separation between the influx and efflux routes within the sample to be controlled.

Two experimental methods are described in this chapter. The first is a simple system to demonstrate that changes in S can be measured using separate, single, optical fibres, mounted in an absorbing boundary. The second system utilizes separate optical fibres to illuminate and detect the reflected flux from a parallel slice of sample of variable thickness. Thus allowing absolute measurements of S to be obtained for varying separation between the influx and efflux routes within the sample.

The optical fibres used throughout these experiments were polymer, step indexed, multimode fibre, of numerical aperture 0.47 and diameter approximately 1 mm.

(4.2) Fixed path length, separate fibre system.

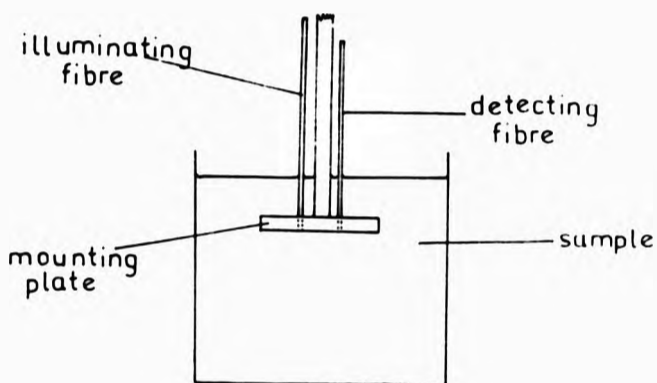
The fibre optic system developed was an adaption of that developed by Boersboom and Ten Borsch [48] to measure multiple scattering in solid samples. The system consisted of two fibres,



mounted on a circular plate, (of diameter 2.0 cm), with a nearest edge separation of 2.1 mm, placed within a cylindrical glass sample cell. The face of the mounting plate was painted matt black to provide the absorbing boundary. The fibres were polished flat with the mounting plate, and positioned approximately centrally on the mounting plate. The sample cell consisted of a glass cylinder of diameter 5 cm, 5 cm long, with a flat glass base. The mounting plate was positioned centrally in the filled sample cell, approximately 3 cm from the base of the cell, see fig(4.2.1).

From Kubelka-Munk theory, a sample of scattering power 2.9 mm^{-1} , (the minimum scattering parameter of any sample used in this experiment), and thickness 3 cm would reflect 99 % of the incident flux. Hence, for the samples used here 3 cm is to a good approximation an infinite thickness of sample. The dominant absorbing surface is therefore the matt black fibre mounting plate.

The fibres were held in this position throughout the experiment and the scattering sample changed. The same monodisperse spherical latex particles suspended in de-ionized water, (at a volume fraction of 0.0238), as used previously, provided the scattering samples. The same illumination and detection systems as detailed in chapter three were used, the detected light being filtered to 589 nm immediately before the photodetector. The input intensity was held constant throughout the experiments. The intensity reflected from the sample, through the output fibre, was recorded for each sample.



Fig(4.2.1)
Optical fibre mounting.

(4.2.1) Results.

Table (4.2.1) illustrates the reflected intensities, as a function of the mean particle diameter of each sample.

Particle Diameter/ microns	Intensity Detected/ Arbitrary Units.
0.11	0.33 +/- .02
0.25	0.070 +/- .003
0.37	0.043 +/- .002
0.48	0.063 +/- .002
0.54	0.063 +/- .003
0.95	0.067 +/- .002
1.43	0.12 +/- .01

Table (4.2.1)

4.2.2) Analysis of results.

Fig (4.2.2) illustrates a log-log plot of the intensity as a function of theoretical scattering parameter, as calculated from equation (2.3.49).

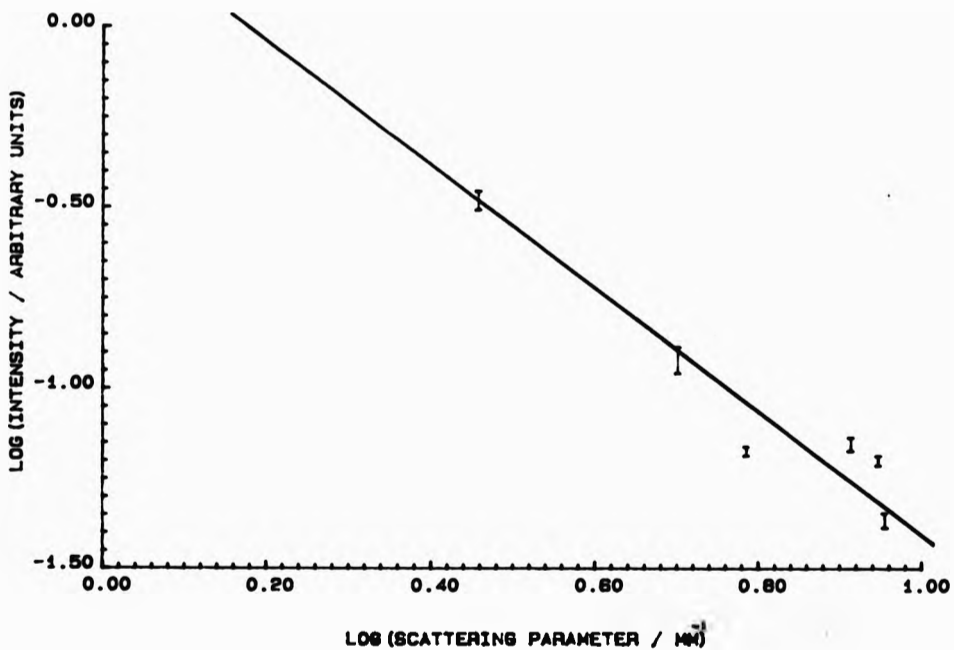


Fig (4.2.2)
The log of the reflected intensity as a function of the log of the theoretical scattering parameter of the sample. Solid line shows fitted curve of gradient $-(1.6 \pm .2)$.

It can be seen from fig (4.2.2) that there is an approximately linear relationship between the log of the reflected intensity and the log of the theoretically calculated scattering parameter. The

fitted line gives,

$$I \propto \frac{1}{S^{1.6}}$$

or

$$S \propto \frac{1}{I^{0.625}} \quad \dots(4.2.1)$$

Fig (4.2.3) illustrates the experimental scattering coefficient as calculated from equation (4.2.1) as a function of mean particle size. The solid line on fig (4.2.3) illustrates the theoretical value of S as calculated from equation (2.3.49).

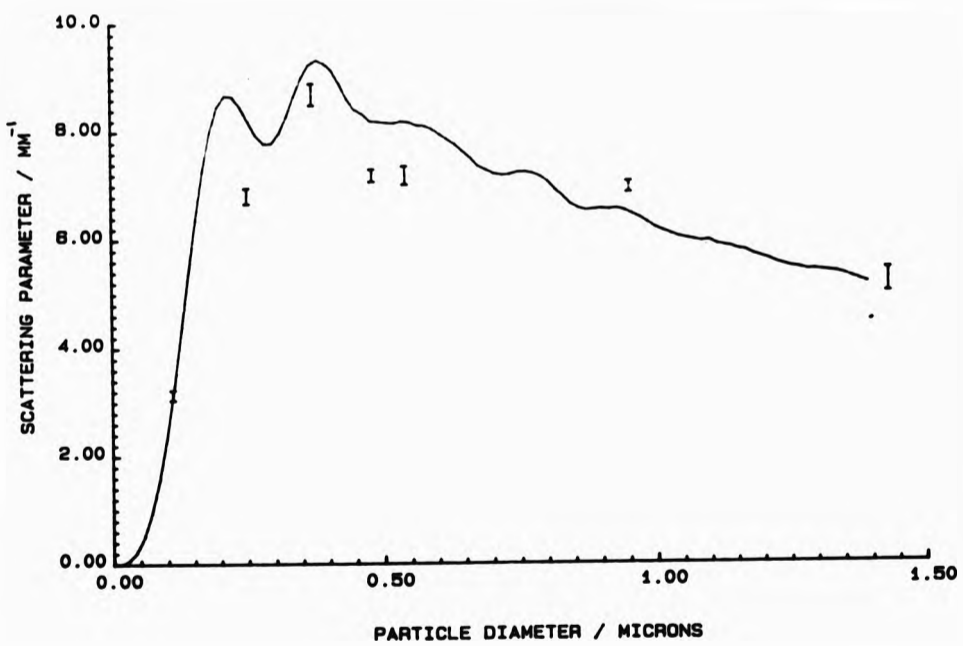


Fig (4.2.3)
S as a function of particle size as calculated from the experimental results and equation (4.2.1). The solid line represents the theoretical curve calculated from equation (2.3.49).

Let us assume that the optical output from the influx fibre is perfectly diffuse, and that the absorption of the scattering sample

is negligible. The optical power P falling on an imaginary hemisphere of radius r , centered on the influx fibre is then,

$$P(r) = I(r) \cdot 4\pi r^2,$$

or
$$I(r) = \frac{P(r)}{4\pi r^2} \quad \dots(4.2.2)$$

The only absorption present is that due to the matt black mounting plate. Assuming that all the light incident on the plate is absorbed, then in increasing the imaginary sphere radius from r to $r+dr$, the change in the optical power is,

$$dP(r) = -I(r) 2\pi r dr. \quad \dots(4.2.3)$$

Hence from (4.2.2),

$$dP(r) = \frac{-P(r) dr}{2r},$$

or
$$\frac{dP(r)}{P(r)} = \frac{-dr}{2r}.$$

Hence,
$$P(r) = \frac{C}{r^2}$$

where C is a constant of integration. Therefore from (4.2.2),

$$I(r) = \frac{C}{4\pi r^2} \quad \dots(4.2.4)$$

The output intensity is solely dependent upon;

- (i) the input intensity I_0 ,
- (ii) the scattering parameter of the sample S ,
- (iii) the separation of the optical fibres within the sample.

Hence,
$$I \propto I_0 S^2 r^2 \quad \dots(4.2.5)$$

Equation (4.2.4) gives $z = -2.5$. A dimensional analysis of (4.2.5) gives $y = -2.5$. Hence,

$$S \propto \frac{1}{\sqrt[2.5]{I}} \quad \dots(4.2.6)$$

This compares with the empirical equation,

$$S \propto \frac{1}{r^2}$$

The agreement between the theoretically derived equation and the empirical equation is poor. This may be due to the illuminating radiation being non-diffuse. In practice, for low values of r , little of the intensity from the input fibre would be incident on the matt black mounting plate. This would tend to decrease the dependence of the intensity on the distance from the input fibre, r .

(4.2.3) Conclusion.

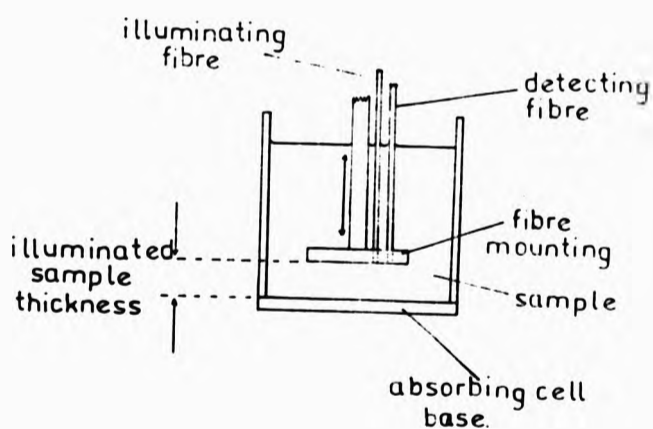
It has been shown that two optical fibres mounted in an absorbing mounting can be used to measure changes in the scattering parameter of optically thick colloidal samples. Absolute measurements of the scattering parameter can be made using such a method if the instrument has been previously calibrated.

(4.3) Variable path length, separate optical fibre system.

This experiment worked on the same principles as the bifurcated optical fibre experiment, detailed in Chapter 3. A parallel slice of sample, above an absorbing boundary, was illuminated. The reflectance of the sample was monitored as a function of sample thickness. Two single fibres provided the illumination and detection routes to the sample. The use of two

separate optical fibres allowed the distance between the influx and efflux routes to be varied by altering the fibre separation.

The two fibres were mounted in and polished flat with a cylindrical aluminium mounting plate, (of diameter 2.0 cm). The mounting plate surface, being polished aluminium, was highly reflecting. The same movement, detection and illumination systems as detailed in chapter three were employed, and the output intensity filtered to 589 nm.



Fig(4.3.1)
Fibre mounting and sample cell geometry.

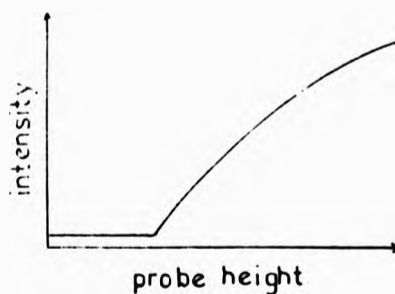
The sample cell consisted of a glass cylinder of radius 26mm with a matt black plastic base. Care was taken to ensure that the cell base and fibre mounting were parallel before commencing the experiment.

Experiments were carried out on two samples of monodisperse

spherical latex particles suspended in deionized water (at a volume fraction of 0.024), of mean particle diameters 1.43 and 0.54 microns. The reflected intensity as a function of sample thickness was measured for sample thicknesses between 0.00 and 4.95 mm, (in 0.05 mm steps), for a range of input-output fibre separations. The fibre ^{edge to edge} separations were measured using a travelling microscope.

(4.3.1) Results.

It was found that as the fibre separation was increased a flat region developed in the intensity readings for low sample thicknesses. This is shown schematically in fig (4.3.2).



Fig(4.3.2)
Schematic illustration of flat region in intensity.

This can be explained by considering the light traversing the sample from the input to output fibre. The input intensity is not diffuse, but restricted to the forward direction by the numerical aperture of the fibre, (N.A. = 0.47). Hence for low



sample thicknesses the input intensity is directly incident upon the absorbing cell base before it can be diffused by the scattering of the sample. Therefore, at low sample thicknesses the majority of the input intensity is immediately absorbed. The intensity detected at low sample thicknesses is hence very low, and largely independent of the sample thickness. Until an appreciable fraction of the input intensity is scattered sideways before it reaches the absorbing cell base, i.e. when the sample thickness is of the order of $1/S$, little change in intensity with sample thickness will be detected.

It is clear that Kubelka-Munk theory is inapplicable over these flat regions. In an attempt to overcome this problem, and to provide consistent fitting conditions for all the results, intensity readings for illuminated sample thicknesses between 0.0 and 0.50 cm were neglected from all data sets. The remaining data was fitted to the non-absorbing Kubelka-Munk equation, equation (2.3.6),

$$R = Sd/(1+Sd),$$

using a fitting programme employing a least squares fitting method.

The fitting results are presented in table (4.3.1) and (4.3.2).

Fibre Separation / mm	Fitted Value of S / mm ⁻¹
0.01 +/- .01	11 +/- 1
0.09 +/- .02	6.2 +/- 0.4
0.23 +/- .02	4.0 +/- 0.3
0.32 +/- .02	2.6 +/- 0.1
0.45 +/- .02	2.3 +/- 0.1
0.60 +/- .02	1.6 +/- 0.1

Table (4.3.1)
0.54 micron sample. Wavelength = 589 nm.



Fibre Separation / mm	Fitted value of S / mm ⁻¹
0.01 +/- .01	8.1 +/- .4
0.07 +/- .02	6 +/- 1
0.09 +/- .02	5.2 +/- .4
0.17 +/- .02	4.1 +/- .2
0.22 +/- .02	3.7 +/- .1
0.29 +/- .02	3.0 +/- .2
0.42 +/- .02	2.3 +/- .1
0.55 +/- .02	2.1 +/- .1

Table (4.3.2)
1.43 micron sample. Wavelength = 589 nm.

Examples of the data obtained are illustrated in fig(4.3.3) and (4.3.4).

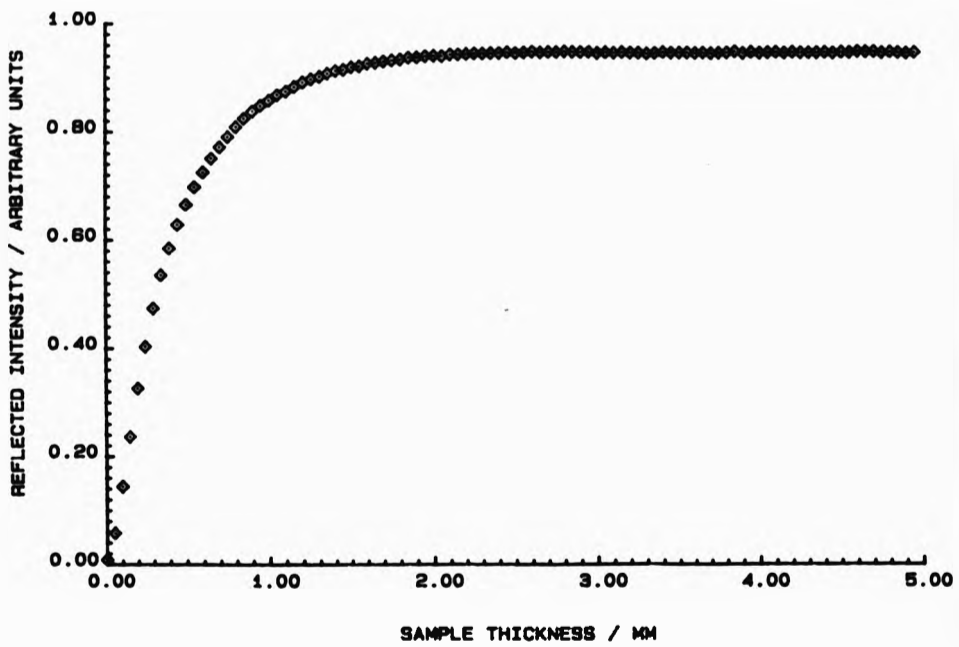


Fig (4.3.3)
Reflected intensity as a function of illuminated sample thickness. 0.54 micron sample. Solid line shows fitted Kubelka-Munk expression. Fibre separation = 0.01 +/- .01 mm.

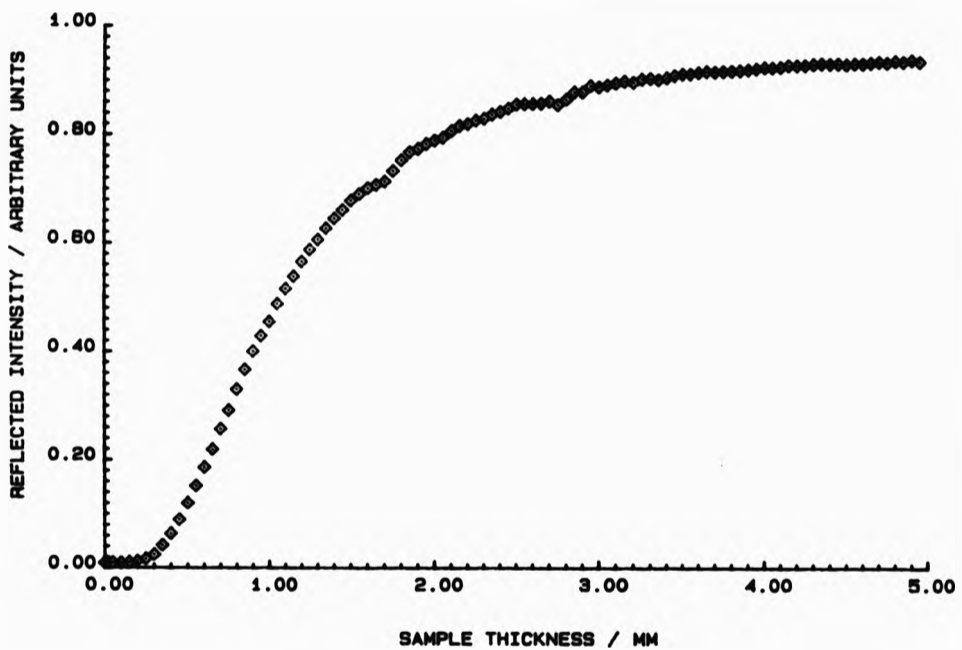


Fig (4.3.4)
Reflected intensity as a function of illuminated sample thickness. 0.54 micron sample. Solid line shows fitted Kubelka-Munk expression. Fibre separation = 0.60 +/- .02 mm.

The fitted value of S as a function of fibre separation is illustrated in fig (4.3.5). The solid line on fig (4.3.5) represents a curve of the form,

$$S = A/(1+Bd).$$

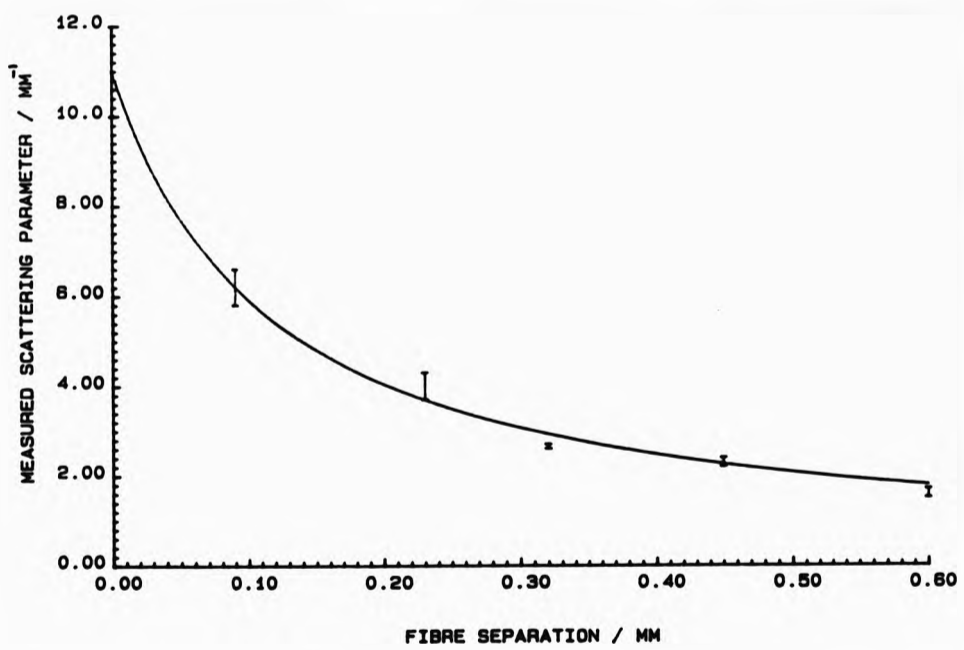


Fig (4.3.5)
Fitted value of S as a function of fibre separation.
0.54 micron diameter sample. Wavelength = 589 nm.

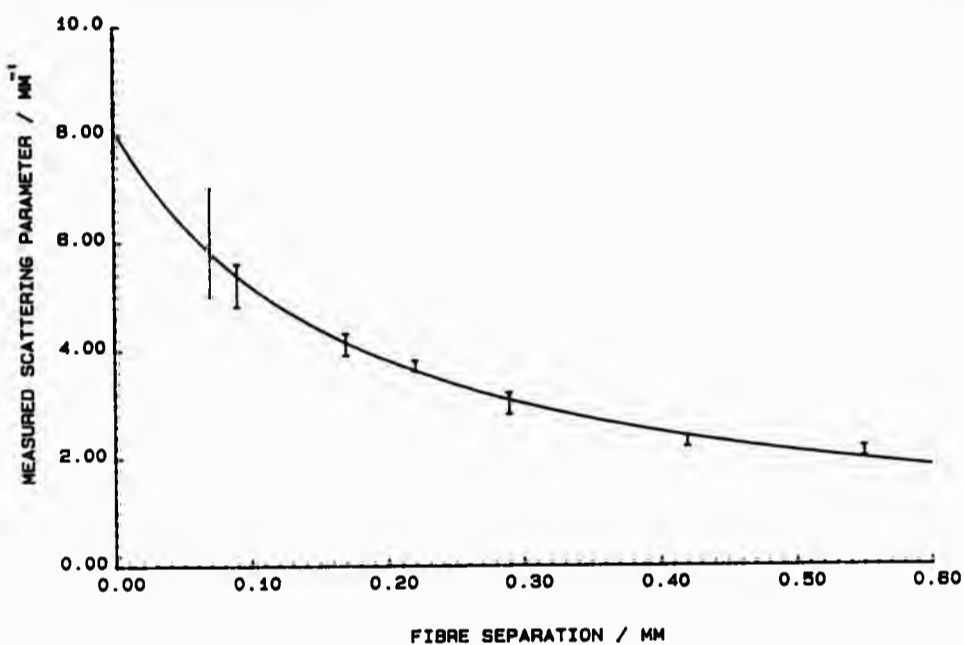


Fig (4.3.6)
 Fitted value of S as a function of fibre separation.
 1.43 micron diameter sample. Wavelength = 589 nm.

(4.3.2) Conclusion.

It has been shown that the value of S obtained by performing a Kubelka-Munk fit on reflected intensity data as a function of illuminated sample thickness, (above an absorbing boundary), from optical fibres with a finite separation, is highly dependent upon that fibre separation. This has important implications for the bifurcated optical fibre system. The influx and efflux routes in that system are physically separate, we cannot therefore expect to obtain values of S from the system that agree well with the theoretical value of S .

CHAPTER 5: SINGLE OPTICAL FIBRE BUNDLE AND BEAMSPLITTER

EXPERIMENTS.

(5.1) Large diameter bundle.

The conclusions reached from the previous experiments suggest that any reduction in the separation between the input and output routes from the sample will improve the agreement between the experimental and theoretical results. It is possible to use a single fibre to provide both input and output routes by using a beam splitter arrangement. See fig (5.1.1).

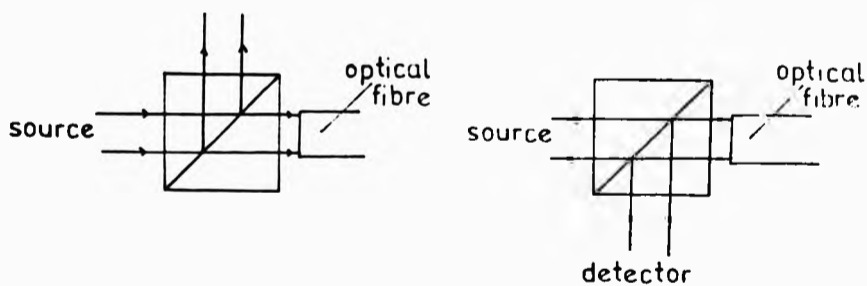


Fig (5.1.1)
Separation of input and output
beams by the use of a beamsplitter.

The use of a single fibre bundle greatly reduces the distance between the input and output routes from the sample. However a disadvantage with this system is that 50 % of the input intensity focussed on the beam splitter is lost before it reaches the fibre. Similarly 50% of the output intensity from the fibre, (the light

reflected from the sample), is lost before it reaches the detector. Hence only a maximum of 25 % of the input intensity can reach the detector, (even if 100 % of light incident on the sample is reflected and detected). In addition, due to imperfect beam splitting and interfacial reflections between the fibre and beam splitter, some input intensity is directly reflected into the photodetector. The magnitude of this intensity is large compared with the output intensity from the sample, (approximately 5 times larger). The interfacial reflections between the beam splitter and fibre were minimized by using Glycerol as an index matching fluid between the fibre and beam splitter.

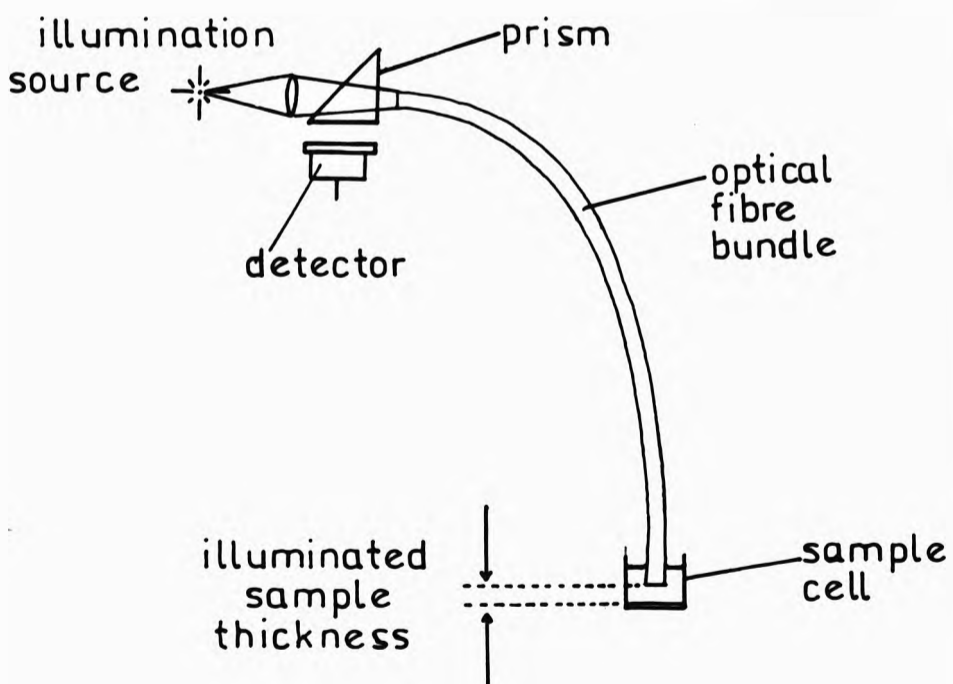



Fig (5.1.2)
Single bifurcated bundle experimental system.



A single optical fibre bundle of diameter (6.7 ± 0.1) mm and NA 0.5 was used to illuminate the sample and to detect the reflected flux. A prism was used to separate the input and output intensities.

The same illumination, detection and stepper motor movement systems as described previously in chapter three were used. The non-illuminated end of the optical fibre bundle was placed within the sample cell and moved upwards from the absorbing base, the reflected intensity being measured as a function of illuminated sample thickness. The results were analysed by fitting to equation (3.2.2). The sample cell consisted of a 28 mm diameter glass cylinder with a matt black plastic base. The samples used were monodisperse spherical latex particles suspended in de-ionized water at a volume fraction of 0.0238. To measure the intensity offset necessary to account for imperfect beam splitting, (resulting in some light being incident upon the photodetector without having been scattered by the sample), the output from the photodetector amplifier was zeroed, (using an offset control on the amplifier), with the end of the fibre bundle placed in a Rayleigh horn.

Typical experimental results are illustrated in fig (5.1.3). The solid line illustrates the fitted curve, equation (3.2.2).

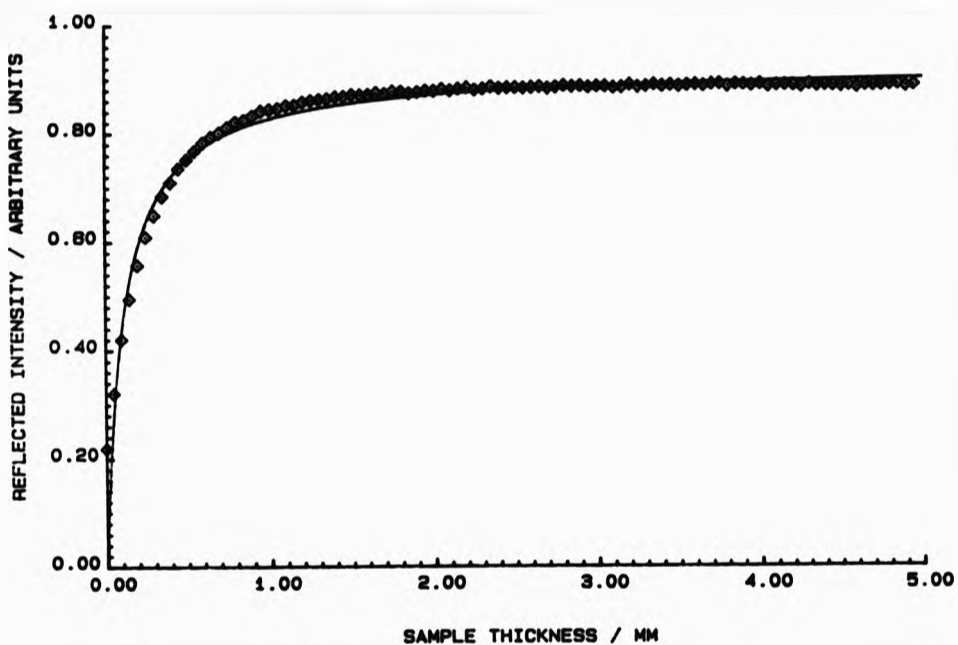


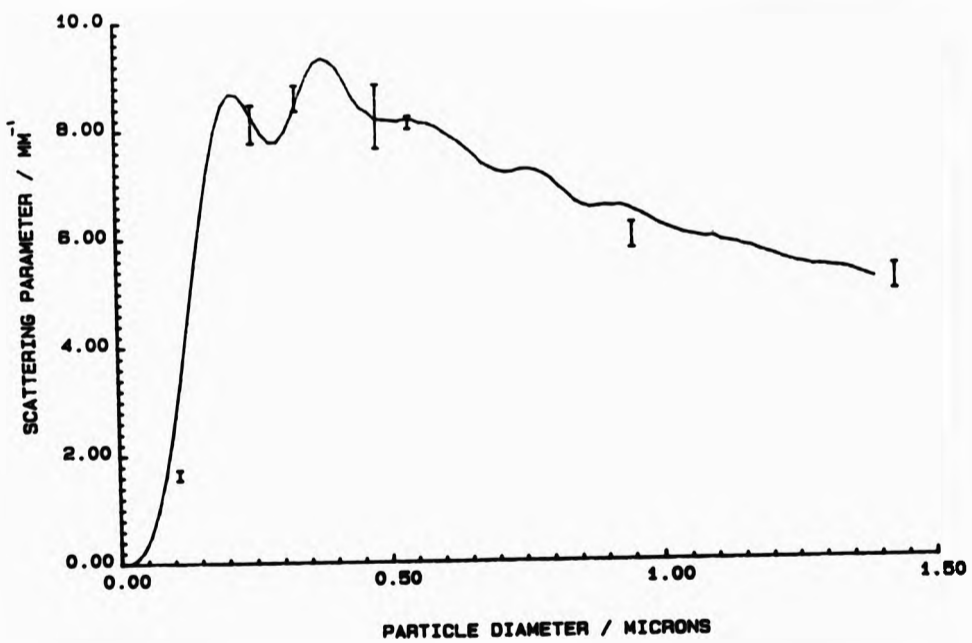
Fig (5.1.3)
 Reflected intensity as a function of illuminated sample thickness. 0.33 micron sample at 589 nm. Solid line is the fitted theoretical curve, equation (3.2.2).

(5.1.1) S as a function of particle size.

Table (5.1.1) gives the fitted values of S as a function of mean particle size. The quoted value of S is the mean value obtained from four experiments on the same sample. The quoted error is the standard error of the four results. The table also compares the theoretical and experimental values of S.

Particle Diameter / microns	S(exp)/mm ²	S(Mie)/mm ²	S(exp)/S(Mie)
0.11	1.40 +/- .08	2.77	0.51 +/- .02
0.25	6.9 +/- .3	8.20	0.84 +/- .04
0.33	7.3 +/- .2	8.39	0.87 +/- .02
0.48	7.0 +/- .5	8.20	0.85 +/- .06
0.54	6.9 +/- .1	8.10	0.85 +/- .01
0.95	5.1 +/- .2	6.10	0.84 +/- .02
1.43	4.4 +/- .2	5.05	0.87 +/- .04

Table (5.1.1)



Fig(5.1.4)

Fitted value of S as a function of particle size, experimental results multiplied by a factor of 1.18 to reduce the discrepancy between experimental and theoretical results. Solid line illustrates theoretical result, equation (2.3.49).

It can be seen from table (5.1.1) that there is a much

improved agreement between the experimental and theoretical results. An average $S(\text{experimental})$ to $S(\text{theoretical})$ ratio of 0.85 \pm .01 was obtained for the single fibre bundle system, compared with a ratio of 0.40 \pm .04 for the bifurcated fibre system. The only discrepancy in the results is that for the 0.11 micron sample. It can be seen from fig (5.1.4) that this may be due to an over-estimation of the particle size.

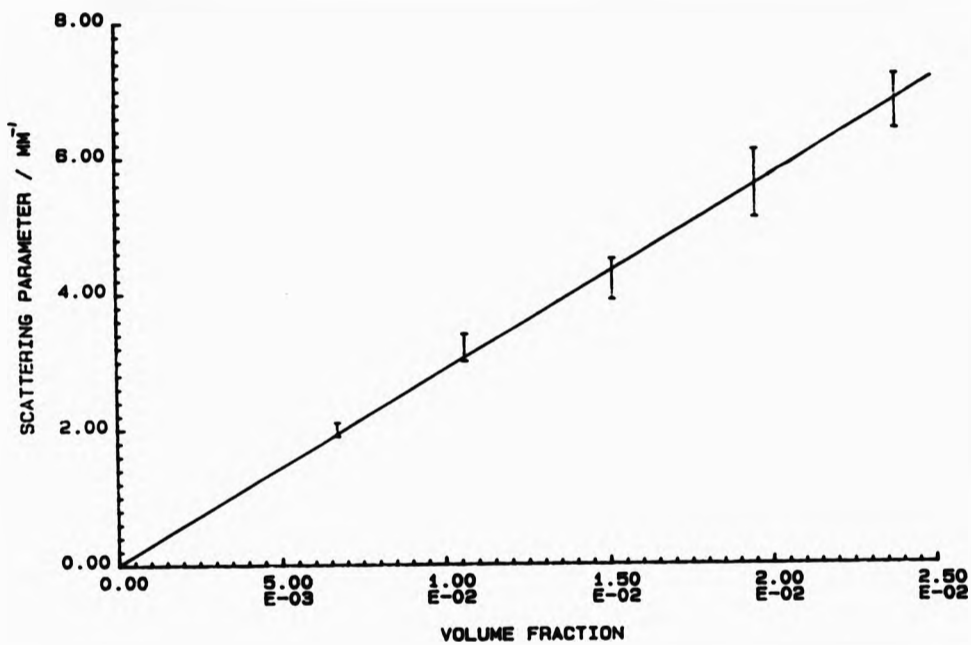
The solid line in fig (5.1.4) represents the theoretical curve. Note that the experimental results have been multiplied by a factor of 1/.85 to reduce the discrepancy between the experimental and theoretical results.

(5.1.2) S as a function of concentration.

Experiments were conducted to check the linearity of response of the system, (i.e. whether the measured value of S varies linearly with the theoretical value). Experiments were conducted on a 0.25 micron mean diameter sample. The sample was diluted with de-ionized water and the reflectance of the sample measured as a function of illuminated sample thickness. The fitting results are presented in table (5.1.2) and illustrated in fig(5.1.5).

Volume Fraction of Latex.	Fitted value of S/mm^2
0.0238	6.8 \pm .4
0.0195	5.6 \pm .5
0.0151	4.2 \pm .3
0.0106	3.2 \pm .2
0.0067	2.0 \pm .1

Table (5.1.2)



Fig(5.1.5)
 Measured value of S as a function of sample concentration. Particle diameter = 0.25 μm .
 Wavelength = 589 nm.

The equation relating the scattering parameter S to the single scattering (Mie) parameters is;

$$S = \frac{3}{4}NC_{\text{ext}}(1 - \overline{\cos\theta})$$

If this equation is valid, then there should be a linear relationship between the number concentration N, (or volume fraction v), and the scattering parameter S. Experiment shows that S is closely proportional to v, hence validating the N dependence of the above equation and suggesting a linearity in the method with respect to changes in S. It is later shown that S is

not proportional to N at higher concentrations. This can be explained in terms of particle-particle interactions.

(5.2) Small diameter bundle.

Assuming theory to be correct there still remains the question as to why the system does not return values of S that are equal to the theoretical value. This may be explained as follows. Light flux input to the sample through one fibre does not return to the detector solely through that fibre. There will be a sideways translation of a proportion of the light, resulting in some of the light input from one fibre exiting the sample through another. Hence, there is an effective finite separation between the influx and efflux routes. This effect will be larger the larger the diameter of the fibre bundle, as the maximum distance between the influx and efflux routes will be equal to the fibre bundle diameter. To test this hypothesis, a second experiment was carried out using a smaller diameter, ($3.0 \pm .01$ mm), fibre bundle, with the same numerical aperture, (0.5) as the previous fibre bundle. The same illumination, detection, movement, beam splitter, sample cell and cell mounting system detailed in the previous experiment were used. As before the reflected intensity as a function of illuminated sample thickness was recorded and fitted using a least squares simplex method to equation (3.2.2).

(5.2.1) S as a function of particle size.

Table (5.2.1) presents the results for the 3.0 mm diameter fibre bundle experiments. The table also compares the theoretical and experimental results.

Particle Diameter/ microns.	S(Mie)/mm ⁻¹	S(Exp)/mm ⁻¹	S(Exp)/S(Mie)
0.085	1.63	1.43 +/- .08	0.88 +/- .01
0.25	8.19	7.3 +/- .3	0.89 +/- .03
0.33	8.38	8.2 +/- .5	0.98 +/- .06
0.48	8.19	7.5 +/- .2	0.91 +/- .03
0.54	8.09	7.4 +/- .2	0.91 +/- .02
1.05	6.00	5.7 +/- .1	0.95 +/- .02
1.43	5.05	4.9 +/- .1	0.97 +/- .02

Table (5.1.3).

It can be seen by a comparison with the S(exp)/S(Mie) ratio in table (5.1.2) that the agreement between the experimental and theoretical results is improved by the use of smaller diameter optical fibre bundle. An S(exp)/S(Mie) ratio of 0.93 +/- .03 is obtained for the 3.0 mm diameter bundle, compared with 0.85 +/- .01 for the 6.7 mm diameter bundle. There is still a discrepancy of approximately 7 % between the experimental and theoretical results, of which approximately one half is accounted for by the effects of interfacial reflections, (see section 3.5.4). The remaining 4 % may well be accounted for by there being a still finite separation between the influx and efflux routes.

(5.3) Conclusion.

It has been shown that the agreement between the experimental and theoretical values of S has been much improved by the use of a

single fibre bundle to both illuminate the sample and to detect the reflected flux. This has been explained in terms of the influx-efflux route separation.

It has been shown that the single fibre bundle has a linear response to changes in S and the N dependence of equation (2.3.49) has been validated for volume fractions between 0.007 and 0.024.

CHAPTER 6: THE INTEGRATING SPHERE.

(6.1) Introduction.

This investigation was conducted to provide an independent, (i.e. non-fibre), measurement of the scattering parameter S . It should however be recalled that such measurements require large corrections [32,33] owing to the refractive index mis-match between the air and the sample.

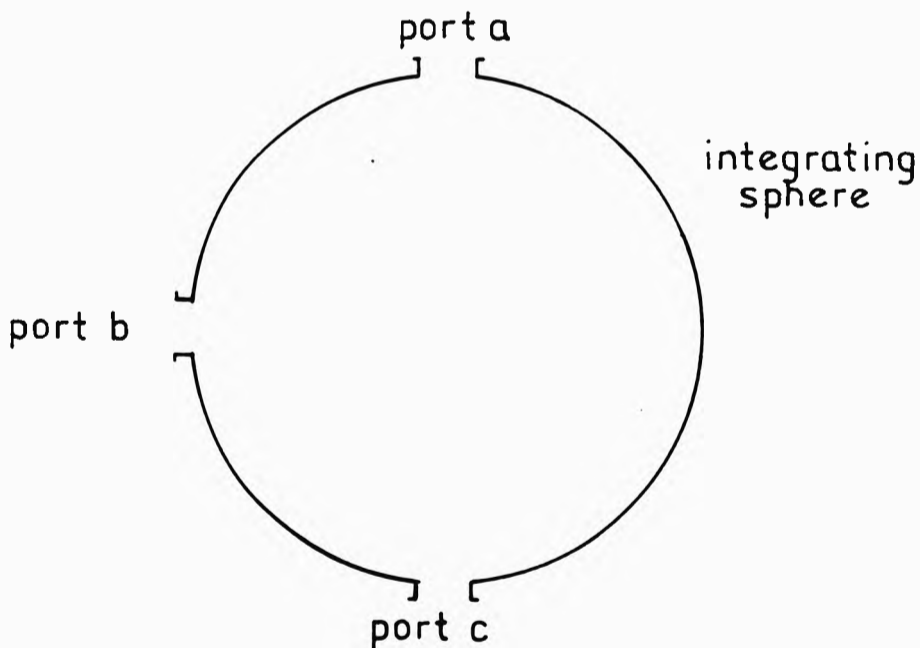


Fig (6.1.1)
The integrating sphere.

The integrating sphere is a hollow sphere, internally coated with a highly diffuse reflective coating, (an albedo of 0.97 is typical).

Suitable apertures around the sphere allow for illumination, detection and insertion of the scattering sample. The sample may be illuminated directly by the source, (sample at a, illumination through c, detector at b, see fig (6.1.1)). In this mode of operation most of the specular reflections from the sample are lost through the input aperture c. Only the diffusely reflected radiation is observed by the detector at b, see fig (6.1.2).

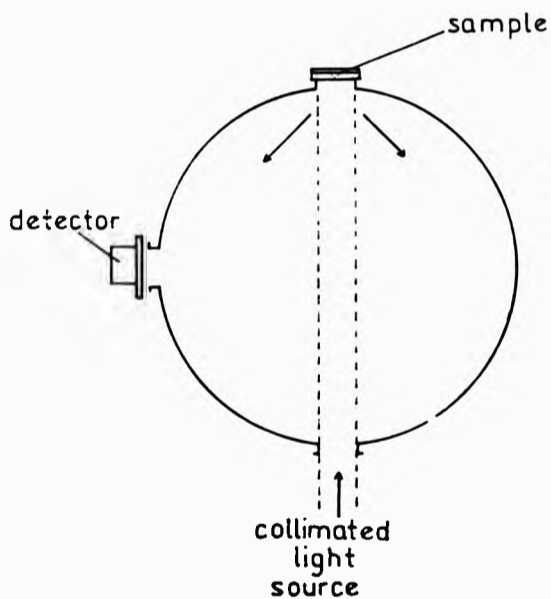
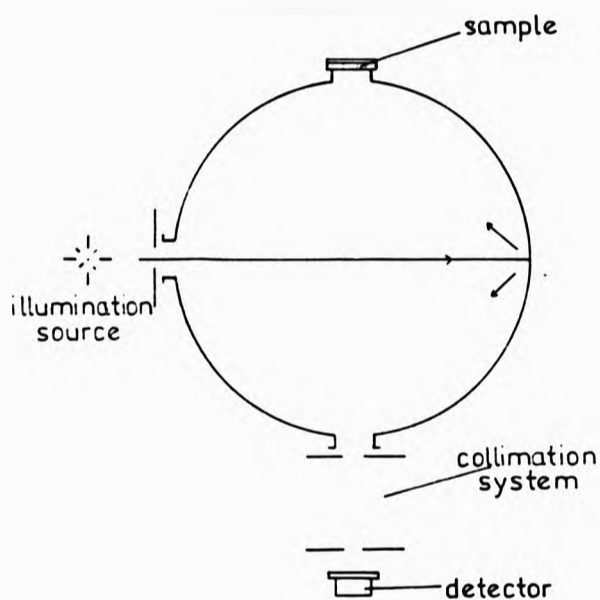


Fig (6.1.2)
Collimated illumination, diffuse detection.

Alternatively the sample may be illuminated indirectly, and diffusely, by placing the sample over aperture a and illuminating the side of the integrating sphere through b, see fig (6.1.3). The light input through b is diffusely reflected around the sphere

until it is incident upon the sample at a, it is then, to a good approximation, diffuse.



Fig(6.1.3)
Diffuse illumination, collimated detection.

The detector at c then measures only the diffuse light reflected from the sample.

The integrating sphere relies upon the sphere acting to diffuse any light falling upon it. To approach this ideal the internal coating should be perfectly diffusely reflecting, and the ratio of aperture cross-section to the sphere's internal area must be vanishingly small [33]. The sphere used in these experiments had an internal diameter of 150 mm and three apertures of cross-sectional area 804 mm^2 , giving an internal surface area to

aperture area ratio of approximately 0.035.

(6.2) Experimental method.

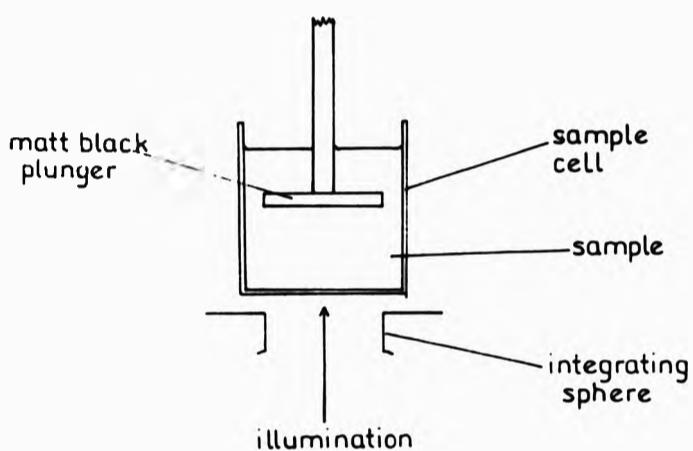
The standard method of use of an integrating sphere is to illuminate a known thickness of sample backed by a tile of known absorbance and measure the combined diffuse reflectance of the sample and tile. The scattering power of the sample may then be calculated from the equation,

$$R = \frac{a+(1-a)Sd}{1+(1-a)Sd} \quad \dots(6.2.1)$$

where a is the reflectance of the backing tile.

There seemed little to be gained by using this method to evaluate S . Hence, as previously the reflected intensity was measured for varying sample thicknesses above an absorbing boundary. The results were fitted to equation (6.2.1), with the quantity a left as a floating parameter in the fit to account for the finite reflectance of the absorbing boundary.

The stepper motor movement system developed earlier was adapted to move a matt black plastic plunger upwards through a cylindrical glass sample cell with a glass base, see fig (6.2.1). The sample cell was filled with a scattering sample and placed on top of aperture a , the sample was then illuminated, and the plunger moved upwards through the sample.



Fig(6.2.1)
Sample cell and absorbing boundary.

Experiments were conducted using a white light source with the sample under direct, (collimated) illumination, and diffuse detection, (sample at a, illuminated through c, detector at b). The experiments were then repeated for indirect, (diffuse), illumination and direct (collimated) detection, (sample at a, sphere wall illuminated through b, detector at c). Experiments were also conducted using direct laser (10mW HeNe, 633 nm) illumination.

The detection system detailed earlier in chapter three was used to detect the reflected flux, (the input to the detector was filtered to 589 nm for white light illumination). The monodisperse spherical latex particles suspended in de-ionized water, at a

volume fraction of 0.0238, provided the scattering samples.

(6.3) Results.

Figures (6.3.1) and (6.3.2) illustrate typical results obtained for laser illumination and diffuse white light illumination. The solid line represents the fitted curve, i.e. equation (6.2.1).

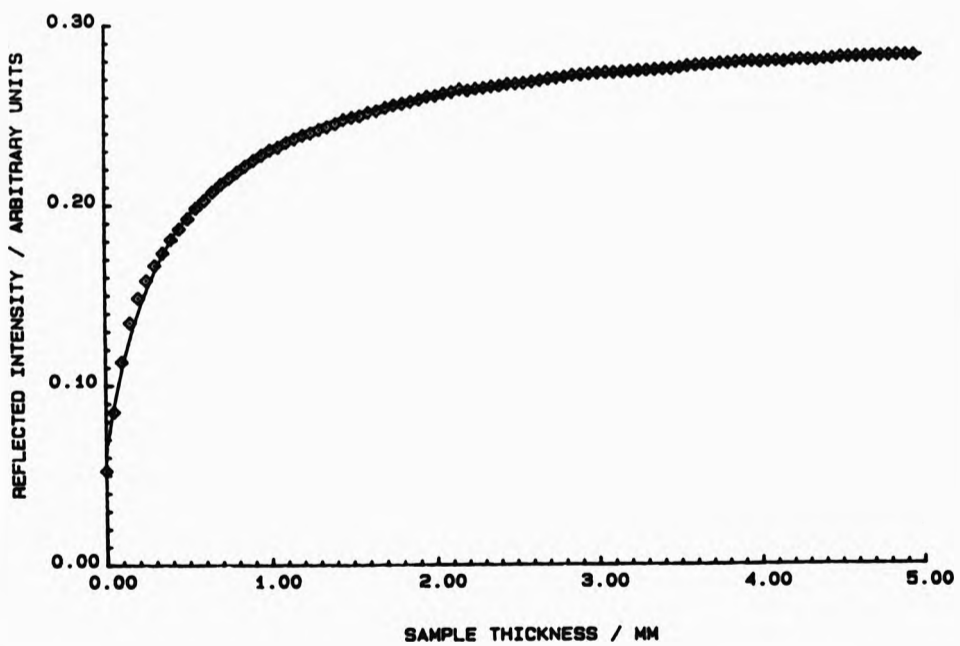


Fig (6.3.1)
Reflected intensity as a function of sample thickness.
Laser illumination. Wavelength = 633 nm, mean particle
diameter = 0.33 microns. Solid line shows fitted curve,
i.e. equation (6.2.1).

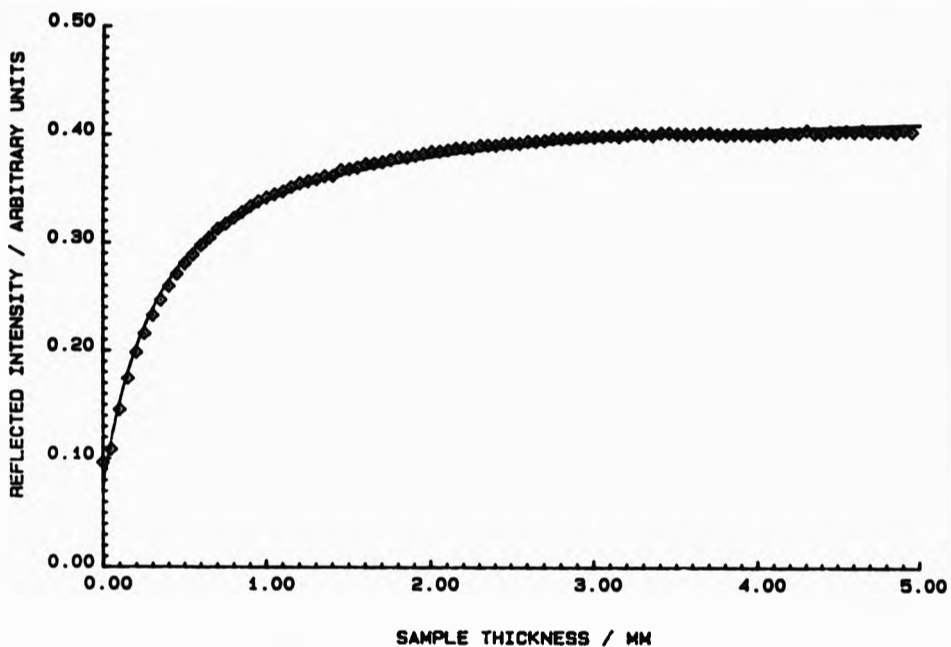


Fig (6.3.2)

Reflected intensity as a function of sample thickness. Diffuse white light illumination. Reflected intensity filtered to 589 nm. Mean particle diameter = 0.33 microns. Solid line shows fitted curve, i.e. equation (6.2.1)

A comparison of figures (6.3.1) and (6.3.2) with the data obtained using optical fibres, i.e. figures (3.3.1), (3.3.6), (3.3.7) and (5.1.3), show that a much better quality of fit is obtained using the integrating sphere.

Tables (6.3.1), (6.3.2) and (6.3.3) compare the theoretical and experimentally obtained values of S . The experimental values have been corrected for internal interfacial reflections at the sample-glass, glass-air interfaces, (assuming a sample refractive index of 1.33), see section (3.7.4). The quoted experimental value of S is the mean value obtained from four experiments on the same

sample. The quoted error is the standard error of the four results.

Particle Diameter /microns	S(exp) / mm ⁻¹	S(Mie) / mm ⁻¹	S(Exp)/S(Mie)
0.085	.75 +/- .03	1.26	.60 +/- .02
0.11	.93 +/- .05	2.24	.42 +/- .02
0.25	8.7 +/- .5	7.82	1.11 +/- .06
0.33	7.8 +/- .3	7.38	1.06 +/- .04
0.48	8.3 +/- .5	7.81	1.06 +/- .06
0.54	8.3 +/- .5	7.59	1.09 +/- .07
1.05	7.3 +/- .5	5.89	1.24 +/- .08
1.43	6.0 +/- .3	4.98	1.20 +/- .06

Table (6.3.1)
S obtained for collimated (laser) illumination. Wavelength = 633 nm.

Particle Diameter /microns	S(exp) / mm ⁻¹	S(Mie) / mm ⁻¹	S(Exp)/S(Mie)
0.085	.88 +/- .08	1.24	.71 +/- .06
0.11	1.03 +/- .05	2.87	.36 +/- .02
0.25	7.5 +/- .1	8.19	.92 +/- .01
0.33	8.0 +/- .8	8.38	.95 +/- .09
0.48	8.3 +/- .5	8.14	1.02 +/- .06
0.54	9.0 +/- .3	8.08	1.11 +/- .04
1.05	7.7 +/- .1	5.95	1.29 +/- .02
1.43	6.5 +/- .3	5.05	1.29 +/- .06

Table (6.3.2)
S obtained for collimated illumination. Wavelength = 589 nm.

Particle Diameter /microns	S(exp) / mm ⁻¹	S(Mie) / mm ⁻¹	S(Exp)/S(Mie)
0.085	.98 +/- .03	1.24	.79 +/- .02
0.22	8.7 +/- .5	8.19	1.06 +/- .06
0.33	8.2 +/- .1	8.38	.98 +/- .01
0.48	8.7 +/- .3	8.14	1.07 +/- .04
0.54	8.5 +/- .8	8.08	1.05 +/- .09
1.05	7.00 +/- .05	5.95	1.18 +/- .01
1.43	6.3 +/- .1	5.05	1.25 +/- .02

Table (6.3.3)
S obtained for diffuse illumination. Wavelength = 589 nm.

It is clear from the results that it makes little difference

to the measured value of S whether the sample is illuminated directly or indirectly. This is however to be expected, when the sample is illuminated with collimated flux the flux reflected from the sample will illuminate the internal surface of the integrating sphere. The integrating sphere will diffusely reflect this flux to re-illuminate the sample. Hence, when the sample is illuminated with collimated flux, it is also illuminated with diffuse flux due to the reflectance of the sample.

The agreement between the theoretical and experimental values of S is unaltered by using laser illumination, as we would expect if the measured value of S is independent of the coherence length of the illuminating radiation.

(6.4) Conclusion.

It has been shown that the agreement between the theoretical and experimental values of S is good so long as the internal interfacial reflections are taken into account. It is therefore reasonable to conclude that the equation $S=3/4NC_{\text{ext}}(1-\overline{\cos\theta})$ is, to at least a good approximation, valid over the tested particle size range for samples of negligible absorption.

The much improved fit to the Kubelka-Munk expression obtained using the integrating sphere is presumably due to the integrating sphere more closely matching the assumptions of the theory, i.e. the sample is diffusely illuminated, and the influx and efflux routes are not physically separate.

CHAPTER 7: ABSORPTION MEASUREMENTS.

(7.1) Introduction.

In the previous experiments it had been assumed that the absorption coefficient K of the scattering sample was negligible in comparison to the scattering parameter S . No attempt was made to measure K , other than to confirm that $K \ll S$. The aim of the following experiments was to determine whether measurements of K may be made using the optical fibre method.

(7.2) Initial Experiments.

Measurements of the scattering parameter S , and the absorption coefficient K , were made using a single optical fibre bundle, (of diameter 6.38 +/- .08 mm and NA 0.50), and beam splitter arrangement, as outlined in chapter five. As in the previous optical fibre bundle experiments, the reflected intensity as a function of illuminated sample thickness was measured. The results were fitted to the Kubelka-Munk equation for a scattering and absorbing sample,

$$R = \frac{1-r(a-b\coth(bSd))}{a-r+b\coth(bSd)} \quad \dots(7.2.1)$$

where $a = \sqrt{1+K/S}$, $b = (a-1)^2$

r = diffuse reflectance of the base of the cell.

The quantity r was left as a fitting parameter. Two experimental studies are described below where in one r is approximately zero (black backing), and in the other r is

approximately one (white backing).

The samples were prepared from a suspension of $0.180 \pm .007$ micron spheres in de-ionized water, with a volume fraction of 0.041. The absorption of the sample was varied by the addition of a dye solution. The dye solution was made from Malachite Green dissolved in distilled water. A solution of 7.5×10^{-3} % by weight of dye was used to provide absorption within the samples. The detected radiation was filtered to a wavelength of 589 nm.

Initial experiments were carried out on 10 ml of the scattering sample to which was added 0.11 ml of the 7.5×10^{-3} % dye solution. The results quoted below give the mean and standard error from four experiments on the sample. Typical (fitted) experimental results are illustrated in fig (7.2.1).

$$S = 5.6 \text{ mm}^{-1} \pm 2 \%$$

$$K = 6 \text{ m}^{-1} \pm 50 \%$$

It is clear that the error in K is significantly greater than the error in S. The large error in K is due to an inability of the fitting programme to obtain an accurate measurement of the absorption of the sample from the reflected intensity measurements. A measurement of the absorption of the sample is more easily obtained if the reduction in reflected intensity as a function of sample thickness above a reflecting (white) boundary is measured as; (a) the reflected intensity is then highly dependent upon the absorption of the sample and (b) the fitting programme can obtain an accurate measurement of the reflectance of the sample from the reflected intensity data.

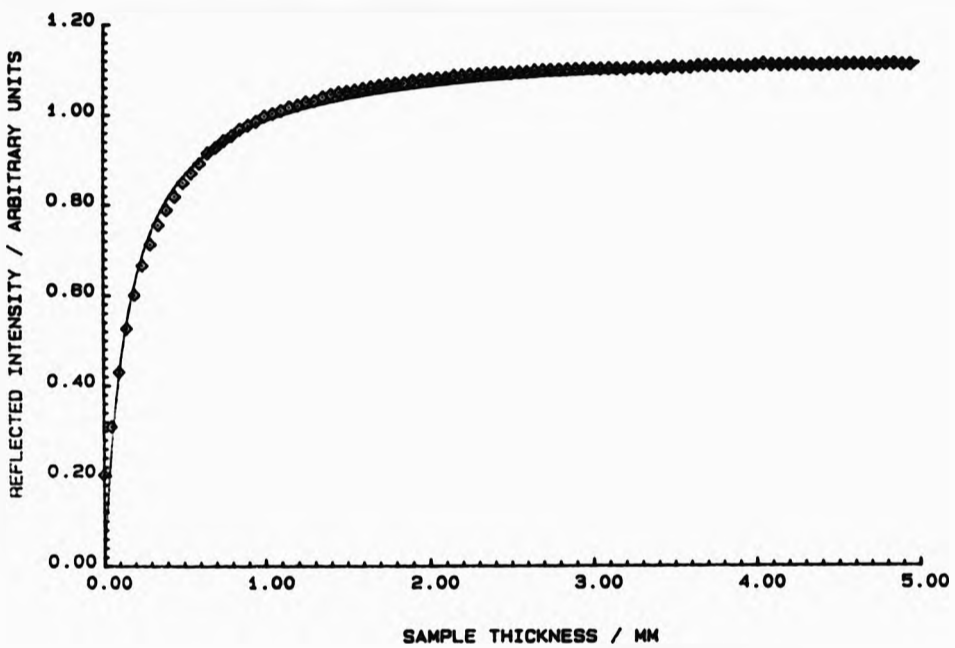


Fig (7.2.1)
 Reflected intensity as a function of sample thickness for an absorbing sample with a matt black cell base. Solid line represents fitted equation (7.2.1). Wavelength = 589 nm, Latex volume fraction = 0.041, mean diameter = 0.18 μm , 0.11 ml of dye solution added.

The matt black cell base was replaced with a matt white cell base, the intensity reflected at zero sample thickness was then commensurate with a reflectance of 1. This provides a reference point by which all intensity measurements may be converted to reflectance measurements. The reflectance of the sample at infinite sample thickness is solely dependent upon the ratio of S to K , hence a measurement of the reflectance of the sample at large sample thickness allows the absorption coefficient K to be accurately estimated by the fitting programme.

Experiments were conducted on a second scattering and absorbing sample made from 15 ml of the scattering sample and 0.4 ml of the dye solution. The experimental results were fitted to equation (7.2.1) with a cell base reflectance of 1. The results given below quote the mean and standard error from four experiments on the sample. Typical experimental results are illustrated in fig (7.2.2).

$$S = 5 \text{ mm}^{-1} \pm 20 \%$$

$$K = 0.15 \text{ mm}^{-1} \pm 7 \%$$

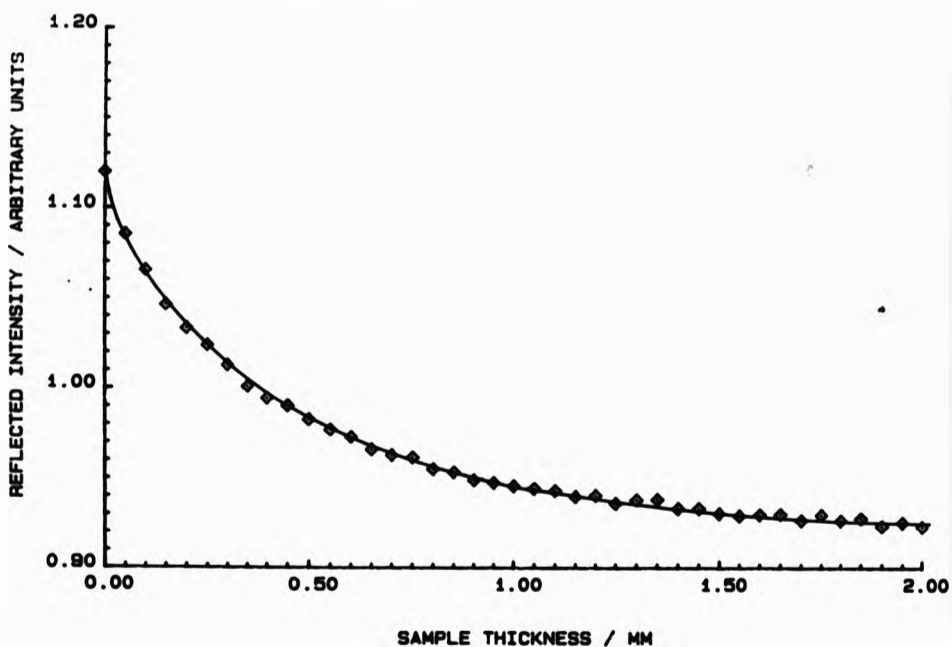



Fig (7.2.2)
 Reflected intensity as a function of sample thickness for an absorbing sample with a matt white cell base. Solid line represents fitted equation (7.2.1). Wavelength = 589 nm, Latex volume fraction = 0.041, mean diameter = 0.18 μm , 0.4 ml of dye solution added.



It is clear that the error in K has been greatly reduced, and the error in S increased. The experimental value of K has been increased by several orders of magnitude over the value obtained using a black based cell. It should be noted here that the difference between the values of K obtained using the two experimental systems, (one with a white based cell, the other with a black based cell), arises from the fitting routine. A low value of K being obtained when the black based cell is used as the fitting routine is incapable of determining the reflectance of the sample from the intensity data. Using a white based cell allows the fitting routine to determine the reflectance of the sample, hence K may be more accurately determined from the fit.

(7.3) Absorption measurements on scattering samples.

Experiments were carried out on the scattering sample with varying amounts of dye solution added. The fitting results are illustrated in fig (7.3.1). Note the dye concentration is expressed in terms of the percentage by weight of dye solution added to the scattering sample.

It can be seen from fig (7.3.1) that to a good approximation there is a linear relationship between the dye concentration and the fitted value of K. The finite value of the intercept implies that the pure scattering sample used has a finite absorbance of $.09 \pm .01 \text{ mm}^{-1}$. Measurements on the scattering

sample with no dye added, using this experimental system, yielded a value of K of $.08 \pm .01 \text{ mm}^{-1}$. This is in good agreement with the extrapolated result. The gradient of the K vs dye concentration curve is $.023 \pm .002 \text{ mm}^{-1} \%$.

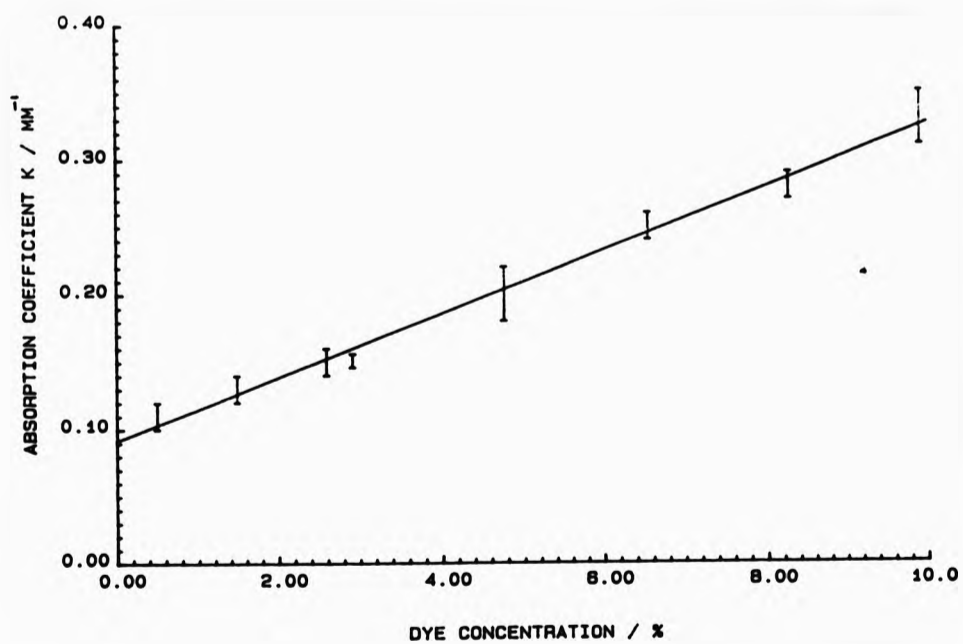


Fig (7.3.1)
Absorption coefficient K , as a function of dye concentration added to the scattering sample.

The value of K obtained for zero dye concentration is somewhat large. Observations of the sample with the naked eye showed that the sample appeared to have a green tint for even low dye concentrations, no such visible observations of absorption were noted in the pure scattering sample. It therefore appears likely that the absorption measured in the purely scattering sample is an artifact of the experimental system. This effect may be explained by considering the numerical aperture of the optical fibre bundle. Consider an optical fibre bundle immersed in a non-absorbing scattering sample, parallel to a perfectly white, flat boundary. For low path lengths, i.e. $Sd \ll 1$, the majority of the light emergent from the fibre will be directly reflected by the white base back to the fibre bundle, see fig (7.3.2a). As the path length increases the divergence of the emergent beam will cause less of the light reflected from the white base to be detected by the optical fibre bundle, (so long as $Sd < 1$), see fig (7.3.2b). Hence a decrease in the detected optical power will be observed. If these results, obtained for a non-absorbing sample, were fitted to equation (7.2.1), a finite absorption coefficient would be returned by the fitting routine, due to the apparent decrease in sample reflectance with sample thickness. Such a process would account for the relatively large absorption recorded for the pure scattering samples.

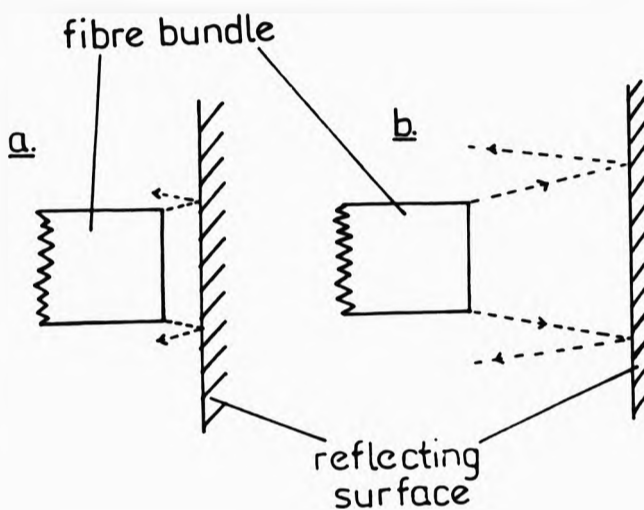


Fig (7.3.2)
Decrease in detected reflected intensity due to numerical aperture of optical fibre bundle.

(7.4) Absorption measurements on non-scattering samples.

For the purpose of comparison further experiments were conducted to measure the absorption of the dye solution as a function of dye concentration for a non-scattering sample.

A cylindrical glass cell with a glass base was illuminated from below by collimated white light. The cell was filled with a dye solution and a single optical fibre bundle placed within the sample. The fibre bundle was then moved upwards through the sample, and the intensity transmitted through the fibre bundle measured as a function of illuminated sample thickness.

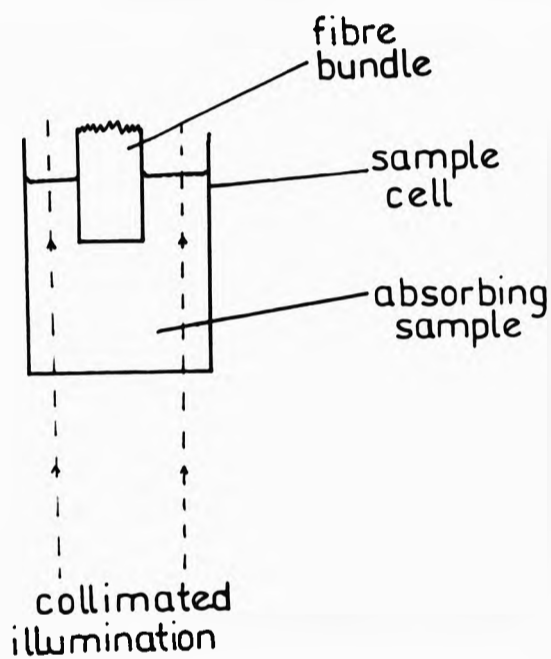


Fig (7.4.1)
Absorption measurement experimental system.

The same illumination, detection and mechanical movement systems as detailed in chapter three were used. The transmitted light was filtered to 589 nm. The data was fitted to Lambert's law (49),

$$I = I_0 \exp(-NC_{abs}d).$$

The results are illustrated in fig (7.4.2).

Where N & C_{abs} now refer to the dye

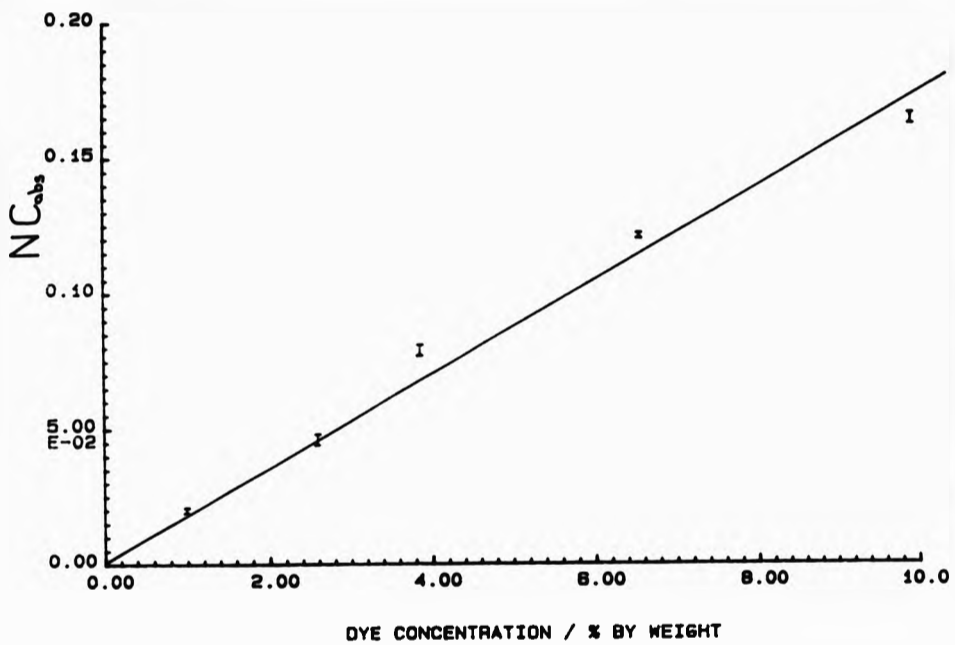


Fig (7.4.2)
Fitted value of NC_{obs} as a function of dye concentration, C_n .

It can be seen that to a good approximation there is a linear relationship between NC_{obs} and the dye concentration. The gradient of the fitted straight line is $0.0179 \pm 0.0005 \text{ mm}^{-1} \%$, and the intercept is $0.002 \pm 0.003 \text{ mm}^{-1}$. It has been shown that, (section 2.3),

$$K = 2NC_{obs}$$

Hence, the ratio of the gradient of K vs C_n to the gradient of NC_{obs} vs C_n should be equal to 2.

$$\text{Ratio} = \frac{0.023 \pm 0.002}{0.0179 \pm 0.0005}$$

Hence,
$$K_e = 1.3 \pm 0.1$$
 where K_e = the experimentally determined value of K.

But,
$$K_t = 2NC_{obs}$$
 where K_t = the theoretical value of K.

Hence,
$$K_e/K_t = \frac{(1.3 \pm 0.1)NC_{obs}}{2NC_{obs}} = 0.65 \pm 0.05$$

Measurements of S using this fibre bundle returned values of S that were $62 \pm 4\%$ of their theoretical value, i.e.,


$$S(\text{exp})/S(\text{the}) = 0.62 \pm 0.04$$

Therefore it would appear that the experimental values of S and K are related by the same factor to the theoretical values of S and K.

Note: The comparatively low ratio of $S(\text{exp})/S(\text{the})$ was unexpected. A ratio of 0.85 was obtained using a similar system with a fibre bundle of radius 6.72 mm. The $S(\text{exp})/S(\text{the})$ ratio was checked using several monodisperse latex samples with no significant change being observed. Examination of the fibre bundle under a microscope revealed that large areas of the fibres were broken. This would result in an increase in the effective separation between the influx and efflux routes to and from the sample, hence the low $S(\text{exp})/S(\text{the})$ value obtained with this fibre bundle.

(7.5) Conclusion.

It has been shown that accurate measurements of the changes in



the absorption coefficient K may be made using the single optical fibre bundle method (detailed in chapter 5) if a reflecting (white) boundary is placed behind the sample. It has been shown that the ratio of the experimental to theoretical value of K is the same as the experimental to theoretical ratio for S .

CHAPTER 8: CONCENTRATION EFFECTS.

(8.1) Introduction.

It has been shown that to a good approximation,

$$S = 3/4NC_{9A}(1-\cos\theta),$$

for volume fractions, v less than 0.025. It is well-known [11,50,51] that for high volume fractions, S is a non-linear function of v . The purpose of this investigation is to examine this effect, comparing the results from monodisperse spherical particulate systems with results from non-spherical particulate systems.

Two latex samples were used in this investigation;

(i) A suspension of 0.180 +/- .007 micron diameter spheres, with a volume fraction of 0.270.

(ii) A suspension of 0.21 +/- .09 micron diameter spheres, with a volume fraction of 0.378.

The concentration of these samples was varied by the addition of distilled water, and checked by weighing and drying the samples.

Experiments were also carried out on broad size fraction samples of kaolin clay particles, (English China Clay grade SPS), suspended in distilled water. The samples were prepared as detailed in section 1.3 for maximum particle deflocculation, i.e. the pH of the sample was adjusted to 8.5 and 0.21 % by dry

weight of clay of sodium polyacrylate was added. All samples were agitated immediately before each experiment to eliminate any sedimentation. As with the latex spheres, the concentration of the kaolinite samples was monitored by drying and weighing.

(8.2) Experimental procedure.

A single optical fibre bundle, (of diameter 6.38 +/- .08mm and NA 0.50), was used in conjunction with a beam splitter to measure the scattering parameter of the samples as a function of concentration, (using the method detailed in chapter 5). The same illumination, detection and mechanical movement systems were used as described previously in chapter three. The detected light was filtered to 589 nm. The reflected intensity as a function of illuminated sample thickness was measured and the results were fitted to equation (3.2.2), i.e

$$I = \frac{A.Sd}{(1+Sd)}$$

(8.3) Results.

The scattering parameter of the three samples as a function of volume fraction are given in tables (8.3.1), (8.3.2) and (8.3.3). The quoted experimental value of S for any given concentration is the mean value obtained from four experiments on the same sample. The quoted error is the standard error of the four results.

Volume Fraction.	S / mm ⁻¹
0.270	23 +/- 2
0.238	24 +/- 1
0.190	26.2 +/- .5
0.172	27.7 +/- .3
0.139	27 +/- 2
0.101	22 +/- 1
0.078	20 +/- 1
0.026	11.2 +/- .5

Table (8.3.1)
0.180 +/- .007 micron spheres.

Volume Fraction	S / mm ⁻¹
0.378	11.4 +/- .8
0.341	12.7 +/- .3
0.309	12 +/- 2
0.276	13.7 +/- .8
0.249	14 +/- 1
0.215	15 +/- 2
0.182	15 +/- 1
0.123	13.5 +/- .8
0.057	11.0 +/- .8
0.036	7.3 +/- .8
0.0084	2.8 +/- .5

Table (8.3.2)
0.21 +/- .09 micron spheres.

Volume Fraction	S / mm ⁻¹
0.366	67 +/- 3
0.328	61 +/- 3
0.213	48 +/- 3
0.141	34 +/- 1
0.111	22 +/- 1
0.075	18 +/- 1
0.042	8.9 +/- .5
0.015	3.8 +/- .3

Table (8.3.3)
Kaolin samples: SPS.

These results are illustrated in fig (8.3.1), fig (8.3.2) and

fig (8.3.3).

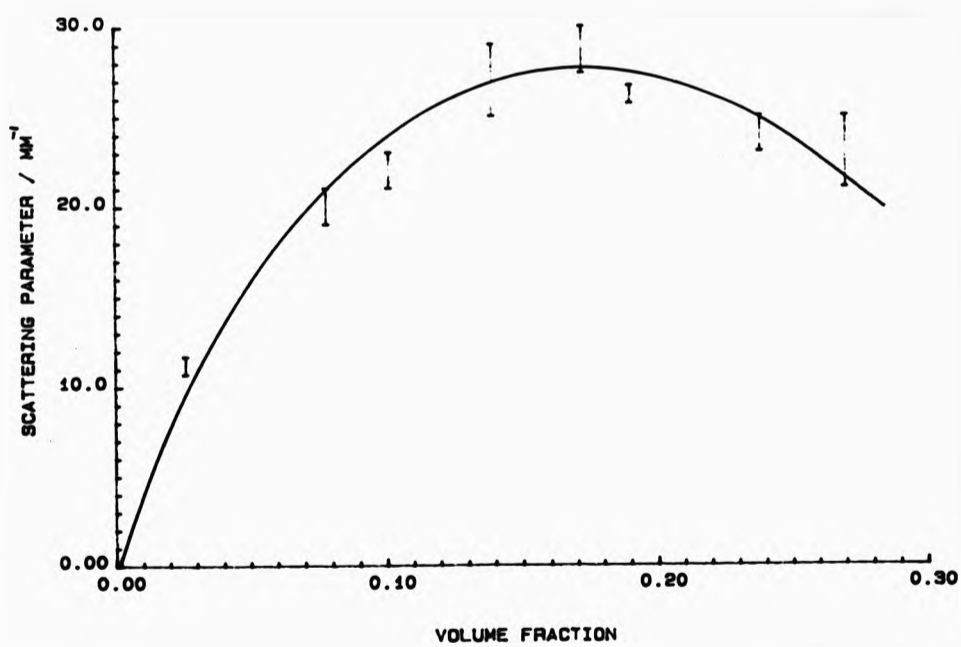


Fig (8.3.1)
Measured scattering parameter as a function of sample concentration. Latex sample, mean particle diameter = $0.18 \mu\text{m}$, wavelength = 589 nm .

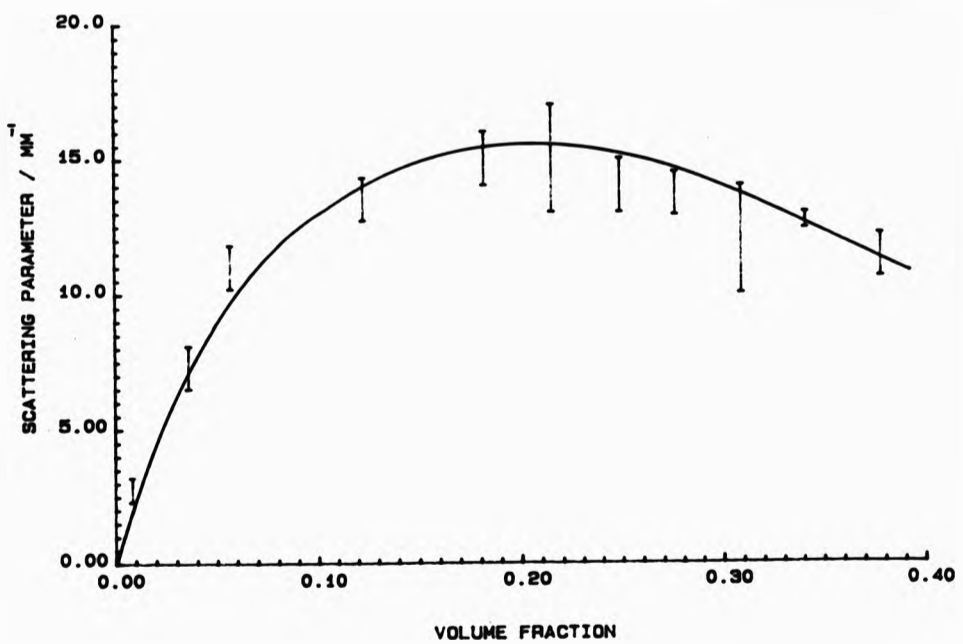


Fig (8.3.2)
 Measured scattering parameter as a function of sample concentration. Latex sample, mean particle diameter = 0.21 μm , wavelength = 589 nm.

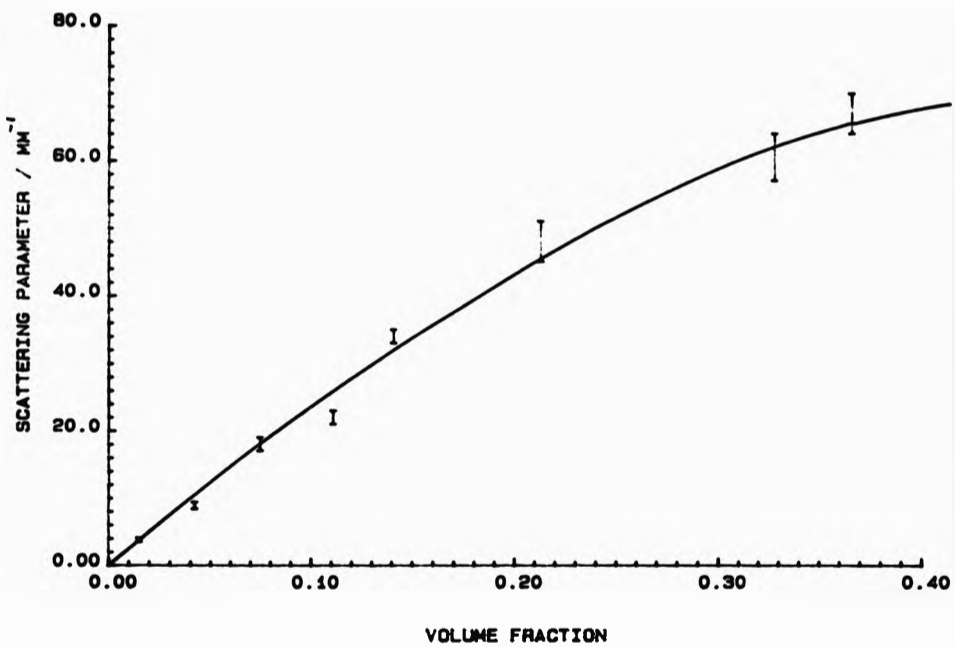


Fig (8.3.3)
 Measured scattering parameter as a function of sample concentration. Kaolin sample, English China Clay grade SPS. Broad size fraction, 80 % < 2 μ m. Wavelength = 589 nm.

It can be seen from figs (8.3.1) and (8.3.2) that the latex samples peak in scattering parameter at a volume fraction of approximately 0.20. This is in reasonable agreement with the results of Meeten et al. [11], obtained with monodisperse spherical

latex particles. The drop in the effective scattering cross section per particle with concentration has been widely reported elsewhere [50,51,52]. The clay particles do not show such a peak in scattering parameter, although a decrease in scattering efficiency per particle is evident.

(8.4) Analysis of results.

The expression used to calculate the scattering parameter S of a monodisperse system is,

$$S = 3/4NC_{sc} (1 - \overline{\cos \Theta}).$$

This predicts a linear relationship between S , and the number concentration (per unit volume), N . To a good approximation this expression has been shown to be valid by previous experiments, for volume fractions less than 0.025. The non-linear relationship between N and S at higher volume fractions therefore implies that the above equation ^{may be} inapplicable to samples of high volume fraction as, the quantities C_{sc} and $(1 - \overline{\cos \Theta})$ ^{may be} affected by the particle number density. Gate [52], proposed that the values C_{sc} and $(1 - \overline{\cos \Theta})$ were modified due to the scattering particles affecting the effective refractive index of the continuous phase of the scattering medium. Hence, the increasing concentration of scattering particles reduces the refractive index mis-match between the scattering particle and the continuous medium, thus (generally), reducing the value of Q_{sc} . Gate assumed a linear relationship between the particle concentration and the bulk refractive index n of the scattering sample. Using the data of Hiltner and Krieger [53] the following empirical relationship

between the bulk refractive index n' , and the volume fraction v , of the latex is obtained [40],

$$n' = 0.27v + 1.333.$$

This expression is in good agreement with that of Meeten et al. [11],

$$n' = m_1 + \chi(m_2 - m_1)v,$$

where; m_1 = the refractive index of the continuous phase, (i.e. in this case that of water, 1.333),

m_2 = the refractive index of the scattering particles, (i.e. in this case that of latex, 1.60),

χ = a constant with a value between 0.94 and 1.05.

We may therefore determine the bulk refractive index of the sample from the above equations for a given volume fraction of latex. Using the new refractive index a new relative refractive index, m' , ($m' = m/n'$), and size parameter x' , ($x' = 2\pi an'/\lambda$), may be calculated. Using these values of m' and x' the concentration dependent values of Q_{sc} and $(1 - \overline{\cos\theta})$, (and hence S), may be calculated from Mie theory. The tables below illustrate the values of S so calculated.

Vol. frac.	n'	x'	m'	S/mm^{-1}
0.270	1.40	1.35	1.140	47.9
0.238	1.39	1.34	1.148	46.7
0.190	1.38	1.33	1.159	42.3
0.172	1.38	1.32	1.163	40.0
0.139	1.37	1.31	1.170	34.8
0.101	1.36	1.30	1.179	27.6
0.078	1.35	1.30	1.184	22.3
0.026	1.34	1.28	1.197	8.4

Table (8.4.1)
0.180 +/- .007 micron sample.

Vol. frac.	n'	x'	m'	S/mm ⁻¹
0.378	1.43	1.60	1.118	52.1
0.341	1.42	1.59	1.127	54.1
0.301	1.41	1.58	1.135	53.6
0.276	1.40	1.57	1.143	54.7
0.249	1.40	1.57	1.143	49.3
0.215	1.39	1.56	1.151	47.1
0.182	1.38	1.55	1.159	43.9
0.123	1.36	1.52	1.176	35.5
0.057	1.35	1.51	1.185	18.0
0.036	1.34	1.50	1.194	12.4
0.0084	1.33	1.49	1.200	3.05

Table (8.4.2)
0.21 +/- .09 micron sample.

The process is not quite so straightforward for the kaolin sample as there is a large distribution of particle sizes, (see section 1.3). However, we can make an estimate of the effective mean particle size from the scattering parameter of the sample at low volume fractions. Taking the result for the most dilute sample, i.e. $v = 0.015$, $S = (3.8 \pm .3) \text{ mm}^{-1}$. Figure (8.3.4) illustrates the scattering parameter as a function of particle diameter for a sample of refractive index 1.57 and volume fraction .015. It can be seen from the graph that a monodisperse sample at this volume fraction with a scattering parameter of $(3.8 \pm .3) \text{ mm}^{-1}$ corresponds to a mean particle size of $(.18 \pm .02)$ microns, or $(0.65 \pm .2)$ microns. The size distribution data presented in fig (1.3.1), would suggest that the larger diameter is the more appropriate. Having determined an approximate effective mean diameter the effect of particle concentration on the observed value of S can be calculated from Gate's theory.

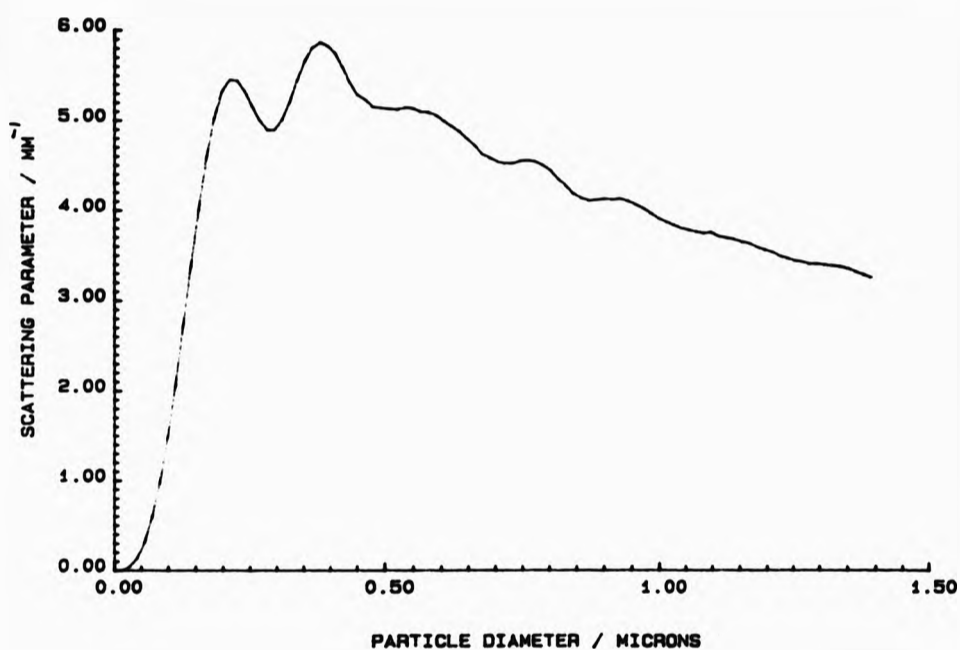


Fig (8.4.1)
 Calculated scattering parameter as a function
 of particle size. Wavelength = 589 nm, relative
 refractive index, $m = 1.19$.

Vol. frac.	n'	x'	m'	S/mm^{-1}
0.366	1.42	5.68	1.106	29.9
0.328	1.41	5.64	1.113	30.5
0.213	1.38	5.53	1.135	28.5
0.141	1.37	5.46	1.149	23.0
0.111	1.36	5.44	1.155	19.7
0.075	1.35	5.40	1.162	14.5
0.042	1.34	5.37	1.169	8.86
0.015	1.34	5.35	1.174	3.36

Table (8.4.3)
Kaolin clay sample:SPS grade.

The calculated and experimental values of S as a function of volume fraction are illustrated in fig (8.4.2), fig (8.4.3) and fig (8.4.4).

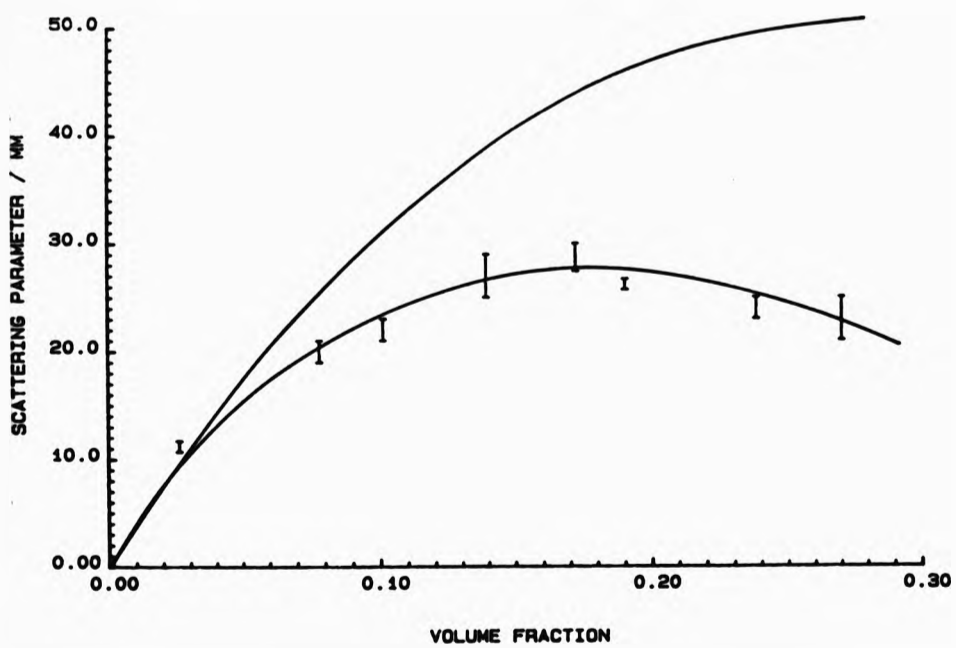


Fig (8.4.2)
 Comparison of theoretical (upper curve) and experimental
 (lower curve) values of S. 0.18 micron latex sample.
 Wavelength = 589 nm.

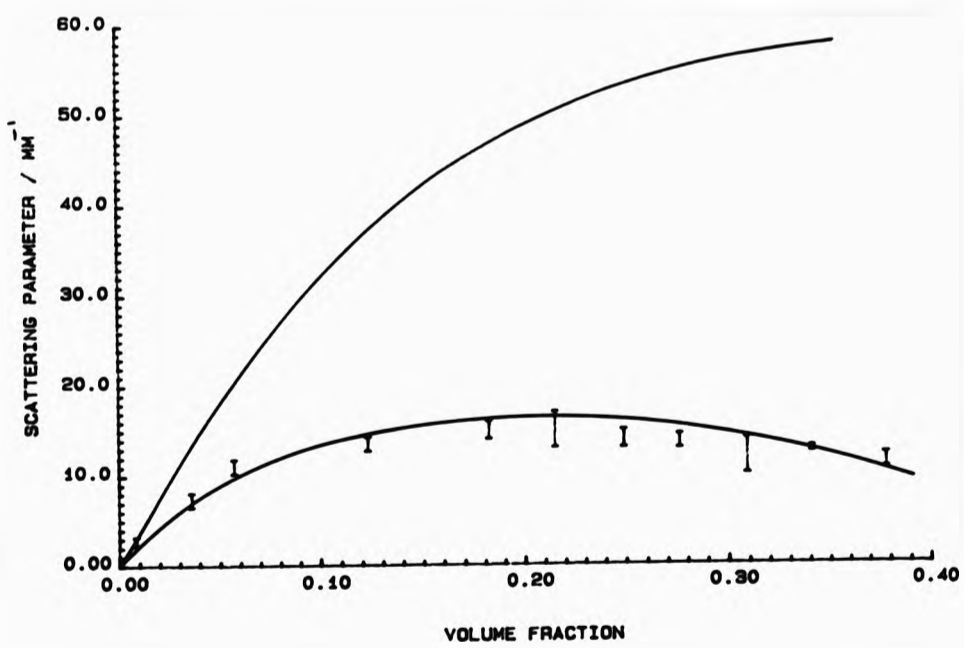


Fig (8.4.3)
 Comparison of theoretical (upper curve) and experimental
 (lower curve) values of S. 0.21 micron latex sample.
 Wavelength = 589 nm.

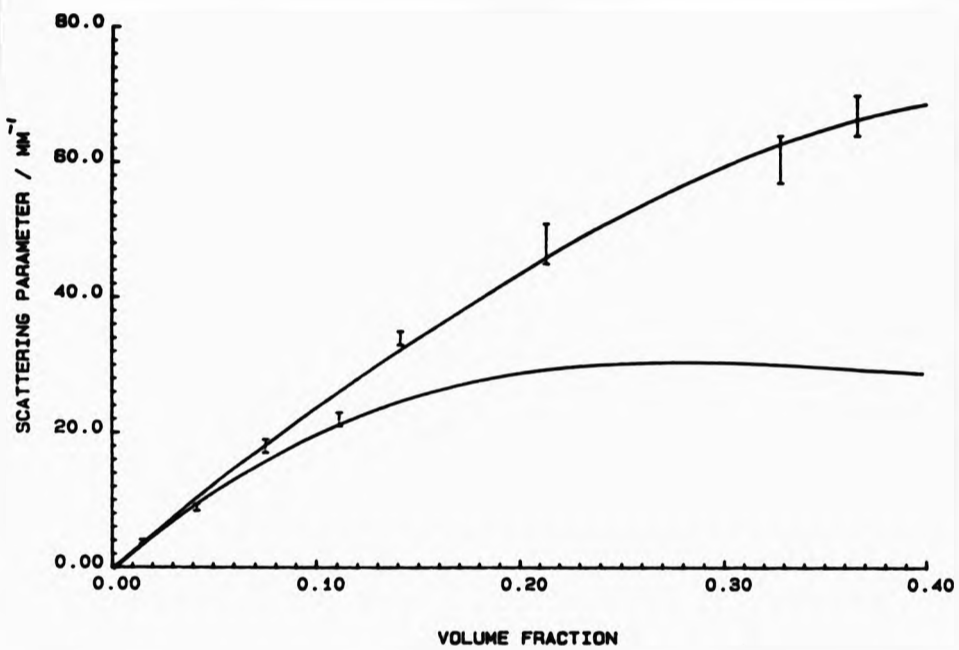


Fig (8.4.4)
 Comparison of theoretical (lower curve) and experimental (upper curve) values of S. Kaolin SPS grade sample.
 Wavelength = 589 nm.

It is clear from a comparison of the theoretical and experimental graphs that Gate's theory overestimates the decrease in scattering efficiency for the clay sample, and underestimates it for the latex samples. In addition there is very poor agreement between the experimental and theoretical values of S.

(8.5) Discussion.

There has so far been limited success in finding an accurate theoretical model to describe multiple scattering in highly

concentrated systems. The model proposed by Gate [52] would appear to be a useful first approximation in that it does predict the broad trends observed experimentally, i.e. a drop in scattering efficiency per particle with concentration. Meeten and Killey [11] proposed a more complex model, this explains the drop in scattering efficiency per particle by assuming there is some type of concentration-dependent liquid-like ordering of particles. By applying Mie theory results computed for concentric spheres, scattering efficiencies can be calculated. Meeten and Killey report good agreement with experimental data. However the choice of radius for the liquid-like ordering is (presently) somewhat arbitrary, this leads to limitations in the applicability of such a theory to practical situations.

The results obtained may be explained by assuming that there is a reduction in scattering efficiency due to close packing of the particles. The spherical particles exhibit a much larger reduction in scattering efficiency per particle with increasing volume fraction. This is commensurate with such a system as the monodisperse spherical particle samples will be capable of more ordered packing than the polydisperse non-spherical kaolinite particle samples, thus resulting in a larger drop in scattering efficiency in the spherical particle samples. This is consistent with the results presented by Fitzwater and Hook [54] for measurements of the scattering parameter S as a function of volume fraction of rutile titanium dioxide, TiO_2 , (see fig (8.5.1) reproduced from Fitzwater and Hook). Rutile TiO_2 particles are approximately spherical, and hence packing of such particles would

be somewhere between the two extremes of the monodisperse spherical latex particles, and the highly polydisperse plate-like kaolin particles. Fig (8.5.1) shows that the drop in scattering efficiency per particle for TiO_2 is less than that obtained for the latex samples, and higher than that obtained for the kaolinite samples.

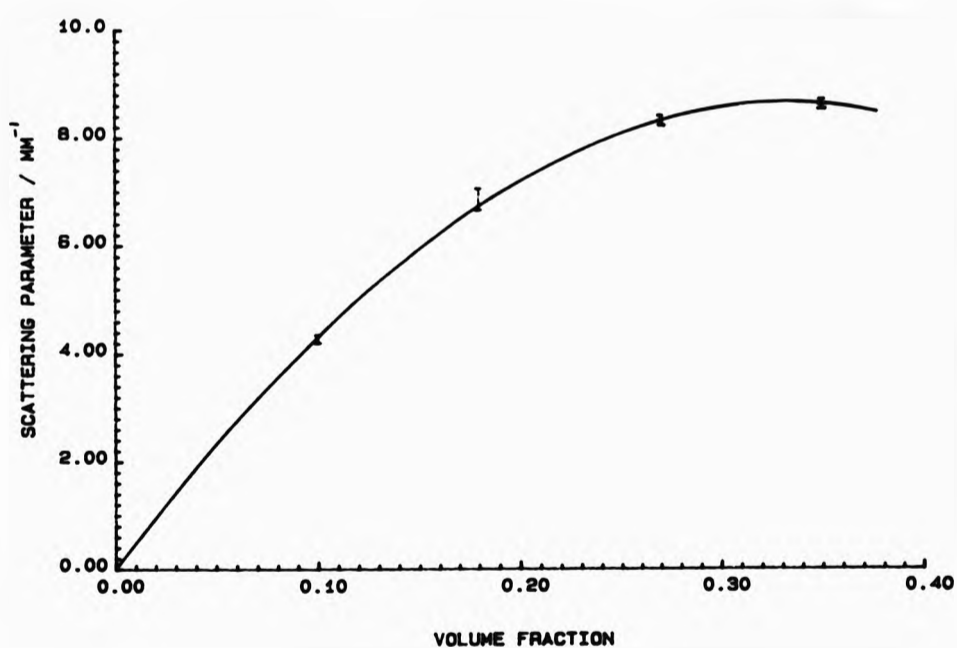


Fig (8.5.1)
Kubelka-Munk scattering coefficient S as a function of volume fraction of titanium dioxide. Figure reproduced from Fitzwater and Hook [54].

(8.6) Conclusion.

The drop in scattering efficiency per particle observed in

highly concentrated scattering systems can be explained in terms of close packing of particles. It has been shown from the experimental results that the more ordered the particle system, (and hence the more ordered the packing at high concentrations), the higher the drop in scattering efficiency with particle concentration.

CHAPTER 9: FLOW EFFECTS IN CONCENTRATED COLLOIDAL SYSTEMS.

(9.1) Introduction.

Non-spherical particles will be partially orientated by laminar flow [2]. Flow-orientation is due exclusively to the anisometry of the particle and any torque produced by the velocity gradient.

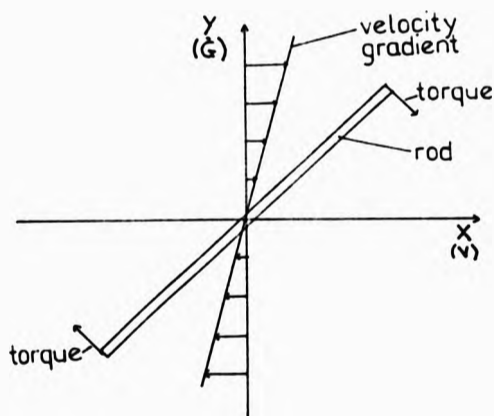


Fig (9.1.1)
Torque exerted on a rigid rod by velocity gradient.

Fig (9.1.1) illustrates the two dimensional case of a rigid rod in a shear field, the same argument may be extended to the plate-like kaolinite particle.

Fig (9.1.1) also illustrates the velocity vector v which is parallel to the X-axis, and the velocity gradient \dot{G} parallel to the Y-axis. A third vector n is defined as being mutually orthogonal to the velocity vector and the velocity

gradient, and hence is parallel to the Z-axis, into the plane of the paper. The shear plane is defined as the plane that contains v and \dot{G} , i.e. the (v, \dot{G}) plane.

The torque exerted on the particle is dependent upon the particle orientation, hence as the particle rotates due to the effect of the torque exerted on it, so the torque acting upon it alters. Hence a particle will rotate with a (generally) non-uniform angular velocity. Neglecting inertial forces, the angular velocity of the particle will be a minimum when the torque exerted on the particle is a minimum. It can be seen from figure (9.1.1) that a minimum torque will be experienced by the particle when its longest axis is parallel to the direction of the stream lines. Therefore in any one rotation the particle will spend most of its time with its longest axis in the direction of the stream lines.

Opposing the alignment effect of the velocity gradient is the randomizing influence of Brownian motion. Brownian motion will cause random variations in the motion and orientation of the particles. This will result in a distribution of orientations for any group of particles. The probability of a spheroid having a given orientation is governed by the rotary convective-diffusion equation [55,56],

$$\frac{\partial p}{\partial t} = D_r \nabla^2 p - \nabla \cdot (w p) \quad \dots(9.1.1)$$

where p = the probability of a spheroid having a given orientation,
 D_r = the rotary-diffusion constant and
 w = the angular velocity of the particle.

No general solution of equation (9.1.1) exists, but numerical and asymptotic solutions are available. The solution obtained is dependent upon the rotary Peclet number, P , defined as

$$P = \frac{G}{D_r}$$

When $P \rightarrow \infty$ rotary diffusion is negligible and the particle rotation and orientation is governed by the applied shear. When $P \rightarrow 0$ Brownian motion is dominant, hence all orientations are equally probable, i.e. the particles are randomly orientated.

For a very thin oblate spheroid, regarded as a disc, in a continuous medium the rotary diffusion coefficient D_r about any diameter is given by the expression (57),

$$D_r = \frac{3kT}{4\eta d^3}$$

where d = the diameter of the spheroid,
 k = Boltzman's constant,
 T = the Kelvin temperature,
 η = the viscosity of the surrounding medium.

For a sample of oblate spheroids with face diameters 1.5 microns at a volume fraction 0.025, the above equation gives $D = 45 \text{ sec}^{-1}$. Hence, strong alignment would be expected for $G \approx 45 \text{ sec}^{-1}$ (i.e. $P \approx 1$). Thus strong alignment is experimentally obtainable.

Aligning the particles within a colloidal dispersion results in optical anisotropy in the dispersion. The optical effects of shear induced orientation of kaolinite have been studied in the single scattering regime [57,58,59]. Information on the size and shape of the suspended particles, and their stability, may be

extracted from such rheo-optical measurements [58,59]. Little work has been conducted on rheo-optical effects in highly concentrated and multiple scattering samples. Single scattering measurements are of limited use in studying the effects of particle interactions, which will be virtually absent at low particle number densities. It has recently been shown however that it is possible to make rheo-optical measurements on concentrated, multiple-scattering samples, to extract information on particle orientation and interactions [9].

(9.1.1) Kaolinite clay samples.

The samples used in this investigation were kaolinite clays suspended in water. Kaolinite clays are ideally suited to rheo-optical investigations due to their shape, a flat thin plate of typical diameter/thickness aspect ratio 10:1 [8], and their low absorption of light in the visible region [9], which maximises the received intensity for reflectance and transmittance measurements. The effect of flocculation on the rheo-optical properties of the sample may also be easily studied, as kaolinite suspensions can be flocculated or deflocculated by manipulating the pH of the sample [9]. Deflocculation may also be achieved by the addition of a surfactant, see section (1.3). The major disadvantage of the kaolinite is that the clay particles have a high relative density; 2.6. This leads to high settling rates within the suspensions, causing drifting of optical intensity readings as the particles settle out of the suspension. The refractive index of kaolinite is 1.56 [9].

(9.1.2) Previous multiple scattering rheo-optical measurements.

Measurements of shear induced optical changes on multiple scattering samples have been made [9] using the fibre geometry shown in fig (9.1.2). The rheo-optical measurements were confined to light directions normal to the shear plane. Shear induced changes in the reflectance of the samples were studied, and no attempt was made to relate these to changes in the scattering parameter of the sample. Fig(9.1.2) illustrates the apparatus used by Molloy [9] to monitor changes in reflectance of kaolinite clay samples with volume fractions between 0.05 and 0.30.

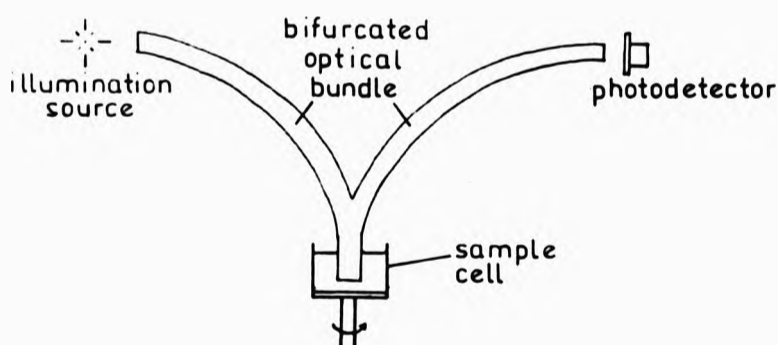


Fig (9.1.2)
The rheo-optical experimental system of Molloy.

A bifurcated optical probe was used by Molloy to both illuminate and to detect the reflected light from the sample, (as in the bifurcated optical fibre experiments, chapter 3). The bifurcated optical fibre was held at a known height above the base of the cell, and the cell rotated at a known frequency, generating

a shear field within the sample between the base of the cell and the end of the probe. The change in the intensity reflected from the sample as a function of the generated shear field was monitored. Typical results obtained by Molloy, for a kaolinite sample of nominal size range 0.6-0.7 microns at a volume fraction of 0.09 is illustrated in fig (9.1.3). It should be noted that G was not uniform over the illuminated volume in this apparatus. The velocity gradient indicated in fig (9.1.3) is averaged over the illuminated volume.

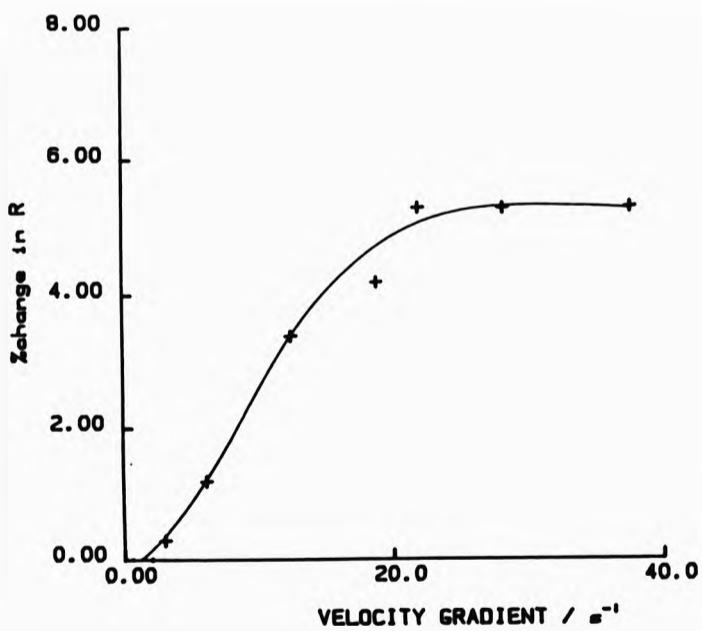


Fig (9.1.3)
Change in reflectance as a function of shear rate. Kaolinite clay sample, nominal size range 0.6-0.7 microns, volume fraction 0.09. Reproduced from Molloy [9].

Reflectance changes as a function of shear rate were measured by Molloy [9] for kaolinite samples of varying particle sizes. It was found that the reflectance of the sample, when viewed at the normal to the shear plane, increased on shearing the sample. Molloy concluded that this was evidence of the particles orientating themselves in the shear field. The particles will orientate themselves so that the normal to their faces will spend most of their time normal to the shear plane [57], see fig (9.1.1). This will result in the geometric area presented to the optical fibre probe face being increased. If we assume the diffraction limit approximation for the scattering cross-section [3], (i.e. the scattering cross-section is twice the geometric cross-section), then the change in the scattering cross-section is simply the change in the geometric cross-section. It can be concluded from this simple analysis that,

- (i) the scattering cross-section will increase under shear when observed parallel to the velocity gradient, and
- (ii) the scattering cross-section will decrease under shear when observed parallel to the velocity vector.

The results of Molloy agree well with these conclusions in the limited respect that an increase in scattering parameter of the sample is recorded under shear for observations of the sample parallel to the velocity gradient.

(9.1.3) Aims of rheo-optical experiments.

The main disadvantages with the rheo-optical measurements on concentrated systems so far carried out, [9] are that; (a) no attempt was made to relate the changes in reflectance to actual changes in the scattering parameter of the sample, and (b) measurements of changes in reflectance with shear rate were only conducted parallel to the velocity gradient.

The magnitude of the change in the observed reflected intensity will be dependent upon the experimental geometry and the scattering parameter of the sample. It is therefore difficult to make meaningful comparisons between samples. In addition, it would be instructive to study reflectance changes normal, as well as parallel to, the shear plane. We would expect that if the increase in the reflected intensity observed normal to the shear plane is indeed due to shear orientation of the particles, a corresponding decrease will be observed parallel to the shear plane.

Thus the following objectives were chosen:

- (a) To relate the measured changes in reflectance of the sample to changes in the scattering parameter S .
- (b) To develop a system capable of monitoring changes in reflectance both parallel and normal to the shear plane.
- (c) To maximize these observed changes in reflectance.

In following these aims two sets of experiments were carried out using different flow geometries. The first set were done using a slot-flow cell, where the fluid flowed in a long slot of internal dimensions 3 mm by 30 mm, thus the generated velocity gradient was non-uniform across the cell thickness. The second set of experiments, designed partially to study the G-dependence of S, was based on an inner-rotor concentric cylinder rheometer. For this design G was closely uniform across the volume of fluid probed by the fibres.

(9.2) Slot-flow cell.

A rectangular flow cell of internal dimensions 0.30 cm by 3.0 cm, was constructed out of matt black optically absorbing plastic, see fig (9.2.1).

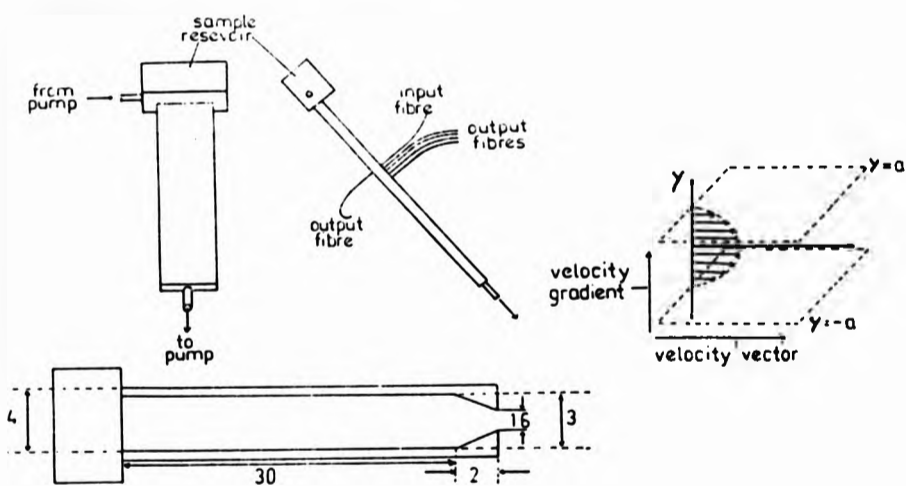


Fig (9.2.1)
Slot-flow cell.

Five fibres were mounted in a straight line along the centre of the top of the cell, approximately half way along the length of the cell. The fibre separations are given in fig (9.2.2). A further fibre was mounted directly opposite the first fibre in the group, on the bottom of the cell. The dimensions are given in fig (9.2.2).

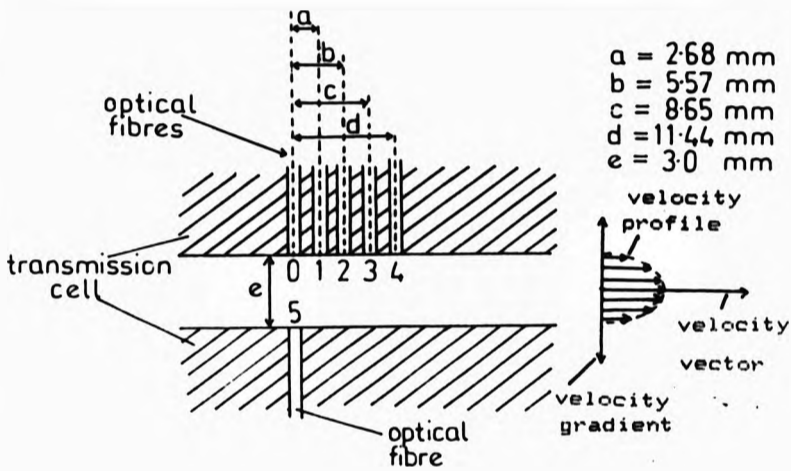


Fig (9.2.2)
Optical fibre mounting geometry.

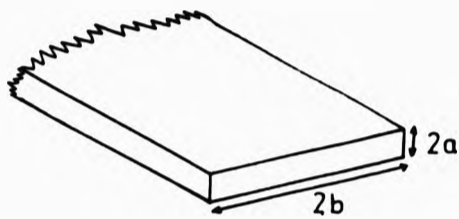
The fibre detection system worked on the principle of transmission of light through the flowing sample. Fibre 0 was used to illuminate the sample. Light transmitted along the sample was detected by fibres 1,2,3 and 4. Light transmitted across the sample was detected by fibre 5. The same illumination and detection systems as detailed earlier were used. The detected intensity was filtered to 589 nm using an interference filter of approximate bandwidth 16 nm.

Care was taken when developing the cell to minimize turbulence and eddy currents. The internal dimensions were held constant from the reservoir at the top of the cell to the output tube at the base. The sample was therefore picked up evenly from the

reservoir, (when the sample was pumped downwards), minimizing turbulence and eddy currents. Observations of the flow, (aided by the addition of small black particles to the clay), were made by replacing the top of the cell with a clear section of plastic. The particles flowed through the cell in straight lines to within approximately 2 cm of the outlet pipe at the bottom of the cell. No turbulence or eddy currents could be detected for the maximum obtainable flow rates. Settling was minimized by keeping the volume of the reservoir small and mounting it so that there were no horizontal surfaces for particles to settle on. Settling effects were still noticeable, (i.e. drifting of results and long relaxation times). However, to some extent these could be countered by the experimental procedure. This consisted of flowing the sample at the maximum flow rate in reverse, (up the cell), this had the effect of blowing air through the reservoir, thoroughly mixing the sample. The desired flow rate would then be selected, and the pump reversed, (so that the flow was now in the correct direction for unturbulent flow, i.e. down the cell). A reading of intensity would then be recorded.

The dimensions of the cell ensured that the dominant shear field was between the closest surfaces. For flow between two parallel plates, infinite in lateral extent, the velocity profile is a parabola. If we assume that the velocity profile within the cell was parabolic then the shear field within the sample may be determined.

Let the dimensions of the cell be $2a$ and $2b$, where $a \ll b$.



The volume flow Q is given by,

$$Q = 2b \int_{-a}^a u(x) dx.$$

Where $u(x)$ is the parabolic velocity profile of the sample,

$$u(x) = u_0 (a^2 - x^2) / a^2$$

Hence,

$$Q = 2b \int_{-a}^a u_0 (a^2 - x^2) / a^2 dx,$$

$$Q = \frac{8ba u_0}{3},$$

or,

$$u_0 = \frac{3Q}{8ab}.$$

The shear rate G is given by

$$G = \frac{du}{dx} = \frac{3Qx}{4a^2b}$$

Hence at the walls, ($x=a$), where the shear rate is a maximum,

$$G_w = \frac{3Q}{4a^2b},$$

The mean shear rate, (when $x=a/2$), is given by,

$$G_m = \frac{3Q}{8a^2b}.$$

Turbulence may be expected if the Reynolds number is greater than approximately 1000. The Reynolds number is given by the expression,

$$R = \frac{3Q \rho}{8a^2 \eta}$$

For a kaolinite sample of volume fraction 0.025, $R = 1000$ corresponds to a mean shear rate of 1560 sec^{-1} . It was earlier shown that a shear rate of 45 sec^{-1} corresponds to a Peclet number of approximately 1, hence large Peclet numbers may be obtained using this apparatus with no danger of turbulence.

(9.2.1) Spherical latex samples.

Experiments were conducted to determine the response of the optical fibre detection system as a function of the scattering parameter of the flowing sample. The intensity transmitted to each fibre was measured as a function of volume fraction of a sample of spherical latex particles, (of mean particle diameter 0.18 microns). The scattering parameter of the latex samples had previously been determined, as a function of volume fraction, using the single optical fibre bundle method detailed in chapter 5. The received intensity as a function of sample scattering parameter is illustrated in figs (9.2.3) and (9.2.4). The received intensity was noted to be independent of the shear rate, as to be expected for a sample of spherical particles.

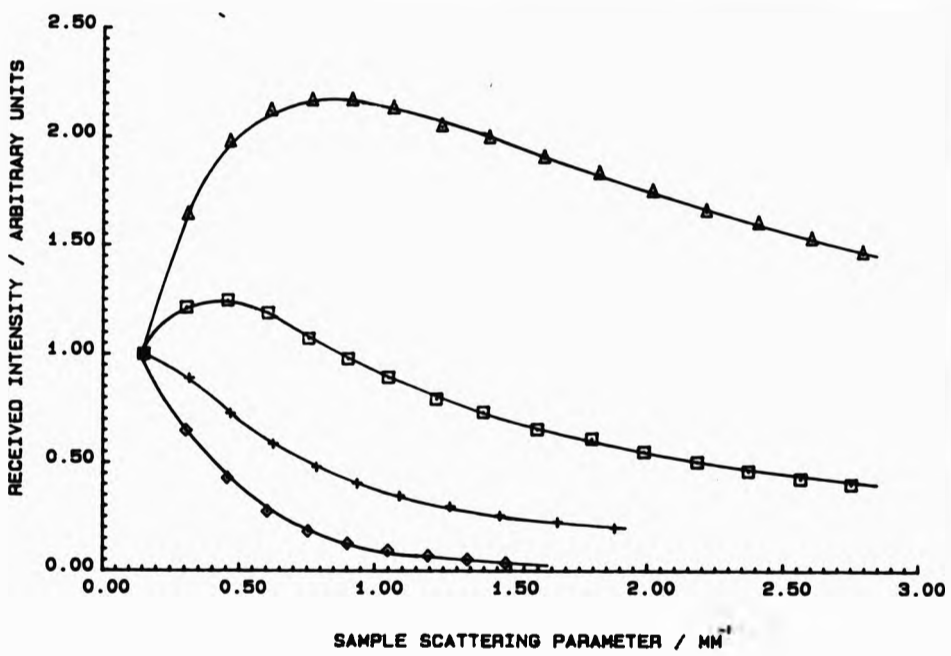


Fig (9.2.3)
 Received intensity as a function of sample scattering parameter for fibres 1,2,3 and 4. 0.18 μm spherical latex samples. Wavelength = 589 nm. Triangles = fibre 1, squares = fibre 2, crosses = fibre 3 and diamonds = fibre 4.

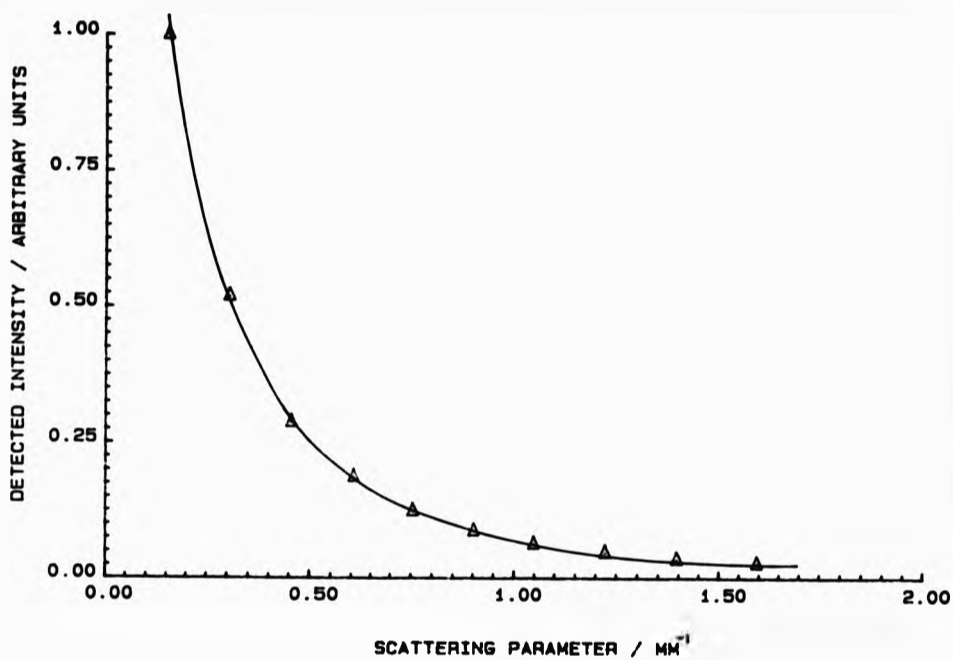


Fig (9.2.4)
 Received intensity as a function of sample scattering
 parameter for fibre 5. 0.18 μm spherical latex samples.
 Wavelength = 589 nm.

It can be seen from fig (9.2.3) that the received intensity initially increases, for fibres 1 and 2, as the scattering parameter of the sample is increased. A peak in received intensity is reached after which it falls. No such rise in received intensity can be detected for fibres 3 and 4. The peak in intensity can be explained in terms of the fibre geometry. To analyse the transmission of light through the cell it is instructive to visualise four diffuse fluxes within the sample. Two fluxes travel up and down, (i and j respectively), in a direction parallel to the

fibre sides. Two further fluxes, (k and l) travel along the cell, parallel to the fibre faces. See fig (9.2.5).

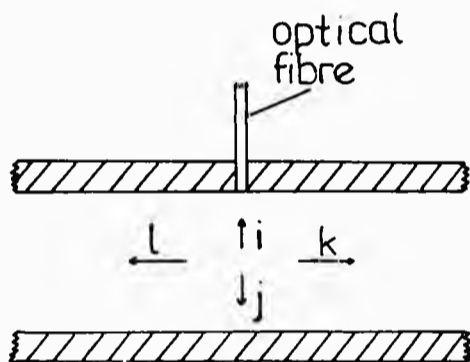


Fig (9.2.5)
Four fluxes travelling within flow cell.

For a sample of zero scattering parameter only the downward flux j , due to the illuminating fibre, would be finite. There would be no interchange to the other three fluxes as there is no scattering. Hence no flux would be detected by fibres 1,2,3 and 4. Increasing the scattering parameter from zero would result in some of the downward flux j being scattered into the upward flux i , and the sideways fluxes k and l . Hence fibres 1,2,3 and 4 would now detect some reflected flux. As the scattering parameter of the sample is increased further, more flux is scattered into i , k and l from j and hence the flux detected by fibres 1,2,3 and 4 increases with increasing sample scattering parameter. Fibres 1,2,3 and 4 detect the upward flux i , but as we travel laterally away from the illuminating fibre, fibre 0, i is increasingly dependent upon the

lateral fluxes k and l . As the scattering parameter of the sample is increased, so the attenuation of k and l with distance is increased, hence the upward flux i decreases with increasing fibre separation, d . For any given fibre separation a point will be reached where the increase in k and l due to an increase in scattering from j will be negated by the increase in attenuation of k and l . At this point a maximum in intensity will be detected by that fibre. Any further increase in the scattering parameter of the sample will result in a decrease in the detected flux. For low fibre separations the attenuation of k and l is low, hence the peak in detected intensity occurs for high scattering parameters. For large fibre separations the attenuation of k and l is large, hence the peak in detected intensity occurs at low sample scattering parameters. The response of the detecting fibres can therefore be characterized as follows;

- (i) Before the peak in received intensity is reached the received intensity is dominantly determined by diffuse reflection from the sample, i.e. the intensity increases with increasing scattering parameter.
- (ii) After the peak in received intensity is reached the received intensity is dominantly determined by diffuse transmission through the sample, i.e. the intensity decreases with increasing scattering parameter.

The turnover point between predominantly reflected to predominantly transmitted flux is determined by the product Sd , where d is the separation between the illuminating and detecting

fibres and S is the scattering parameter of the sample. This is illustrated in the calibration curves. It can be seen from fig (9.2.3) that for fibre 1, with a separation of 2.68 mm, the peak in received intensity occurs at a sample scattering parameter of approximately 0.6 mm^{-1} . Hence the product Sd , for the peak intensity, is 1.6. For fibre 2, with a separation of 5.60 mm, the peak occurs at a sample scattering parameter of 0.3 mm^{-1} , i.e. for fibre 2 the peak intensity occurs for an Sd of approximately 1.7. Taking a mean of these two Sd values it is possible to calculate the value of S for which the peak in intensity occurs for fibres 3 and 4. For fibre 3, separation 8.65 mm, $S(\text{peak}) = 0.19 \text{ mm}^{-1}$. For fibre 4, separation 11.44 mm, $S(\text{peak}) = 0.14 \text{ mm}^{-1}$. The scattering parameters of the latex samples used to obtain the data illustrated in fig (9.2.3) were greater than 0.2 mm^{-1} . This would explain why no maxima were observed for fibres 3 and 4. Hence, so long as the product $Sd > 1.7$ the detected flux is predominantly transmitted.

It is important to consider what may be concluded from these results about the path of the detected light through the sample. When the detected intensity is increasing with increasing scattering parameter, i.e. the detected flux is dependent on reflection from the sample, the majority of the detected flux must have travelled through the sample parallel to the velocity gradient. Hence, observations of the sample would be mostly dependent upon the scattering parameter of the sample parallel to the velocity gradient. When the intensity is decreasing with increasing scattering parameter, i.e. the detected flux is dominantly dependent upon lateral transmission through the

sample, the majority of the detected flux must have travelled through the sample parallel to the velocity vector. Hence observations would depend mostly upon the scattering parameter of the sample parallel to the velocity vector.

The above discussion has neglected fibre 5, the fibre mounted directly opposite the input fibre. It can be seen from fig (9.2.4) that this fibre detects transmitted flux, (at no point does the received intensity increase with increasing scattering parameter). Hence fibre 5 detects flux transmitted parallel to the velocity gradient.

(9.2.2) Kaolinite samples.

The received intensity as a function of shear rate was monitored for an SPS grade, (broad size fraction, $80\% < 2\ \mu\text{m}$), kaolinite clay sample at a volume fraction of 0.020. The scattering parameter of the sample was measured to be $5.21 \pm .08\ \text{mm}^{-1}$, using the single optical fibre bundle method detailed in chapter 5, giving $Sd = 6.2$ for the minimum fibre separation. From the criterion of section (9.2.1) it therefore follows that all the detecting fibres were operating in transmission mode. The received intensity change as a function of shear rate for fibres 1,2,3 and 4 is illustrated in fig (9.2.6). Fig (9.2.7) illustrates the received intensity change detected for fibre 5. The clay sample was prepared as detailed in section 1.3 for maximum deflocculation. Fibre 0 was used to illuminate the sample, as in the previous

experiment. (It was necessary to use a relatively dilute sample as for volume fractions > 0.02 the attenuation of light was too great to obtain results from fibre 4).

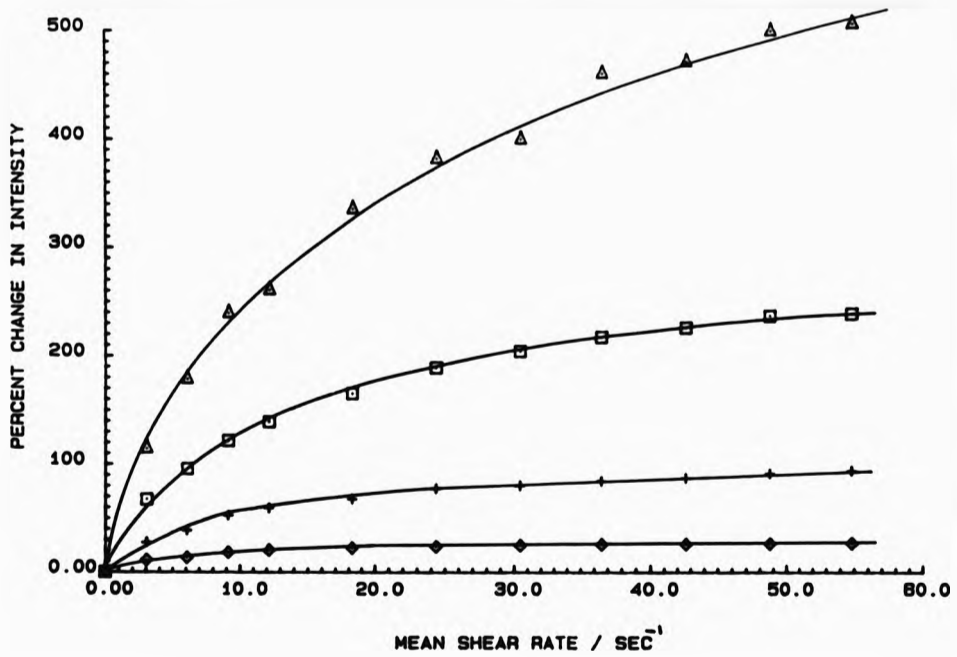


Fig (9.2.6)
 Received intensity change as a function of the mean shear rate for fibres 1,2,3 and 4. SPS grade kaolinite sample. Wavelength = 589 nm. Volume fraction = 0.02. Triangles = fibre 4, squares = fibre 3, crosses = fibre 2, diamonds = fibre 1.

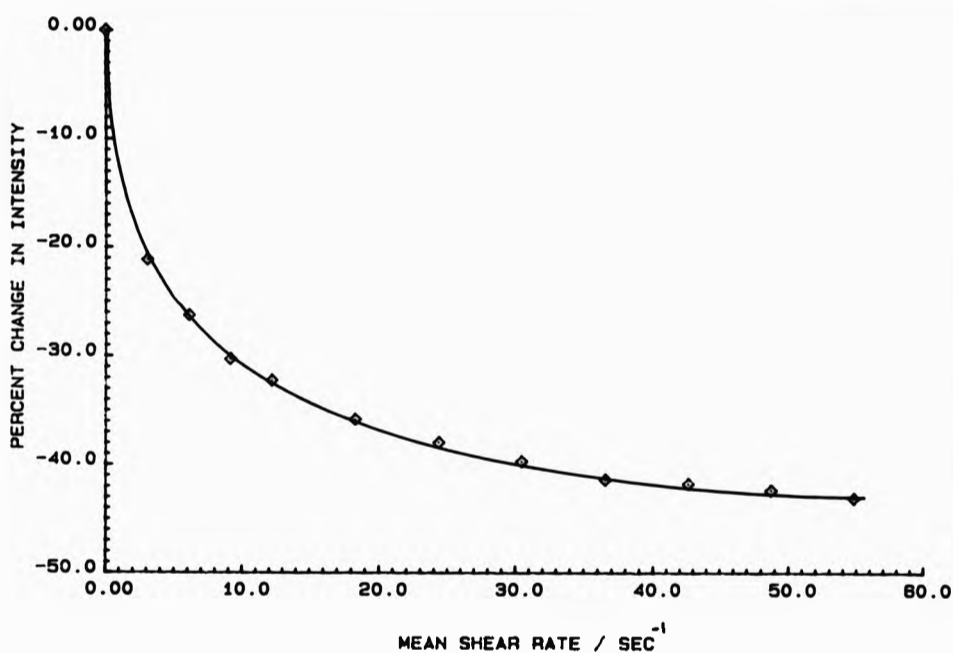


Fig (9.2.7)
 Received intensity change as a function of the mean
 shear rate for fibre 5. SPS grade kaolinite sample.
 Wavelength = 589 nm. Volume fraction = 0.02.

It can be seen from fig (9.2.6) that the observed intensity change is highly dependent upon the fibre separation. At a fibre separation of 1.04 cm, (fibre 4 detecting), the maximum observed change in intensity was approximately 500 %. The changes in intensity illustrated in fig (9.2.6) were converted into changes in effective scattering parameter S , using the data obtained with the latex samples. The effective scattering parameter as a function of

shear rate is illustrated in fig (9.2.8) for fibres 1,2,3 and 4, and in fig (9.2.9) for fibre 5.

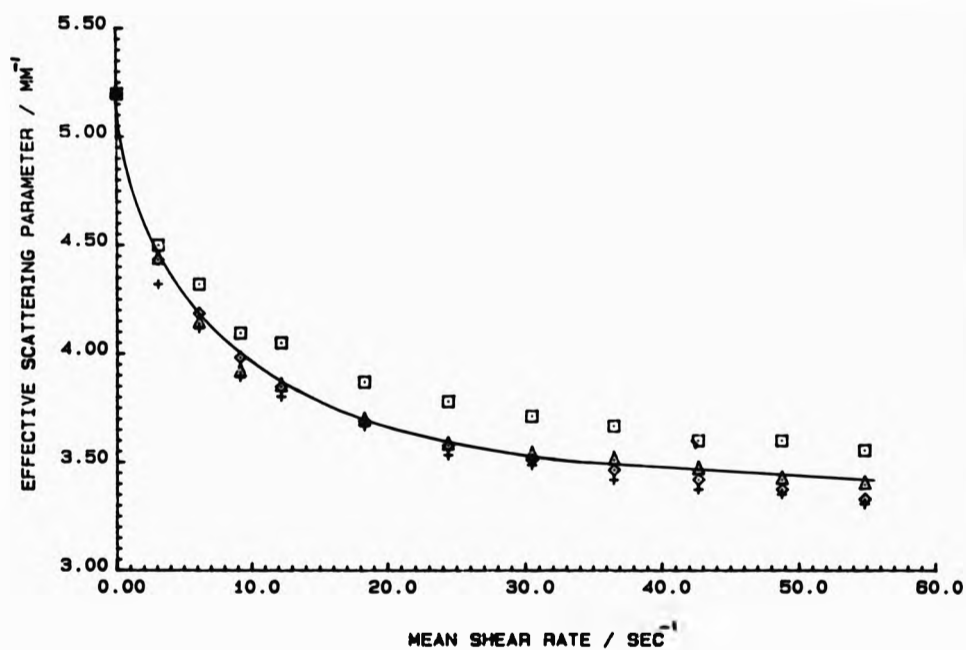


Fig (9.2.8)
 Effective scattering parameter as a function of the mean shear rate for fibres 1,2,3 and 4. SPS grade kaolinite sample. Wavelength = 589 nm. Volume fraction = 0.02. Triangles = fibre 4, squares = fibre 3, crosses = fibre 2, diamonds = fibre 1.

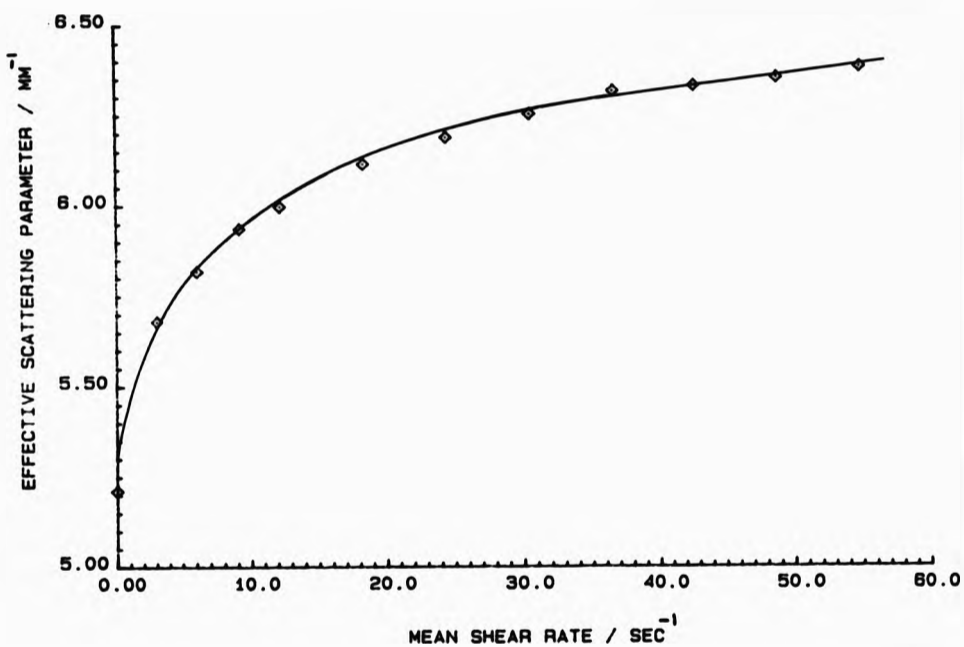


Fig (9.2.9)
 Effective scattering parameter as a function of the
 mean shear rate for fibre 5. SPS grade kaolinite sample.
 Wavelength = 589 nm. Volume fraction = 0.02.

It can be seen from fig (9.2.8) that there is good agreement between the values of S measured by the four fibres. We would expect that the measured change in S would be dependent upon the path of the light within the sample, (as the scattering parameter is directionally dependent). Hence it can be concluded from the data illustrated in fig (9.2.8) that the proportion of the light

path travelled by the detected light in any given direction is approximately the same for all four detecting fibres.

The data presented in figs (9.2.8) and (9.2.9) can be interpreted as showing that the effective scattering parameter increases on shear when the sample is viewed parallel to the velocity gradient, and decreases when viewed parallel to the velocity vector. This is in good agreement with the proposed model of particle orientation in shear fields, assuming that an increase in geometric cross-section presented to the propagating flux results in an increase in the scattering parameter. This assumption is later examined in section (9.3.3) and is shown to be valid for multiple scattering platelets.

Experiments were conducted on SPS grade kaolinite clay samples with volume fractions between 0.01 and 0.30. Figure (9.2.10) illustrates the percentage change in effective scattering parameter, observed when switching from a mean shear rate of 0 to 55 sec^{-1} , as a function of volume fraction.

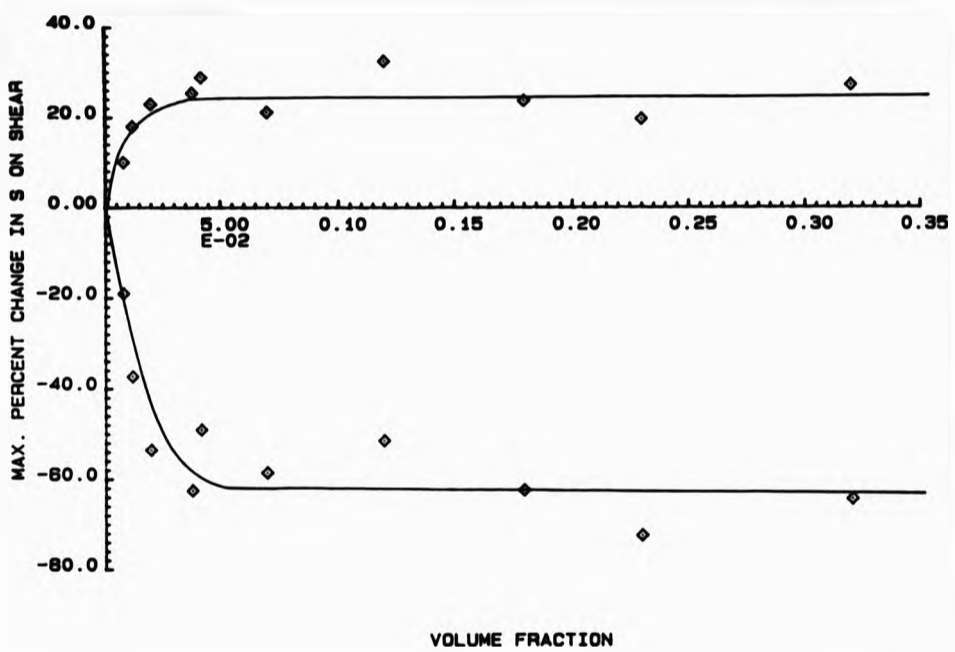


Fig (9.2.10)
 Percentage change in effective scattering parameter as a function of sample volume fraction. Change in scattering parameter measured in varying the mean shear rate from 0 to 55 sec⁻¹ SPS grade kaolinite samples. Lower curve = observations parallel to velocity vector, upper curve = observations parallel to the velocity gradient. Wavelength = 589 nm.

It can be seen from fig (9.2.10) that;

- (1) When viewed parallel to the velocity gradient the maximum percentage change in effective scattering parameter induced by shear alignment of the particles remained approximately constant with volume fraction at 25 +/- 5 %, for volume

fractions between 0.02 and 0.30.

(11) When viewed parallel to the velocity vector the maximum percentage change in effective scattering parameter induced by shear alignment of the particles remained approximately constant with volume fraction at $65 \pm 5\%$, for volume fractions between 0.03 and 0.30.

It is difficult to meaningfully compare the data obtained at low volume fractions with that obtained at high volume fractions. At low volume fractions multiple scattering becomes negligible, altering the interpretation of the results. The drop in the change in effective scattering parameter below volume fractions of 0.03 is therefore interpreted as illustrating the transition from single to multiple scattering, as opposed to a change in kaolinite particle interactions.

The maximum change in the effective scattering parameter on flow is approximately 3 times greater when the sample is viewed parallel to the velocity vector than when the sample is viewed parallel to the velocity gradient.

(9.2.3) Flocculation detection.

Experiments were conducted to ascertain whether particle flocculation could be detected optically using the slot-flow cell. When flocs form within a kaolinite sample a large 'house-of-cards' type structure is formed [8]. These large structures will be approximately spherical, i.e. they cannot be aligned, (as the individual particles can), by a shear field. Hence the scattering parameter of a completely flocculated kaolinite sample under shear is isotropic, and hence no flow-induced optical changes should be apparent. Flocculation of particles may be induced either by manipulating the pH of the sample, or by varying the dosage of deflocculant, Dispex being used in the studies below. The active ingredient of Dispex is sodium polyacrylate.

(9.2.4) Flocculation induced by pH adjustment.

A broad size fraction, (SPS grade) clay sample of volume fraction 0.01 was prepared as detailed in section (1.3). i.e. 0.21% (by dry weight of clay), of sodium polyacrylate in the form of Dispex was added and the pH adjusted to 8.5 by the addition of a sodium hydroxide solution. Half of the sample was placed in the slot-flow cell, and the intensity change on shearing the sample, (at a mean shear rate of 49 sec^{-1}), as a function of decreasing pH, recorded from fibre 3. The pH of the sample was decreased by the addition of 1M hydrochloric acid. The scattering parameter of the sample was measured using the single optical fibre bundle method

detailed in chapter 5 to be $2.65 \pm 0.05 \text{ mm}^2$; the input to output separation fibre was 8.65 mm, giving $Sd = 23$. Hence the fibre system was operating in transmission mode. The flow cell was then emptied and cleaned and the remaining original solution placed in the cell. The change in intensity on flow was monitored for increasing pH by the addition of 1M sodium hydroxide. The same illumination and detection system as detailed earlier were used, and the detected radiation filtered to 589 nm. The results obtained are illustrated in fig (9.2.11).

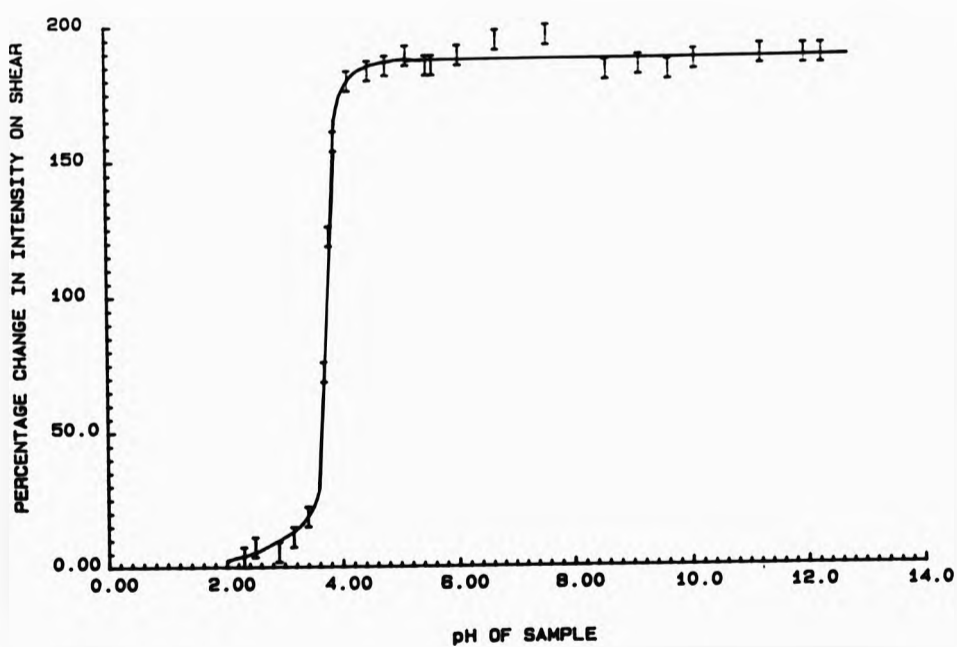


Fig (9.2.11)
Intensity change on flow as a function of sample pH.
Kaolinite clay, SPS grade. Volume fraction = 0.01.
Wavelength = 589 nm.

It can be seen from the results that there is a very sharp decrease in the change in intensity on shear at a pH of approximately 4. The change in intensity of approximately 200 % for pH > 4.8 sharply drops to a change of about 10 % for pH < 3.5. Similar results are presented by Molloy [9] for kaolinite samples undergoing ultrasonic orientation. The results of Molloy show the sharp drop occurring at higher pH, approximately 6, this is probably due to the difference in sample preparation between the experiments. Molloy prepared several samples of differing pH prior to the experiment. In these experiments the pH of one sample was manipulated in situ, it may well be that the clay hydrochloric acid reaction had not gone to completion when the intensity readings were recorded. This experiment illustrates the accuracy with which particle flocculation may be monitored using the slot-flow cell.

It was noted during the experiments that the intensity detected from fibre 3 remained constant with pH for the unsheared sample, i.e. the scattering parameter of an unsheared kaolinite sample is independent of sample pH. This is in good agreement with the results of Molloy [9].

(9.2.5) Flocculation induced by Dispex dose adjustment.

An SPS grade kaolinite clay sample of volume fraction 0.15, (31.4 % by weight), was prepared without the addition of Dispex and the pH adjusted to 8.5. The sample was placed in the slot-flow cell and the intensity change as a function of shear rate recorded. Long

relaxation times were noted for the zero flow reading. This was presumably due to the increased density and viscosity of the high volume fraction kaolinite sample. This effect, combined with the drifting of results due to settling, made it difficult to obtain consistent results. To overcome this the change in intensity between mean shear rates of 2.9 sec^{-1} and 49 sec^{-1} were measured as a function of Dispex dose. The results are illustrated in fig (9.2.12).

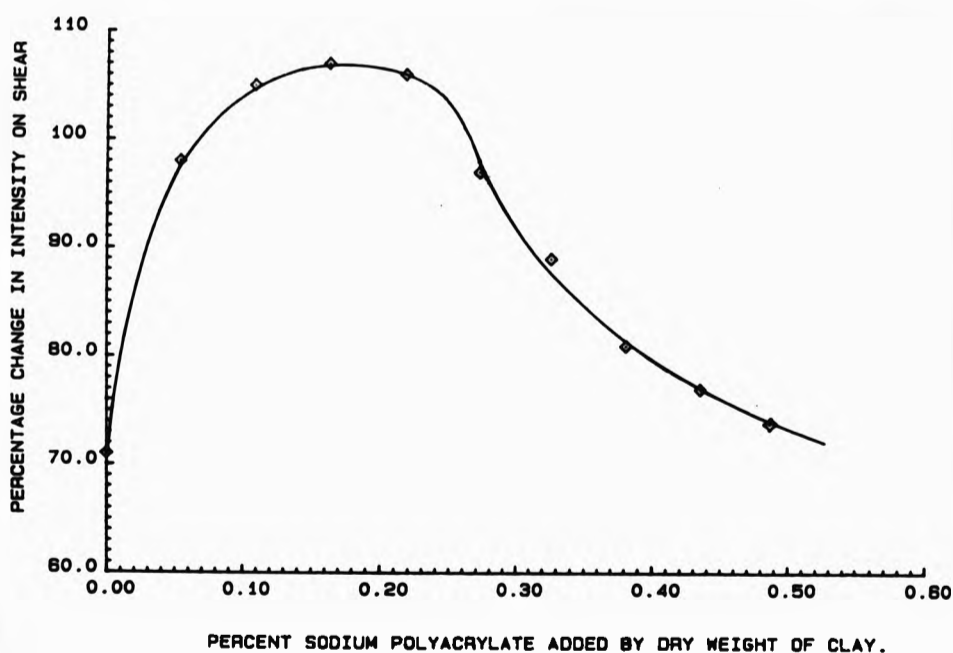


Fig (9.2.12)
Intensity change on flow as a function of Dispex dose.
Kaolinite clay, SPS grade. Volume fraction = 0.15.
Wavelength = 589 nm.

It can be seen from the results that a maximum intensity change is observed at a sodium polyacrylate dose of 0.20 % by dry weight of clay. This is in good agreement with measurements of viscosity of SPS as a function of sodium polyacrylate dose [61] carried out by English China Clays, see fig (9.2.13).

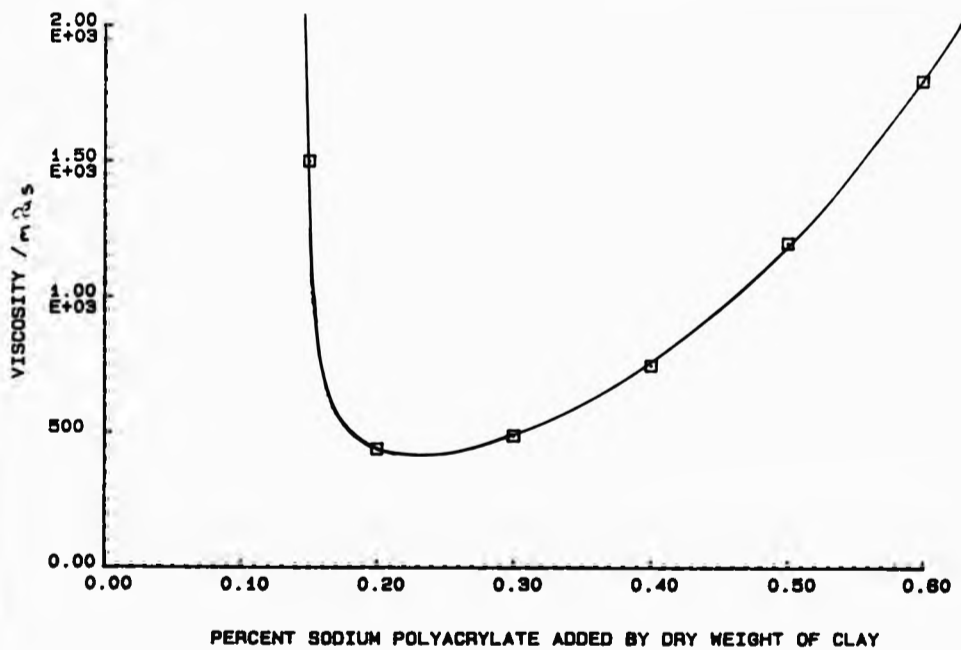


Fig (9.2.13)
Viscosity of SPS grade kaolinite dispersion as a function of Dispex dose. Data supplied by English China Clays.

The viscosity of a kaolinite sample is dependent upon its state of flocculation. The higher the flocculation, the greater the average inter-particle forces, the higher the viscosity.

Therefore the minimum in the viscosity corresponds to maximum deflocculation of the sample. Hence the maximum intensity change on shear due to shear particle alignment will coincide with the minimum in viscosity. It can be seen from a comparison of figs (9.3.2) and (9.3.3) that this is indeed the case.

The decrease in the change of scattering parameter, and the increase in viscosity, noted for sodium polyacrylate doses $> .23 \%$ is interpreted as evidence for reflocculation of the sample. This has been reported elsewhere [9], however the exact mechanism of this effect is unclear.

(9.3) Concentric cylinder shear cell.

In the previous rheo-optical systems the velocity gradient created within the sample was not constant over the volume of sample under observation. To overcome this a shear system was developed consisting of two concentric cylinders manufactured from black acetyl acetate. Five polymer, multimode optical fibres, of numerical aperture 0.47 and diameter 1 mm were mounted along the circumference of the exterior cylinder. These are termed the azimuthal set. Four further fibres were mounted along the axis of the exterior cylinder, orthogonal to the first line of fibres, these are termed the axial set. The ends of the fibres were polished smooth with the internal face of the exterior cylinder. The dimensions are given in fig (9.3.1).

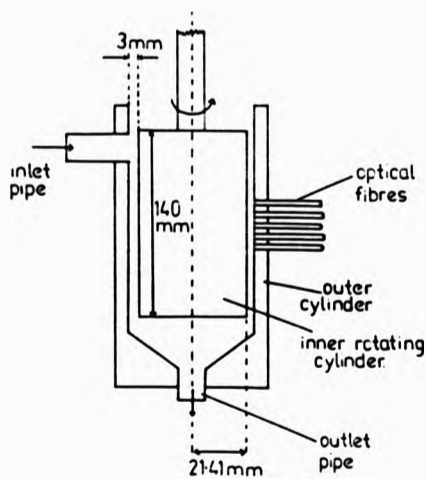


Fig (9.3.1)
Concentric shear cell.

The outer rotor was designed to fit in place of the stator in a Haake RV100 rheometer. The inner cylinder was rotated using the rheometer controls. The same illumination and detection systems as detailed previously were used to illuminate the sample and detect the reflected flux. Fibre 0 was used to illuminate the sample, and fibres 1 to 8 used to detect the transmitted flux. The optical fibre mounting geometry is given in fig (9.3.2). The detected flux was filtered to 589 nm immediately before the photodetector.

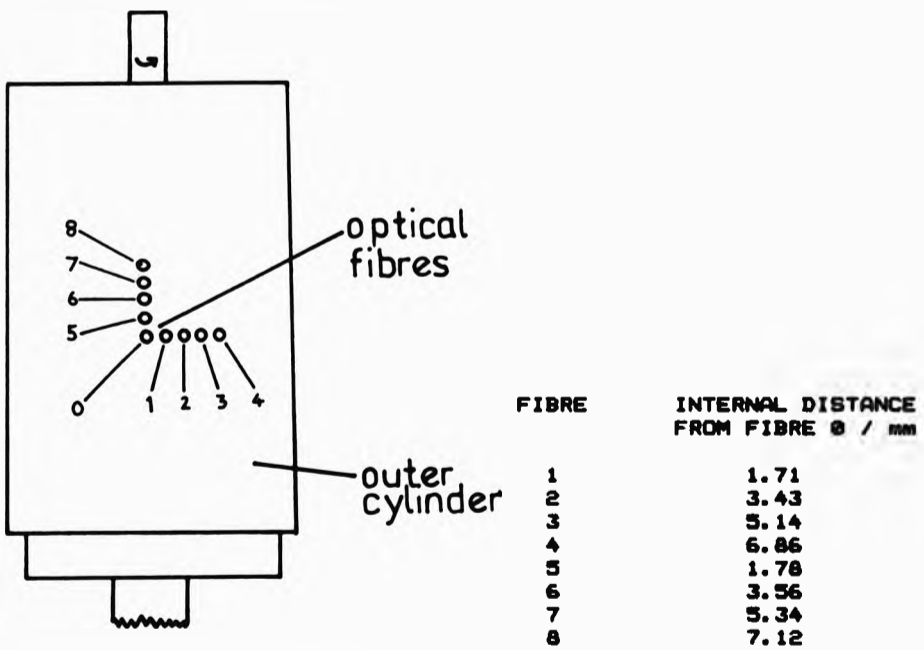


Fig (9.3.2) Optical fibre mounting geometry. Fibres 1,2,3 and 4 are termed the azimuthal fibres, and fibres 5,6,7 and 8 are termed the axial fibres.

To reduce the effects of settling, the sample was pumped, using a peristaltic pump, from the bottom to the top of the cell between intensity readings.

The velocity gradient G developed between the cylinders is almost constant over the sample so long as the gap to cylinder radius is small [62]. The velocity gradient G is, by definition,

$$G = R \frac{dw}{dr}$$

where R = the radial distance from the axis of rotation.

So long as the gap width s is small, (i.e. $r_1 \approx r_2$),

$$\langle G \rangle = \omega R / (r_2 - r_1),$$

where r_1 = the radius of the internal (rotating) cylinder,

r_2 = the radius of the external (stationary) cylinder,

Concentric cylinder viscometers, particularly those with the outer cylinder stationary and the inner cylinder rotating, are prone to generate Taylor vortices [62] within the cell gap at angular velocities exceeding a critical value T , given by,

$$T = \frac{\omega^2 (r_1 + r_2)}{2 \rho s^3 r_1^2}, \quad \dots(9.3.1)$$

where ν = the kinematic viscosity and

$$P = 0.00571(1-0.652(s/r)) + 0.00056/(1-0.652(s/r))^2$$

When the angular velocity T is exceeded the laminar flow of the sample is destroyed by a three-dimensional motion: the sample flow breaks up into symmetrical ring-shaped vortices spread at regular intervals along the length of the cylinder, rotating alternately in opposite directions, see fig (9.3.3). The above expression is valid for a Newtonian liquid, and hence some inaccuracy may be expected when applied to a non-Newtonian colloidal dispersion. The kinematic viscosity, and hence T is dependent upon the kaolinite sample concentration. For a sample of volume fraction 0.024, the critical value of T as predicted by equation (9.3.1) is reached at a shear rate of 15 sec^{-1} .

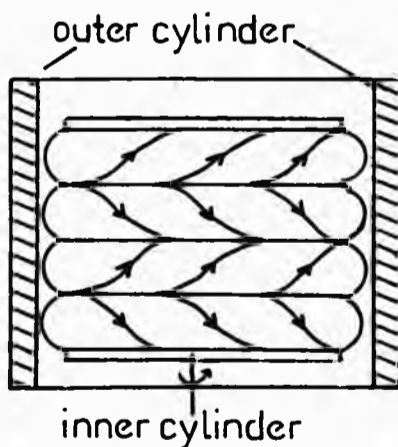


Fig (9.3.3)
Schematic illustration of Taylor vortex
flow in rotating concentric cylinders.

(9.3.1) Spherical latex samples.

The shear cell was filled with samples of monodisperse spherical latex particles suspended in water. The scattering parameters of the samples had previously been determined using the single optical fibre bundle method detailed in chapter 5. The intensity detected by each fibre was recorded as a function of sample scattering parameter. The results are illustrated in figs (9.3.4) and (9.3.5).

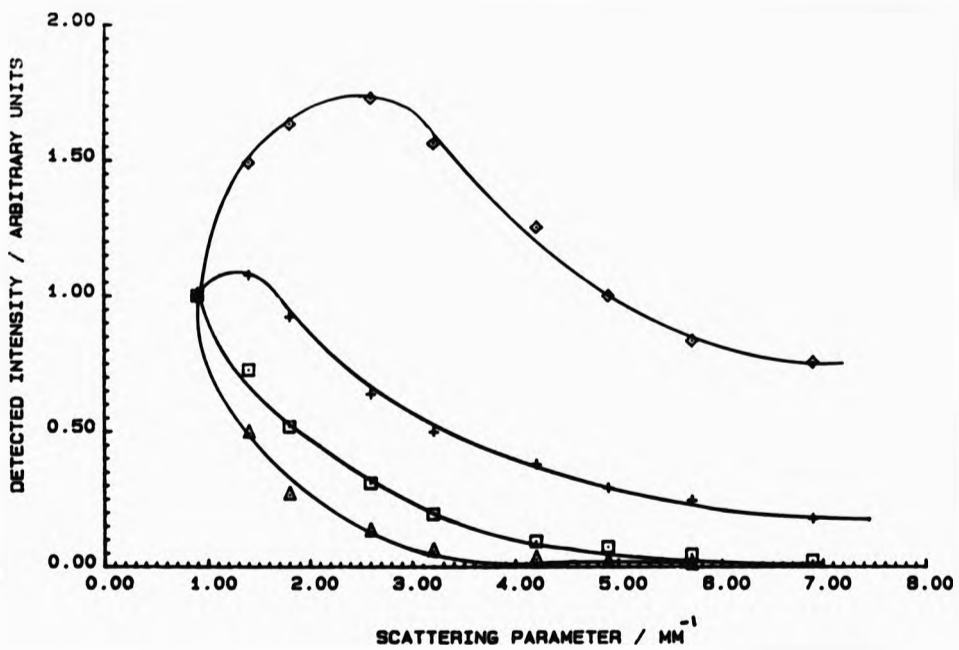


Fig (9.3.4).
Detected intensity as a function of sample scattering parameter for the azimuthal fibres 1,2,3 and 4. Spherical latex particle sample, mean particle diameter = 0.18 μm . Wavelength = 589 nm. Triangles = fibre 4, squares = fibre 3, crosses = fibre 2 and diamonds = fibre 1.

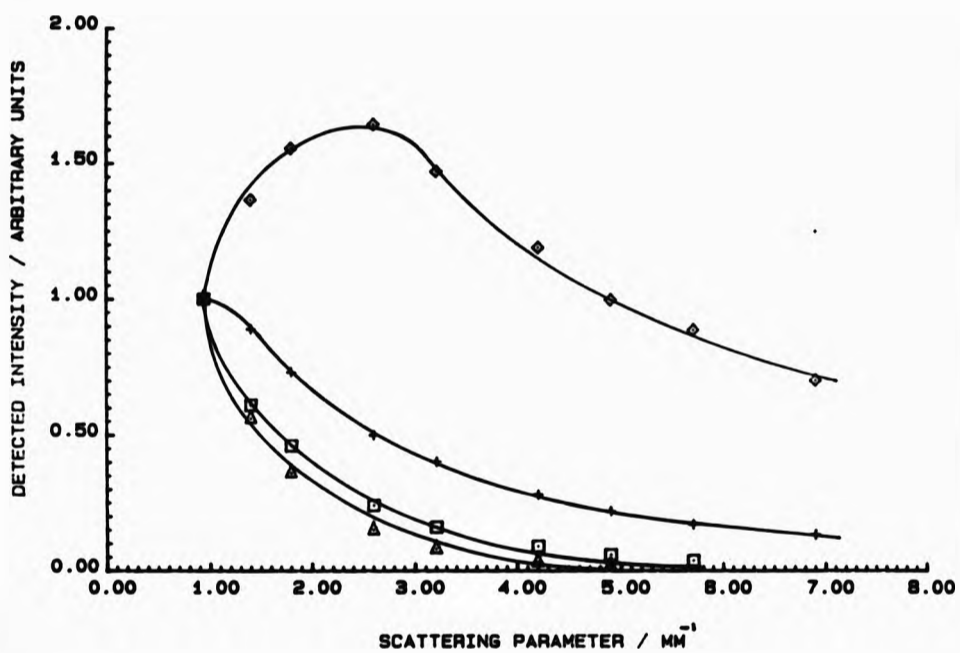



Fig (9.3.5).
 Detected intensity as a function of sample scattering parameter for the axial fibres 5,6,7 and 8. Spherical latex particle sample, mean particle diameter = $0.18 \mu\text{m}$. Wavelength = 589 nm . Triangles = fibre 8, squares = fibre 7, crosses = fibre 6 and diamonds = fibre 5.

It can be seen from figs (9.3.4) and (9.3.5) that the results obtained using spherical latex particle samples closely resemble those obtained previously in the slot-flow cell system, see fig (9.2.4), as we would expect and for the same reasons. It can be concluded from the above results that so long as the scattering parameter of the sample is greater than 2 mm^{-1} , the flux detected by the optical fibres is dominantly dependent upon transmission of



flux through the sample parallel to the (n,v) plane, (see fig (9.1.1) for axis definitions). It is important to note that the azimuthal fibres detect flux transmitted in the direction of flow (the v direction), and the axial fibres detect flux transmitted across, (orthogonal) to the flow direction, (the n direction).

It was noted that rotating the inner cylinder had no effect on the detected intensity, as is to be expected with spherical particle samples.

(9.3.2) Broad size fraction kaolinite Samples.

An SPS grade kaolinite clay sample, (of volume fraction 0.021 and $S = 5.5 \pm 0.1 \text{ mm}^2$), was prepared, as detailed in section 1.3, for maximum particle deflocculation, i.e. the pH of the sample was adjusted to 8.5 and 0.21 % by dry weight of clay of sodium polyacrylate, (in the form of Dispex). The sample was illuminated from fibre 0 and the intensity detected from fibres 1 to 8 recorded as a function of shear rate. The results are illustrated in figs (9.3.6) and (9.3.7).

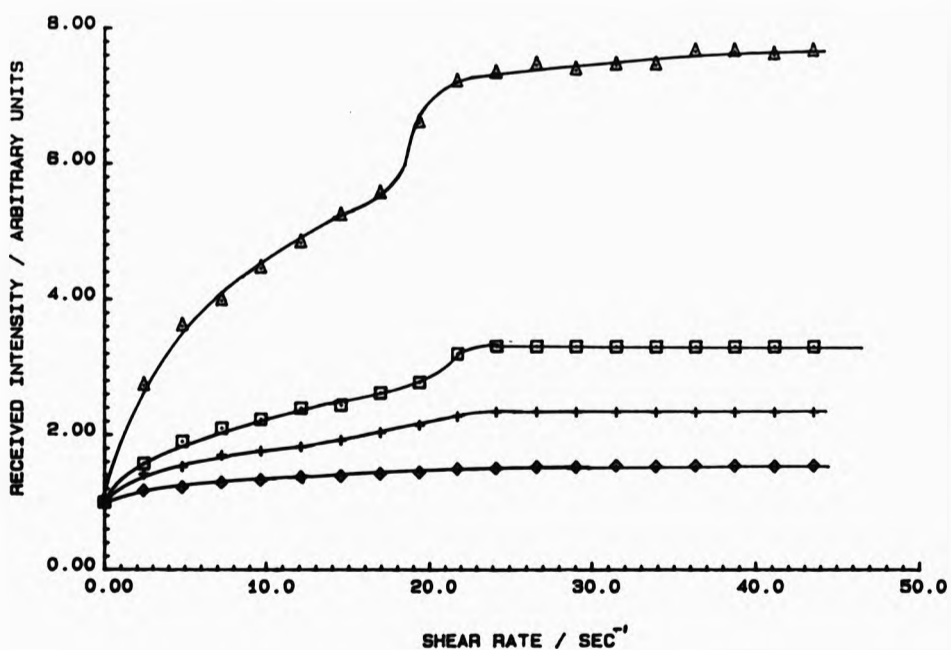


Fig (9.3.6)

Intensity detected from azimuthal fibres 1,2,3 and 4 as a function of shear rate. SPS grade kaolinite clay sample, volume fraction = 0.021. Wavelength = 589 nm. Diamonds = fibre 1, crosses = fibre 2, squares = fibre 3, triangles = fibre 4.

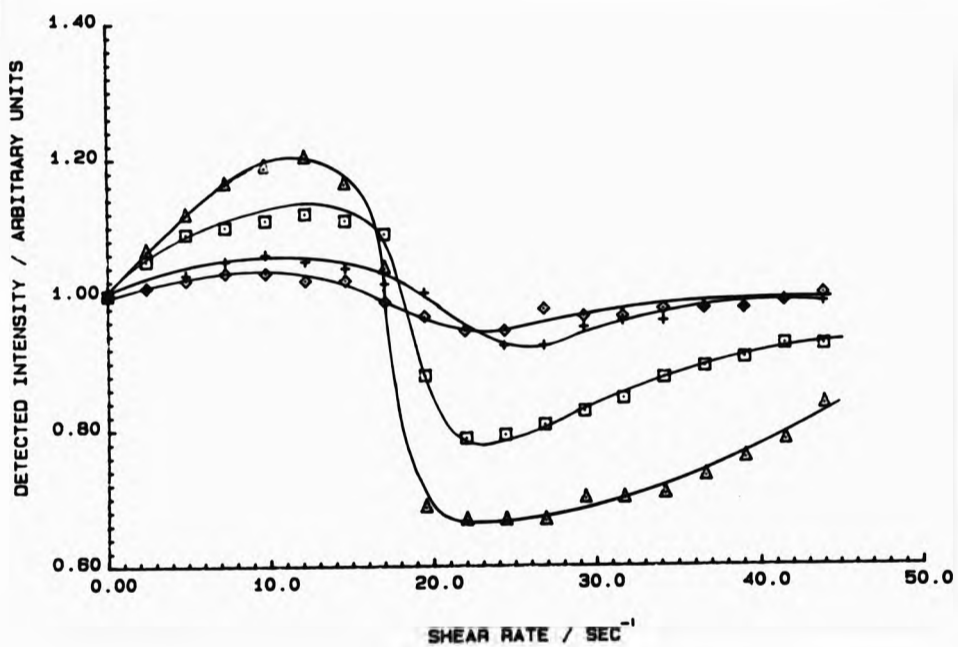


Fig (9.3.7)
Intensity detected from axial fibres 5,6,7 and 8 as a function of shear rate. SPS grade kaolinite clay sample, volume fraction = 0.21. Wavelength = 589 nm. Diamonds = fibre 5, crosses = fibre 6, squares = fibre 7, triangles = fibre 8.

The change in effective scattering parameter, calculated using the data obtained for spherical latex samples, is illustrated in figs (9.3.8) and (9.3.9).

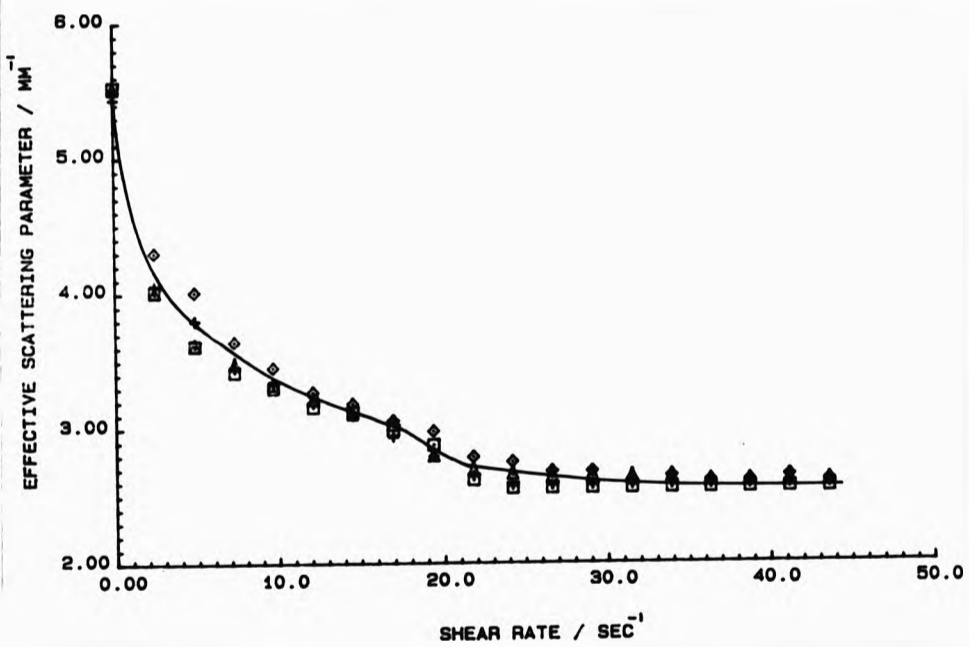


Fig (9.3.8)
 Scattering parameter as a function of shear rate for the azimuthal fibres 1,2,3, and 4. Diamonds = fibre 1, crosses = fibre 2, squares = fibre 3, triangles = fibre 4, SPS grade clay sample, volume fraction = .021.

It is clear from fig (9.3.8) that the change in effective scattering parameter experienced by the light detected by the azimuthal fibres 1,2,3 and 4 is approximately identical between the four fibres. The scattering parameters measured by the four axial fibres, fig (9.3.9), do not show such good agreement, however the

same general trends can be observed for all four axial fibres.

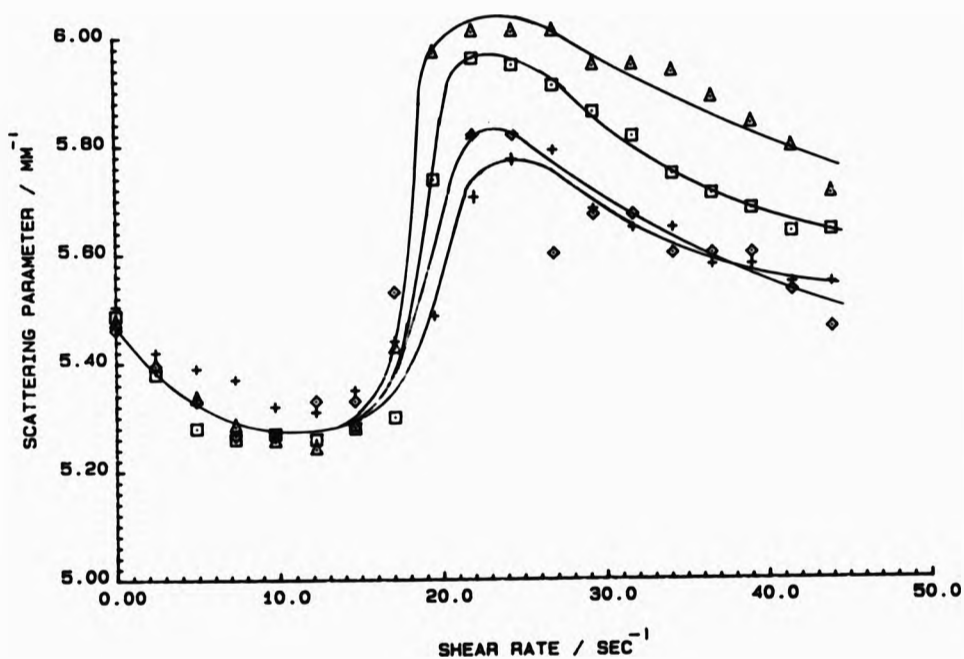


Fig (9.3.9)
Scattering parameter as a function of shear rate for axial fibres. Diamonds = fibre 5, crosses = fibre 6, squares = fibre 7, triangles = fibre 8, SPS grade clay sample, $v = .021$.

The previous graphs show three important features;

- (i) the scattering parameter of the sample decreases on shear when the sample is viewed parallel to the velocity vector, (azimuthal fibres),
- (ii) the scattering parameter of the sample initially increases only marginally when the sample is observed parallel to the n-direction, (axial fibres),
- (iii) at shear rates of approximately 17 sec^{-1} , sudden changes of

scattering parameter with shear are observed for both the azimuthal and axial fibres.

Points (i) and (ii) may be explained in terms of a simple model of particle orientation. The kaolinite particles population is split into three orientation sets corresponding to the three principal axes X, Y and Z. Random orientation is then represented by the particle face normals of each set being aligned with one of the principal axes. See fig (9.3.10).

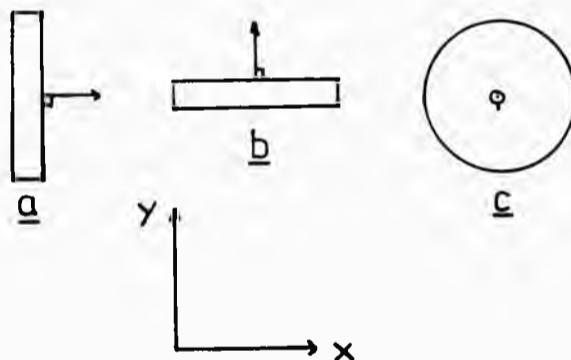


Fig (9.3.10)

Simple model of random orientation of kaolinite particles. Set (a), particle face normal parallel to X-axis. Set (b) particle face normal parallel to Y-axis. Set (c), particle face normal parallel to Z-axis. Z-axis out of plane of paper.

The effect of simple shear fields on a kaolinite sample may be easily evaluated in terms of this model. Fig (9.3.11) illustrates the effect of applying a velocity gradient in the Z-direction, (velocity vector in X-direction), to a sample initially in the random state.

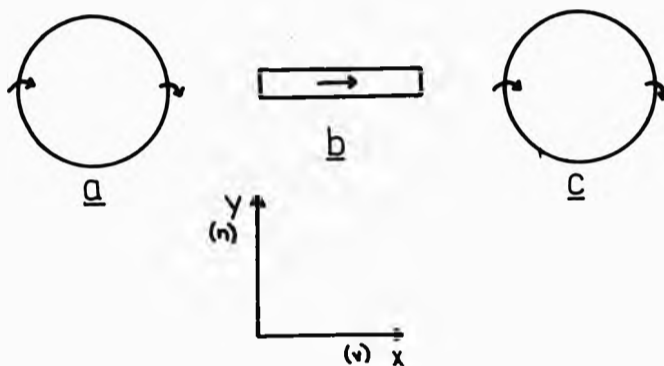



Fig (9.3.11)
Effect of shear field on particle orientation. Velocity vector in the X-direction. Velocity gradient in the Z-direction. Z-axis into plane of paper.

The particles in sets (a) and (c) will experience a minimum torque when their particle face normals are aligned with the Z-axis. Hence the particles will rotate with a non-constant angular velocity, spending most of their time with their particle face normals aligned with the Z-axis. The particles in set (b) will experience a torque causing them to rotate about the Y-axis.

The azimuthal fibres detect flux that has been transmitted in the X-direction, (i.e. the v-direction). Note that for simplicity the curvature of the cylinders is neglected here, the Y-axis is defined as being parallel to the axis of rotation of the inner cylinder, (the n-direction), the Z-axis is defined, (at any point along the gap radius), as pointing towards the axis of rotation, (the G-direction), the X-axis is hence at a tangent to the cylinders. It can be seen from fig (9.3.10) that when the




particles are randomly orientated flux travelling in the X-direction will see one third of the particles face-on, corresponding to set (a), and two-thirds of the particles edge-on, corresponding to sets (b) and (c). After the particles have been aligned by the shear field, flux travelling in the X-direction will see all the particles edge-on, fig (9.3.11). Hence there is a net decrease in the geometric cross-section presented to flux travelling in the X-direction due to shear alignment of particles.

The axial fibres detect flux that has been transmitted in the Y-direction, (i.e. the n-direction). Hence for random orientation the axial fibres observe two-thirds edges and one-third faces, fig (9.3.10). When the particles have been aligned by the applied shear field the axial fibres still detect two-thirds edges and one-third faces, fig (9.3.11). Hence no change in scattering parameter would be observed according to this model.

The predictions of this model are in broad agreement with the experimental results observed at low shear rates; a large decrease in scattering parameter on shear is observed by the azimuthal fibres, very little initial change in scattering parameter is observed by the axial fibres.

The above model gives an adequate qualitative explanation of the results observed for low shear rates. However, at shear rates of approximately 17 sec^{-1} sudden changes in the scattering parameter are observed by both the axial and the azimuthal fibres. It can be concluded from this that either the simple two-dimensional laminar



flow of the sample was disturbed at high shear rates, or the nature of the kaolinite particle interactions was altered by the applied shear field. Equation (9.3.1) predicts that Taylor vortices will be formed for shear rates greater than 12 sec^{-1} for a kaolin sample of volume fraction 0.024, it therefore seems likely that the sharp transitions apparent for both axial and radial observations of the sample are due to Taylor vortices forming within the sample. The agreement between the experimental and theoretical onset of vortex flow is surprisingly good considering equation (9.3.1) is only strictly valid for a Newtonian liquid, whereas kaolinite suspensions are non-Newtonian colloidal dispersions. Taylor vortices will produce a three dimensional flow within the cell, see fig (9.3.12). This will result in additional velocity components in both the Y and Z-directions. The orientation of the particles will then be dependent on the relative strengths of the velocity components. If the velocity vector in the X-direction is dominant, (as is the case prior to vortex flow being initiated), then little change in the particle orientation, (and hence the observed value of S), will result. However, in the circular flow generated within the vortex, the velocity vector of any particle is a function of its position along the Y-axis. Hence, the different groups of particles observed by each of the azimuthal fibres, (which are mounted in the cell normal to the Y-axis), all have approximately the same distribution of velocity components. Therefore, the same degree of average particle orientation, (and hence S), is observed by each of the azimuthal fibres. However, the groups of particles observed by the axial fibres, (mounted parallel to the Y-axis), will in general have differing velocity

component distributions. Hence different degrees of average particle orientation, and hence different S values, will be observed by each axial fibre.

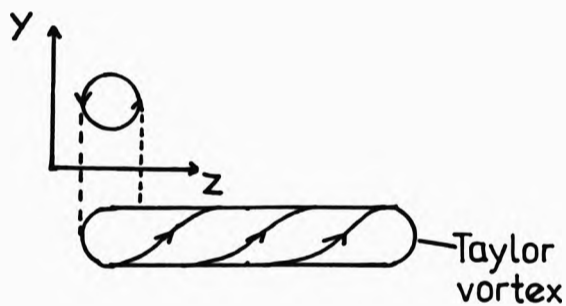


Fig (9.3.12)
Schematic illustration of a Taylor Vortex generating velocity components in the Y and Z-directions.

(9.3.3) Concentration dependence.

Experiments were conducted on SPS grade kaolinite samples with volume fractions between 0.03 and 0.30, using the four azimuthal detecting fibres. Fig (9.3.13) shows that the percentage increase in scattering parameter on initiating laminar flow was independent of volume fraction at $55 \pm 5\%$, in reasonable agreement with the results from the previous slot-flow rheo-optical experiments. For all concentrations the scattering parameter dependence on shear rate resembles that illustrated in fig (9.3.7).

The same sharp decrease in scattering parameter was noted between shear rates of 15 to 25 sec^{-1} for all the samples, indicating the onset of Taylor vortex flow.

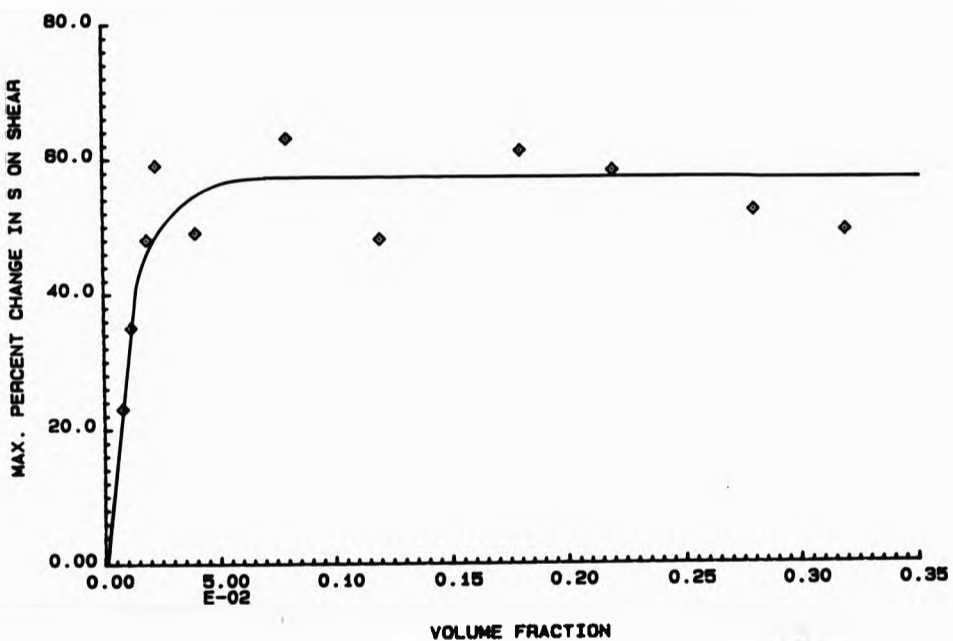


Fig (9.3.13)
Percentage increase in effective scattering parameter as a function of sample volume fraction. SPS grade kaolinite sample. Wavelength = 589 nm.

(9.3.4) Fractionated kaolinite samples.

Kaolinite samples of nominal equivalent spherical diameter (e.s.d.) ranges 0.4-0.5, 0.7-0.8, 1-2, 2-3, 3-4 and 5-6 microns were prepared in the usual manner for maximum particle deflocculation. The samples were supplied by English China Clays. Fig (9.3.14) illustrates the distribution in particle face

diameters for a nominal 0.4-0.5 micron e.s.d. sample.

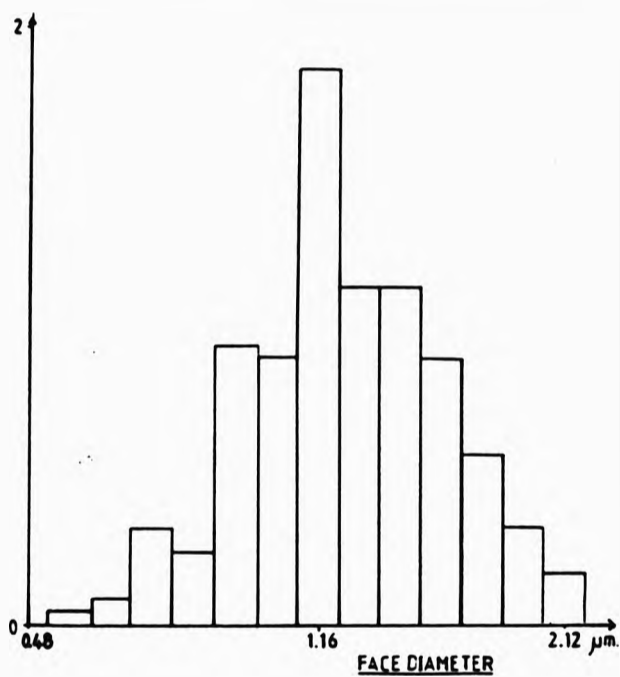


Fig (9.3.14)
Particle face diameter distribution obtained from scanning electron micrograph of nominal 0.4-0.5 micron e.s.d. sample.

The samples were placed in the cell and the inner cylinder rotated. The intensity detected from the azimuthal fibres as a function of velocity gradient generated within the sample was recorded. Figure (9.3.15) illustrates the percentage change in effective scattering parameter as a function of shear rate for all the samples.

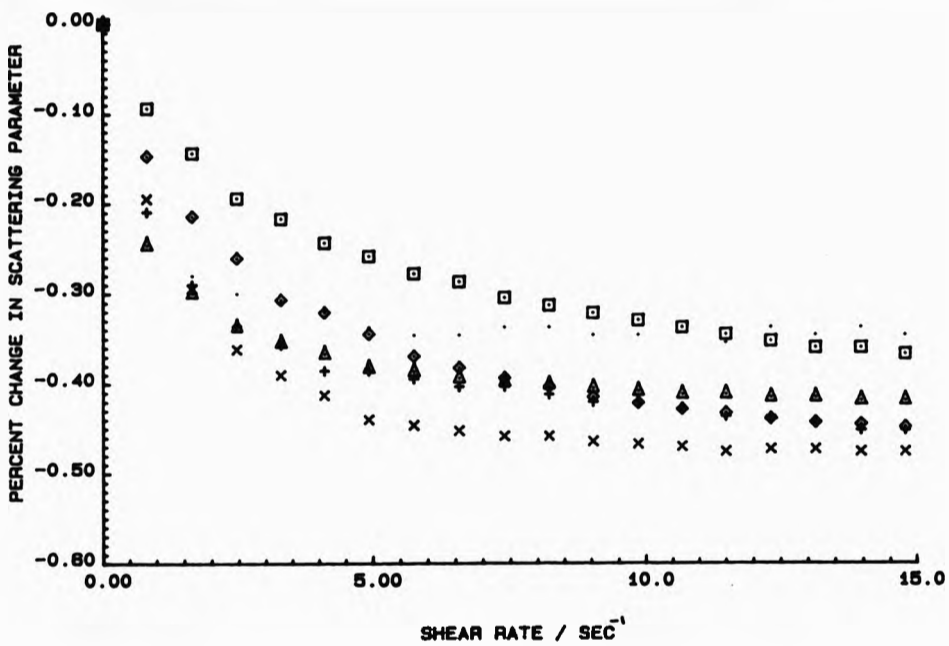


Fig (9.3.15)

Percentage change in scattering parameter as a function of shear rate. Fractionated kaolinite clay samples. Measured using azimuthal fibres, 1,2,3 and 4. Upright crosses = 5-6, diagonal crosses = 3-4, triangles = 2-3, diamonds = 0.7-0.8, squares = 0.4-0.5, points = 1-2 (μm). Wavelength = 589 nm, $\nu = 0.024$.

It can be seen from fig (9.3.15) that as the particle size increases the rate of change of scattering parameter with shear rate increases. This is to be expected: if the particle size increases so the Peclet number and the degree of particle orientation increases for any given shear rate. The shear rate necessary to completely align the particles was observed to decrease with increasing particle size. The effective scattering parameter at maximum alignment as a function of particle size is

illustrated in fig (9.3.16).

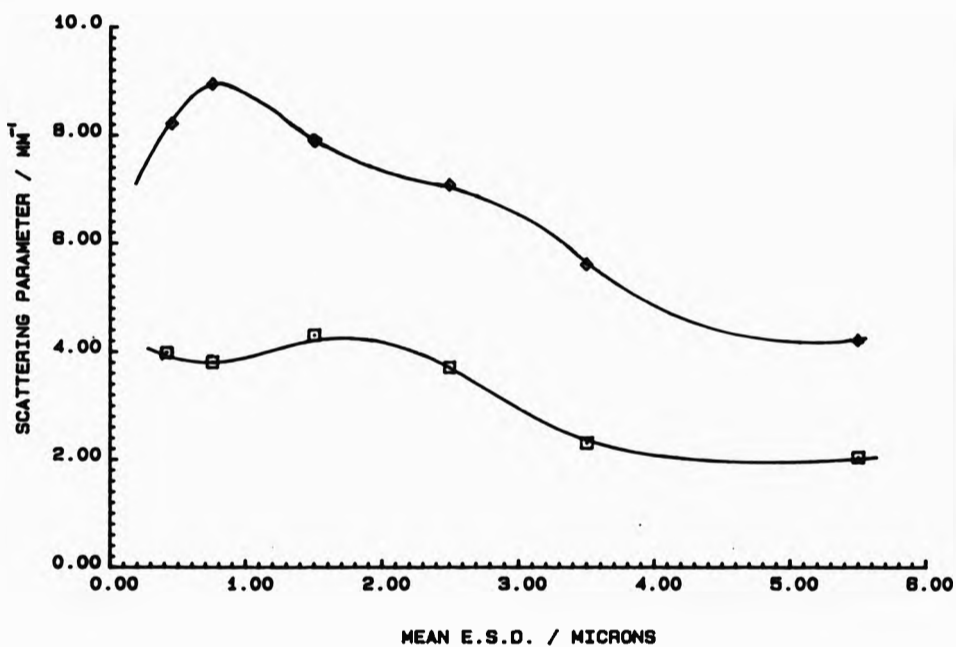


Fig (9.3.16)
Scattering parameter of aligned, (measured using azimuthal fibres) and unaligned kaolinite clay samples. Wavelength = 589 nm. Volume fraction = 0.024. Squares = aligned sample, diamonds = unaligned sample.

The non-aligned measurements of S were carried out using the single optical fibre bundle method detailed in chapter 5. For both aligned and non-aligned measurements of S the value quoted is the mean result from four experiments on the same sample.

Champion, Meeten and Moon [59] measured the scattering cross-section of fractionated kaolinite clay samples subject to laminar shear flow using very dilute suspensions where single

optical scattering was predominant. Measurements of the scattering cross-section were carried out parallel to the velocity gradient, (i.e. along the Z-axis), orthogonal to the measurements carried out above. Their results are reproduced in fig (9.3.17).

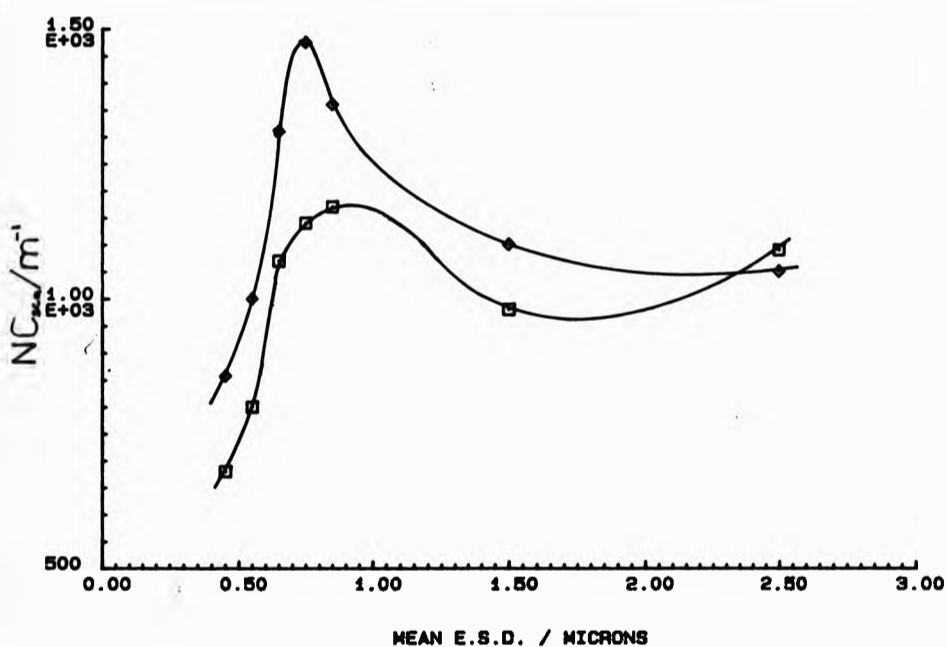


Fig (9.3.17)
Measured values of NC_{sca} of aligned and non-aligned fractionated kaolinite clay samples. Wavelength = 546 nm. Squares = aligned sample, diamonds = unaligned. Concentration = 1 kg m^{-3} . Reproduced from Champion et al. [59].

Comparisons of figs (9.3.16) and (9.3.17) show good qualitative agreement for the unsheared measurements of C_{sca} and S . Recalling that,

$$S = \frac{3}{4}NC_{sca}(1 - \overline{\cos\theta}),$$

it can be concluded that the effect of the $(1 - \overline{\cos\theta})$ term in the

above equation is to smooth out the peaks illustrated in the single scattering experiment, fig (9.3.17).

It is important when comparing the sheared sample results between these experiments to remember that the results are from orthogonal observations of the sheared sample, i.e. the single scattering measurements were made for light travelling parallel to the velocity gradient, (hence when aligned, faces of the particles were observed), and the multiple scattering measurements, (from the azimuthal fibres) were made orthogonal to the velocity gradient, parallel to the velocity vector, (hence when aligned, edges of the particles were observed). Hence, a decrease in C_{scat} observed in the single scattering experiment due to particle orientation changing from random to face-on, would correspond to an increase in C_{scat} in the (orthogonal) multiple scattering experiment as the particle orientation would change from random to edge-on.

For samples of e.s.d. less than 2 microns the measured values of C_{scat} decrease on shear in the single scattering experiment, hence the value of C_{scat} must increase in the (orthogonal) multiple scattering experiment. In fact, a decrease in S , (which is proportional to NC_{scat}), is observed. It can be concluded from this that there is a larger compensatory decrease in the factor $(1 - \overline{\cos\theta})$ in the multiple scattering experiment, (i.e. an increase in $\overline{\cos\theta}$), as the particles orientation changes from random to edge-on. Hence, $\overline{\cos\theta}$ for edge-on particles must be greater than $\overline{\cos\theta}$ for face-on particles, i.e. edge-on particles scatter light more strongly in the forward direction than face-on.

It is possible to obtain an estimate of $\overline{\cos\theta}$ for non-spherical particles using Rayleigh-Gans scattering theory [3]. It is an assumption of Rayleigh-Gans theory that;

$$2kr|m-1| \ll 1.$$

Where; k = the wave number of the illuminating radiation, $= 2\pi n/\lambda$,
 r = characteristic dimension of the particle,
 n = relative refractive index of the particle.

Although this means that this method is not completely accurate over the particle size range of interest, no other tractable approximation exists. From Rayleigh-Gans theory [3] the scattered intensity I , at a distance r from a scattering particle is;

$$I(\theta, \phi) = \frac{L k^4 \alpha^2 (1 + \cos\theta)}{2r^2} R^2(\theta, \phi) \quad \dots(9.3.1)$$

Where; k = the wave number of the illuminating radiation in the medium,
 α = the polarisability of the scattering particle,
 I = the intensity incident upon the particle,
 θ = the scattering angle and
 ϕ = the azimuth angle.

The function $R(\theta, \phi)$, for cylinders of finite length l and radius a , is given by the expression [3],

$$R(\theta, \phi) = F(u)E(s),$$

where, $F(u) = \frac{2}{u} J_1(u)$ and $u = (2kasin(\theta/2)sin\beta)$,
and $E(s) = \left(\frac{\pi}{2s}\right)^{1/2} J_{1/2}(s)$ and $s = (klsin(\theta/2)cos\beta)$.

Where $J_n(u)$ is the spherical Bessel function of order n , and the angle β is given by the expression,

$$\cos\beta = -\cos\zeta\sin(\theta/2) + \sin\zeta\cos(\theta/2)\cos\phi,$$

where ζ = the angle between the direction of propagation of the incident light and the cylinder axis normal, i.e. when the particle is face-on to the incident light $\zeta = 0^\circ$, and when the particle is edge-on to the incident light $\zeta = 90^\circ$.

The asymmetry parameter $\overline{\cos\theta}$ is given by the expression [14],

$$\overline{\cos\theta} = \frac{\int_0^\pi \int_0^\pi I(\theta, \phi) \sin\theta \cos\theta d\theta d\phi}{\int_0^\pi \int_0^\pi I(\theta, \phi) \sin\theta d\theta d\phi} \quad \dots(9.3.2)$$

Hence from (9.3.1),

$$\overline{\cos\theta} = \frac{\int_0^\pi \int_0^\pi (1 + \cos^2\theta) R^2(\theta, \phi) \sin\theta \cos\theta d\theta d\phi}{\int_0^\pi \int_0^\pi (1 + \cos^2\theta) R^2(\theta, \phi) \sin\theta d\theta d\phi} \quad \dots(9.3.3)$$

A BBC Basic programme was written to run on a BBC model B microcomputer to evaluate $\overline{\cos\theta}$ from equation (9.3.3), the programme coding is given in appendix III. The integral was evaluated numerically using the trapezium rule with angular steps of 0.01 radians for both θ and ϕ . For face on illumination it was not necessary to evaluate the integrals over all ϕ , as the scattering is spherically symmetrical. The functions $J_1(x)$ and $J_{1/2}(x)$ were evaluated using polynomial expressions from Abramowitz and Stegun [39].

Fig (9.3.18) illustrates values of $\overline{\cos\theta}$ as calculated by the programme given in appendix III, for both face-on and edge-on kaolinite particles, (compare with fig (2.2.3), $\overline{\cos\theta}$ for spherical

particles). Values of $\overline{\cos\theta}$ are illustrated for particle diameters up to 2.5 microns, above 2.5 microns the calculated values of $\overline{\cos\theta}$ were observed to oscillate for the face-on particles, but this size was outside of the present range of interest.

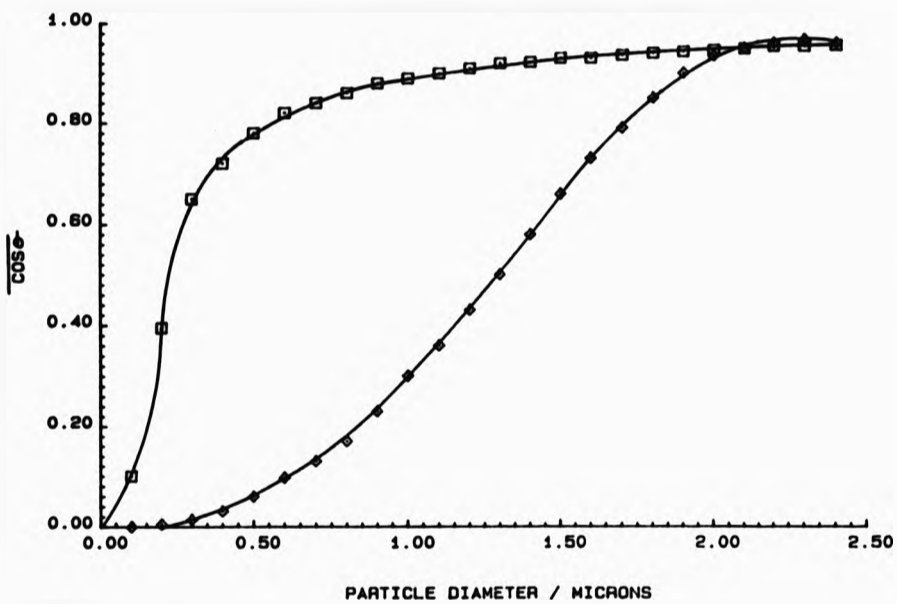


Fig (9.3.18)
 $\overline{\cos\theta}$ as a function of particle size for edge-on (squares) and face-on (diamonds) kaolinite particles with an axis ratio of 10:1. Wavelength = 589 nm.

It can be seen from fig (9.3.18) that $\overline{\cos\theta}$ for edge-on kaolinite particles is always greater than $\overline{\cos\theta}$ for face-on particles, in good qualitative agreement with the experimental results.

It is possible to calculate the scattering efficiency of

arbitrarily shaped particles using anomalous diffraction theory [3]. It has been shown by single scattering measurements that anomalous diffraction theory is in good agreement with experimentally determined scattering efficiencies for unaligned kaolinite particles [59]. Scattering efficiencies were calculated from anomalous diffraction theory (using the programme listed in appendix IV), for edge-on and face-on kaolinite particles. It was therefore possible, (using the previously calculated values of $\overline{\cos^2 \theta}$), to calculate scattering parameters of face-on and edge-on kaolinite particles. A scattering parameter for randomly orientated particles was estimated using a weighted mean of the scattering parameters for face-on and edge-on particles, (it was assumed that random orientation could be represented by 2 edge-on particles per face-on particle). Fig (9.3.19) illustrates the scattering parameters of randomly orientated and edge-on kaolinite particles so calculated.

It can be seen from a comparison of figs (9.3.16) and (9.3.19) that there is reasonable qualitative agreement between the theoretical and experimental results. The peak in scattering parameter observed experimentally for the unaligned 0.7-0.8 micron e.s.d. sample is predicted by the theoretical curve. However, the theoretical curve shows the scattering parameter dropping quickly with particle size above a particle diameter of 0.8 microns, for both aligned and non-aligned samples. A much slower drop in scattering parameter is observed in the experimental results. This discrepancy is possibly due to inaccuracies in Rayleigh-Gans theory generated by calculating

values of $\overline{\cos\theta}$ outside of the range of strict validity of the theory. It may also be due to the large polydispersity of face diameters in the samples, this would tend to decrease the slopes in fig (9.3.19).

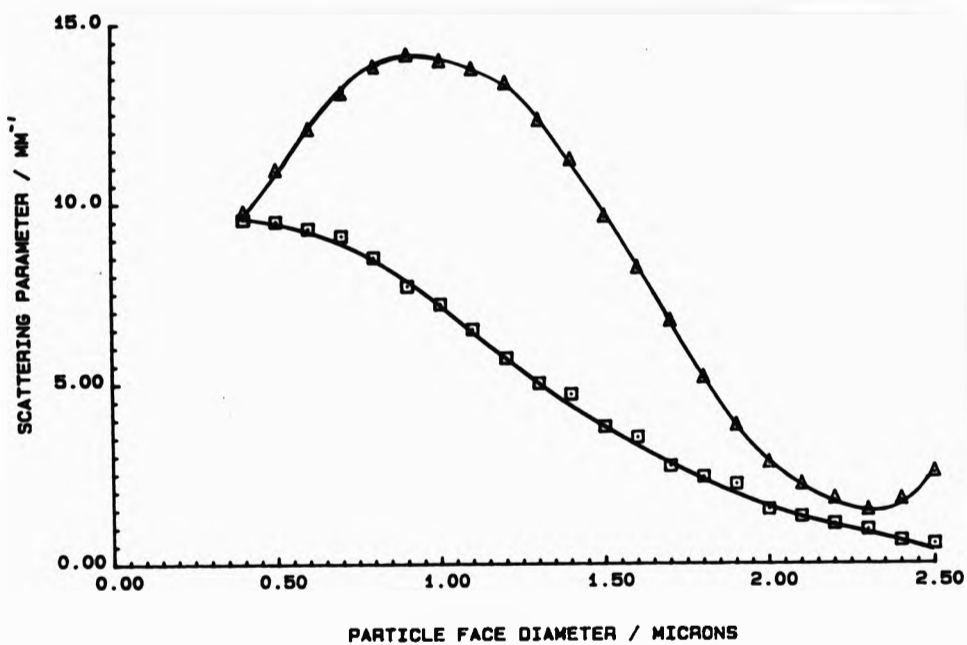



Fig (9.3.19)
Theoretically computed scattering parameters of randomly orientated (squares) and edge-on (diamonds) kaolinite particles. Wavelength = 589 nm. Volume fraction = 0.024.

The calculated scattering parameters illustrated in fig (9.3.19) are highly dependent upon the assumed mean axis ratio of the kaolinite particles. An axis ratio of 10:1 has been assumed here, however mean axis ratios as low as 7.7 and as high as 12 have been reported [63].

(9.3.5) Conclusion.

It has been shown that single optical fibres, mounted in a flow channel, may be used to measure rheo-optical effects arising from particle orientation in concentrated colloidal dispersions. It has also been shown that, for optical fibres mounted in the same plane and facing in the same direction, with a lateral separation d , the detected flux is dominantly transmitted through the sample so long as the product $Sd > 1.7$. The percentage change in the observed intensity has been shown to be dependent upon the fibre separation d , changes in intensity on flow orientation of the particles of up to 700 % being recorded. The change in the scattering parameter experienced by the detected flux has been shown to be independent of d , (so long as in varying d the range of shear rates over which S is measured remains unaltered). This makes such an optical fibre geometry a convenient method of measuring rheologically induced changes in the scattering parameter of colloidal samples.

It has been shown that the change in scattering parameter on flowing colloidal kaolinite samples is independent of volume fraction between volume fractions of 0.03 and 0.30 for observations both parallel and normal to the applied velocity gradient. It has been shown that the state of flocculation of a flowing kaolinite dispersion may be accurately monitored using optical fibres. The results obtained for the flocculation pH dependence are in reasonable agreement with those obtained by Molloy [9]



using ultrasonic orientation of particles. It has also been shown that the Dispex dose for maximum particle deflocculation determined optically is in good agreement with previous measurements based on dispersion viscosity.

A simple model of particle orientation has been shown to be capable of predicting the change in scattering parameter observed. It has been shown that the onset of Taylor vortex flow in the concentric cylinder system may be accurately determined, and that the experimentally observed shear rate necessary to induce Taylor vortex flow is in reasonable agreement with hydrodynamic theory. In addition it has been shown experimentally that kaolinite particles scatter light more strongly in the forward direction when viewed edge-on than when viewed face-on. This is in good agreement with Rayleigh-Gans scattering theory. It has also been shown that, by a combination of anomalous diffraction theory and Rayleigh-Gans theory, the scattering parameters of both aligned and non-aligned kaolinite samples, (and in particular the sign of the changes in the multiple scattering parameter caused by shear flow), may be understood.

CHAPTER 10: DISCUSSION AND CONCLUSIONS.

This chapter is intended to provide a brief summary of the results, conclusions and structure of the investigation. In addition the practical applications of this work will be considered.

(10.1) Overview of investigation.

The aim of this work has been to investigate the use of optical fibres for measuring the diffuse reflectance of concentrated colloidal dispersions, and hence extract useful information about the dispersion. The structure of the investigation has been directed to bridge the two extremes between (relatively) well theoretically characterized systems, (monodisperse, spherical, well stabilised samples), and systems of more practical usefulness, (polydisperse, non-spherical samples), which are not as well defined theoretically.

The initial work in this investigation is concerned with validating the use of optical fibres to measure multiple light scattering parameters in densely scattering colloidal samples. Two problems were evident at this point;

- (i) how to extract information on the multiple scattering parameters from the samples, and
- (ii) how to assess the accuracy of the results so extracted.

Problem (i) at first sight would appear to be relatively

straightforward. The reflectance of a multiple scattering sample is dependent upon the samples multiple scattering parameters. Hence, measurements of the samples reflectance, (as a function of sample thickness above an absorbing boundary), will give a measurement of the multiple scattering parameters. However, analyzing the reflectance data is far from straightforward. There are several multiple scattering theories with which the data may be analyzed. They range from the simplistic Kubelka-Munk theory [30], to the highly complex, but much more exact, radiative transport theory [36,38,43]. In general, the more complex the theory, the greater the number of parameters needed to describe the multiple scattering within the sample, but the greater the number of parameters, the better the 'fit' between experiment and theory. However, simply increasing the complexity of the theory (to increase the number of parameters, and hence improve the fit), is not the perfect solution: for any given experimental data set, increasing the number of parameters used to characterize that set will not only lead to a better 'fit', but also an increase in the errors on the values of the theoretical parameters determined from the 'fit'. This is particularly so for the monotonic experimental data sets obtained, (see figs (3.2.1), (3.2.2) and (3.5.1)). Hence there is a compromise between error due to non-exact fitting of theory, and error due to having a multitude of fitting parameters. Because of this fact the simplistic Kubelka-Munk theory, (which employs only two multiple scattering parameters S and K), was used to analyze the data. The Kubelka-Munk theory gave reasonable fits to the experimental data, see figs (5.1.3), (6.3.1) and (6.3.2). This does not mean that the more complex theories are redundant, and the more

exact radiative transfer theory is employed to explore the range of validity of the Kubelka-Munk theory in section (2.3.3). In section (2.3.7) photon diffusion, four-flux and radiative transfer theory are all used to explore the meaning of the Kubelka-Munk scattering coefficients. Finally in section (3.7.3) the effect of using non-diffuse illumination is analyzed by comparing Kubelka-Munk theory with four-flux theory.

Problem (ii), how to assess the accuracy of the multiple scattering measurements, is again less straightforward than it would at first appear. Standard calibration materials for multiple scattering from colloidal dispersions do not exist. However, for monodisperse spherical particle samples of moderate concentration (volume fraction v less than .05), optical effects due to close packing of particles are negligible, but multiple scattering is still predominant. Thus a theoretical value of the Kubelka-Munk scattering coefficient can be calculated from the single particle scattering parameters, see section (2.3.7). A further problem arises here in that little experimental work has been carried out to verify the multiple scattering theoretical results. Hence, discrepancies between the theoretical and experimentally determined values could arise either from errors in theory, or faults in the application of the optical fibre system. To overcome this problem the scattering parameters of monodisperse spherical latex samples at a volume fraction of 0.0238, for which the single scattering parameters may be calculated, were measured using various optical fibre geometries, (see chapters 3,4 and 5), and, as an independent check, using the classical integrating sphere

method, (see chapter 6). The agreement between the absolute values of S from theory, the integrating sphere method, (chapter 6) and the single optical fibre bundle and beam splitter method, (chapter 5), was good, (so long as internal interfacial reflections at the sample/window interface were taken into account, see section (3.7.4)), thus validating the theoretical calculation of S , and the single fibre bundle and beam-splitter method of measuring S . The other optical fibre methods for measuring S , (i.e. the bifurcated optical fibre bundle, and single optical fibre methods), could then have their performance checked using the theoretically calculated values of S .

Having validated the use of optical fibres to measure multiple scattering in spherical latex samples of relatively low volume fractions, the single optical fibre bundle method was employed to examine the agreement between theory and experiment for high volume fraction samples, (i.e. $v > 0.10$), where significant deviation has previously been noted from the linearity between S and v predicted by theory (see chapter 8).

Measurements of absorption in multiple scattering samples were also carried out using two optical fibre techniques, (chapter 7). A straight comparison between absorption measurements for multiple scattering and non-scattering samples allowed the performance of the two optical fibre methods employed to be assessed.

The second part of this investigation is concerned with non-spherical colloidal particles and the application of optical

fibres to measuring flow induced changes in their scattering parameters. Due to the nature of the investigation it is necessary to use non-spherical particles. Kaolinite clay suspensions were used for the majority of this investigation. The kaolinite particles have a low optical absorption, (maximizing transmission of light) and a flat plate-like shape of high aspect ratio, (maximizing their Peclet number). In addition to this the rheology and stability of kaolinite clays is well documented. Highly polydisperse kaolinite samples were provided in large quantities by English China Clays International, a small quantity of more monodisperse samples was also provided. Exact single scattering theoretical results do not exist for kaolinite particles, however approximate scattering theories were applied to the samples with some measure of success, see section (9.3.4). The application of a simple multiple-scattering theory is also prohibited due to the highly anisotropic scattering and light propagation through the samples. The analysis of the optical fibre methods is therefore, by necessity, highly empirical for use with flowing kaolinite suspensions. The optical response of the various shear flow systems was therefore assessed using the monodisperse spherical latex samples. The rheo-optical data obtained with kaolinite samples was then interpreted using this data.

(10.2) Conclusions.

(10.2.1) Spherical and randomly orientated particles.

It has been shown that a bifurcated optical fibre bundle can be used to measure the diffuse reflectance of a purely scattering sample as a function of sample thickness and, by analysis of these results, a measure of the scattering parameter S of the sample may be obtained. By use of well characterized samples, (monodisperse spherical latex particles suspended in water), it has been shown that the particle size and concentration dependence, (for $v < .025$), of S predicted theoretically are accurately reflected in the experimental results. However, the absolute experimental values of S were not in agreement with the absolute theoretically predicted values, i.e. there was a constant factor, (independent of both particle size and sample concentration), relating the two values of S . It was shown experimentally, by the use of single optical fibres, that the discrepancy between absolute experimental and theoretical values of S was due to the finite separation between the optical influx and efflux routes within the sample, and this discrepancy was shown to be resolvable by use of a single optical fibre bundle.

The application of optical fibres to illuminate the sample where the incident flux is partially diffuse was investigated by comparing the predictions of Kubelka-Munk two-flux theory with the four-flux theory. Provided that reflected intensity data was obtained up to sufficient optical thicknesses Sd , (where d is the

thickness of the reflecting sample), the use of imperfectly diffuse illumination was shown to have only a small effect on the measured value of S . E.g. for $Sd > 5$, the error introduced by using imperfectly diffuse illumination was less than 4%. It was also shown theoretically that for the bifurcated optical fibre bundle the corrections to S which allow for internal specular reflection at the sample/fibre interface are small, approximately 3%. This compares with the correction of approximately 60% necessary in the integrating sphere method of obtaining S . This illustrates a major advantage of the optical fibre method, as neglecting the often unknown interfacial specular reflections leads to only small errors in the measured value of S . In the integrating sphere method the interfacial corrections are large and are often impossible to calculate accurately without knowledge of the sample refractive index.

The validity of the two-flux Kubelka-Munk theory was also investigated by comparison with the radiative transfer theory. It was shown (section (2.3.4)) that only if the optical thickness of the sample was small would large errors occur when applying Kubelka-Munk theory to the sample to obtain values of S . E.g. for $Sd < 0.5$, error in $S > 30\%$. However, if the reflectance of the sample is measured up to large optical thicknesses the error is much reduced, e.g. for $Sd > 4$ the error introduced by applying the Kubelka-Munk theory to calculate S is $< 5\%$. In this work all data was obtained up to values of $Sd > 5$.

Reflection measurements to obtain S were also carried

out, (chapter 6), using the classical integrating sphere method. Good agreement was noted between experiment and multiple scattering theory for the well characterized latex samples used, so long as the large interfacial specular reflections were taken into account. This validated the theoretical calculations of S, and the use of such calculations in assessing the performance of the optical fibre probes.

Measurements of the absorption coefficient K, within multiple scattering samples were also carried out using the single optical fibre bundle method, (chapter 7), but using both a white and black backing. In both cases the reflectance of the sample was monitored as a function of sample thickness. It was shown that when using the black backing an accurate measurement of K could not be obtained. However, by the use of a white backing K could be determined accurately, although with diminished accuracy in S.

The concentration dependence of the scattering parameter of both spherical latex and non-spherical kaolinite particles was investigated up to volume fractions of 0.38. The decrease in scattering efficiency per particle noted at high concentrations, ($v > .05$), was explained in terms of close packing of particles.

(10.2.2) Shear-orientated kaolinite particles.

It has been shown that single optical fibres may be used to measure flow-induced changes in the diffuse scattering of colloidal kaolinite dispersions. The optical fibre geometry outlined in

sections (9.2) and (9.3) is very sensitive to flow-induced changes in scattering parameter. Changes in detected intensity of up to 700 % were recorded on flowing a sample, and these changes were explicable in terms of shear-induced particle orientation. The experiments detailed in sections (9.2.4) and (9.2.5) show that it is possible to measure sensitively the state of flocculation of a kaolinite sample using optical fibres. A simple model of shear-induced particle orientation has been shown to be capable of predicting the changes in scattering parameters observed on flow. Approximate scattering theories, i.e. Rayleigh-Gans and anomalous diffraction theory, were applied to the kaolinite dispersions. These enabled the scattering parameters of both aligned and non-aligned kaolinite particles, and in particular the signs of the flow induced changes in S, to be understood.

It has been shown that the optical fibre method can measure flow-orientational effects in non-spherical particle dispersions. Fair agreement is found between the experimental results and the approximate scattering theory that can be applied to such particles.

APPENDIX I.

CALCULATION OF MIE SCATTERING COEFFICIENTS.

(i) Introduction.

The programme coding owes a large debt to that of Bohren and Huffman [13]. The programme listing below is as coded into the computer, it should therefore be possible to execute the programme, (on a suitable machine), with no alterations. The double precision Fortran programme was executed on a VAX11/780 mainframe.

It is important to note that the programme listed below assumes that neither the particles nor the supporting medium is absorbing.

(ii) Mie scattering programme.

```
10      PROGRAM MIE
20      DOUBLE PRECISION Z,S,M,X,Y,REB(-1,300),IMB(-1,300)
30      DOUBLE PRECISION REA(0:300),REB(0:300)
40      DOUBLE PRECISION IMA(0:300),IMB(0:300),U,V,NB,NC,WB
50      DOUBLE PRECISION QSCA,QPR,QC,AV,RN,NN,N,A(0:300)
60      INTEGER NMX,NMAX
70
80
90
100     WRITE(6,100)
110     READ(5,110) X
120     WRITE(6,120) X
130     WRITE(6,140)
140     READ(5,110) M
150     WRITE(6,120) M
160
```

```

170
180
190      NMAX = X+4.0*(X**.333)+2.0
200      Y=M*X+1.0
210      NMX = NMAX+50
220
230
240
250      WRITE(6,150) NMX
260      NN=NMX-1
270      A(NMX)=0.0
280      DO 10, N=1, NN
290          RN=NMX-N+1
300          A(NMX-N)=1.0*(RN/Y)-(1.0/(RN/+A(NMX-N+1)))
310 10      CONTINUE
320
330
340
350      REB(-1)=DCOS(X)
360      IMB(-1)=-DSIN(X)
370      REB(0)=DSIN(X)
380      IMB(0)=DCOS(X)
390      DO 20, N=1, NMAX
400          REB(N)=((2.0*N-1.0)/X)*REB(N-1)-REB(N-2)
410          IMB(N)=(((2.0*N-1.0)/X)*IMB(N-1))-IMB(N-2)
420      CONTINUE
430
440
450
460      DO 30, N=1, NMAX
470          Z=1.0*A(N)/M+1.0*N/X
480          S=1.0*M*A(N)+1.0*N/X
490          U=(Z*IMB(N)-IMB(N-1))/(Z*REB(N)-REB(N-1))
500          V=(S*IMB(N)-IMB(N-1))/(S*REB(N)-REB(N-1))
510          REA(N)=1.0/(1.0+U**2.0)
520          REB(N)=1.0/(1.0+V**2.0)
530          IMA(N)=-1.0/(1.0/U+U)
540          IMB(N)=-1.0/(1.0/V+V)
550 30      CONTINUE
560
570
580
590      WRITE(6,210)
600      QSCA=0.0
610      DO 40, N=1, NMAX
620          QSCA=QSCA+(2.0*N+1.0)*(REA(N)+REB(N))
630      CONTINUE
640
650
660
670      WB=0
680      DO 50, N=1, (NMAX-1)
690          NB=1.0*N*(N+2.0)/(N+1.0)
700          NC=1.0*(2.0*N+1.0)/(N*(N+1.0))
710          WB=WB+1.0*NB*(REA(N)*REA(N+1)+IMA(N)*IMA(N+1))
720          WB=WB+1.0*NB*(REB(N)*REB(N+1)+IMB(N)*IMB(N+1))

```

```

730          WB=WB+1.0*NC*(REA(N)*REB(N)+IMA(N)*IMB(N))
740 50      CONTINUE
750
760
770
780          QSCA=2.0/(X**2.0)*QSCA
790          QC=4.0/(X**2.0)*WB
800          QPR=QSCA-QC
810          AV=QC/QSCA
820          WRITE(6,250) QSCA,AV
830          WRITE(6,260) QD
840
850
860
870 100     FORMAT(1X,'INPUT X')
880 110     FORMAT(D21.15)
890 120     FORMAT(D21.15)
900 140     FORMAT(1X,'INPUT M')
910 150     FORMAT(I5)
920 210     FORMAT('          ')
930 250     FORMAT(' QSCA= ',D21.15,' COS= ',D21.15)
940 260     FORMAT(' QPR= ',D21.15)
950
960
970
980          END

```

(111) Definition of variables.

Variable	Definition
REA(n)	One dimensional array, used to store the real part of a_n . For any value of n , the value of $\text{Re}\{a_n\}$ is stored in REA(n).
IMA(n)	One dimensional array, used to store the imaginary part of a_n . For any value of n , the value of $\text{Im}\{a_n\}$ is stored in IMA(n).

REB(n) One dimensional array, used to store the real part of b_n . For any value of n , the value of $\text{Re}\{b_n\}$ is stored in REB(n).

IMB(n) One dimensional array, used to store the imaginary part of b_n . For any value of n , the value of $\text{Im}\{b_n\}$ is stored in IMB(n).

REB(n) One dimensional array, used to store the real part of ζ_n . For any value of n , the value of $\text{Re}\{\zeta_n\}$ is stored in REB(n).

IMB(n) One dimensional array, used to store the imaginary part of ζ_n . For any value of n , the value of $\text{Im}\{\zeta_n\}$ is stored in IMB(n).

A(n) One dimensional variable, used to store the value of A_n . For any value of n the value of is stored in A(n).

X Size parameter x , ($x = 2wa/\lambda$).

M Relative refractive index m , ($m = n_1 / n_2$).

Y $Y = mx$

NMAX Integer variable, represents the limit for the summations and upward recurrence

relations.

NMX	Integer variable, represents the starting point for calculating the downward recurrence relation to calculate $\{ \}$.
U,V,NB,NC, Z,S,WB,NN,RN	Variables used to store intermediate results of numerical calculations.
N,NN,RN	Incremental variables used in DO...CONTINUE loops.
QSCA	Mie scattering coefficient Q_{SCA} .
QPR	Mie scattering coefficient Q_{PR} .
QD	Product of coefficients $Q_{SCA} \overline{\cos\theta}$.
AV	Mie scattering coefficient $\overline{\cos\theta}$.

NOTE. All variables are double precision unless otherwise stated.

(iv) Programme algorithm.

Lines.	Function.
10 - 60	Initialization of variables. Note all non-integer

variables are defined as being double precision, i.e. they all have 16 significant figures. This is necessary to reduce rounding errors that may become magnified in the recurrence relationships.

- 100 - 150 Requests input of the size parameter x , and the relative refractive index m . Input is echoed on screen.
- 190 Calculate required number of terms for convergence. Note if the number of terms for convergence is greatly exceeded, the accuracy of the programme may be greatly affected by rounding errors in the recurrence relations.
- 200 Calculate y , $y=mx$.
- 210 Calculate the starting point ($n=NMX$), for estimation of $A_n(y)$, by a downward recurrence relation.
- 250 - 310 Calculate $A_n(y)$ for $0 < n < NMX$. Store results in one dimensional array, $A(n)$.
- 350 - 420 Calculate real and imaginary parts of ζ_n by upward recurrence for $0 < n < NMax$. Store the results in two one dimensional arrays, $REB(n)$ and $IMB(n)$.

- 460 - 550 Calculate real and imaginary parts of a_n and b_n , for $0 < n < NMAX$, using the calculated values of $An(\gamma)$, and $\sum_n(\gamma)$. Store in four one dimensional arrays, REA(n), IMA(n), REB(n) and IMB(n).
- 590 - 630 Evaluate series summation necessary to calculate Q_{sca} , i.e. $\sum_n (2n+1)(RE[a_n] + RE[b_n])$.
- 670 - 740 Evaluate series summation necessary to calculate $Q_{sca} \cdot \overline{\cos\theta}$, i.e. $\sum_n n(n+2)/(n+1) \cdot (RE[a_n a_{n+1}] + RE[b_n b_{n+1}]) + (2n+1)/(n(n+1)) \cdot (RE[a_n b_n])$.
- 780 - 810 Calculate Q_{sca} and $Q_{sca} \cdot \overline{\cos\theta}$ from results of series summations. Hence calculate $\overline{\cos\theta}$ and Q_{pr} .
- 820 - 830 Output Q_{sca} , $\overline{\cos\theta}$ and Q_{pr} .

(v) Validation of Programme.

The values of Q_{sca} , Q_{pr} and $\overline{\cos\theta}$ calculated by the programme were initially compared with the tabulated values of Wickramasinghe [14]. Wickramasinghe gives tabulated values of Q_{sca} , Q_{pr} and $\overline{\cos\theta}$ (for both absorbing and non-absorbing spheres), for values of m ranging from 1.1 to 2.0 and values of x ranging from 0.1-(.1)-5.0, 5.0-(.2)-15.0. It was noted that excellent agreement was obtained (better than 1 %) for Q_{sca} . However large discrepancies were observed between the tabulated and computed values of Q_{pr} and $\overline{\cos\theta}$. It was

first assumed that the programme was at fault, however careful checking revealed no coding or theoretical error in the programme. No previous reports of errors in Wickramasinghe's tabulated values have been discovered. Comparisons of values of $\overline{\cos\theta}$ and Q_r were then made with those of other authors. These were; Blevin and Brown [15], Brinkworth [16], Irvine [17,18], Mehta [19]. In all cases excellent agreement was noted. In those cases where tabulated results (as opposed to graphical results) were presented, the agreement between the tabulated and computed results was better than 1%. For the graphical results, agreement was well within the limits imposed by estimating values of $\overline{\cos\theta}$ and Q_r from the graphs. The values of m within the published values ranged from 1.2 to 2.4 and the values of x ranged from 0.2 to 30. It was therefore concluded that the programme was correct in predicting values of Q_{ms} , Q_r and $\overline{\cos\theta}$ between values of m of between 1.2 and 2.0, and values of x between 0.2 and 30.

APPENDIX II: INTERNAL DIFFUSE REFLECTANCE OF A WINDOW.

(1) Theory.

The incident flux density H_0 at an interface can be calculated from I_0 , the radiance, by the radiance-to-flux equation [47],

$$H_0 = \int_0^{2\pi} I_0 \cos \eta d\omega, \quad \dots(1)$$

where; η = the angle made by I with the surface normal,
 ω = solid angle.

Now,

$$d\omega = 2\pi \sin \eta d\eta,$$

therefore

$$H_0 = \pi I_0. \quad \dots(11)$$

The diffusely reflected flux density H at the interface is given by the expression;

$$H = \int_0^{2\pi} R I_0 \cos \eta d\omega, \quad \dots(111)$$

where R is the specular reflectance of the interface, (a function of η).

R may be calculated for incident unpolarised irradiance from equation [47],

$$R = 1/2(|r_p| + |r_s|),$$

where r_p and r_s are the Fresnel field-reflectance coefficients for the electric vector polarised parallel and normal, (respectively), to the plane of incidence. For non-absorbing media the standard results are [49];

$$r_p = \frac{\tan(\eta_a - \eta_b)}{\tan(\eta_a + \eta_b)} \quad \text{for } n_a \sin \eta_a < 1, \quad n_b$$

$$r_p = 1 \quad \text{for } n_a \sin \eta_a > 1, \quad n_b$$

$$r_s = \frac{\sin(\eta_a - \eta_b)}{\sin(\eta_a + \eta_b)} \quad \text{for } n_a \sin \eta_a < 1, \quad n_b$$

$$\text{and } r_s = 1 \quad \text{for } n_a \sin \eta_a > 1, \quad n_b$$

Where; n_a = the refractive index of medium 1,
 n_b = the refractive index of medium 2,
 η_a = the angle of incidence,
 η_b = the angle of refraction.

Combining equations (ii) and (iii) yields,

$$H = \int_{\omega=0}^{\omega=2\pi} (|r_p|^2 + |r_s|^2) \cos \eta \sin \eta d\eta,$$

The diffuse reflectance \bar{R} of the surface is given by,

$$\bar{R} = H/H_0,$$

hence,

$$\bar{R} = \frac{1}{\pi} \int_{\omega=0}^{\omega=2\pi} (|r_p|^2 + |r_s|^2) \cos \eta \sin \eta d\eta. \quad \dots (iv)$$

This integral cannot be evaluated directly due to the nature of r_p and r_s , numerical solutions must be used to evaluate \bar{R} .

A BBC Basic programme was written to estimate \bar{R} from equation (iv). The programme was run on a BBC model B microcomputer and evaluated the integral (using the trapezium rule), over the range $0 < \eta < \pi/2$ in steps of 0.01 radians.

(ii) Programme coding.

```
5 H = 0
10 MODE 7
20 @% = &203004
30 CLS
40 PRINT "REFRACTIVE INDEX MEDIUM 1 = ": INPUT N1
50 PRINT "REFRACTIVE INDEX MEDIUM 2 = ": INPUT N2
60
70
80 FOR iangle = 0.01 TO PI/2 STEP .01
90 IF (N1*SIN(iangle)/N2) >= 1 THEN PROCONE
100 IF (N1*SIN(iangle)/N2) < 1 THEN PROCTWO
110 PRINT TAB(1);(iangle/PI*180);TAB(9);(rangle/PI*180);
    TAB(17);Rp;TAB(25);Rs
120 H = H + ((ABS(Rp)*ABS(Rp))+(ABS(Rs)*ABS(Rs)))*PI*
    COS(iangle)*SIN(iangle)
130 NEXT iangle
140 H = H*.01/PI
150 PRINT H
160 STOP
170
180
190 DEFPROCONE
200 rangle = PI/2
210 Rp = 1: Rs = 1
220 ENDPROC
230
240
250 DEFPROCTWO
260 rangle = ASN(N1*SIN(iangle)/N2)
270 Rp = (TAN(iangle - rangle))/(TAN(iangle + rangle))
280 Rs = (SIN(iangle - rangle))/(SIN(iangle + rangle))
290 ENDPROC
```

(iii) Results.

The programme was tested against published results [32,47] and was found to agree to within 2 % of the published values.

To calculate the reflectance of the sample/bifurcated optical fibre bundle interface it is necessary to evaluate R for the core, cladding and epoxy resin separately. The core, cladding and epoxy resin have refractive indices 1.56, 1.46 and 1.58 respectively and

relative areas 14:76:10. The sample refractive index is a function of the sample concentration, however for low volume fractions the refractive index of the sample will be close to that of water, i.e. 1.333. Assuming a sample refractive index of 1.333 the following reflectances were calculated by the programme;

sample to core,	R = 0.039,
sample to cladding,	R = 0.024,
sample to epoxy,	R = 0.042.

The reflectance of the fibre bundle interface is therefore;

$$\bar{R} = (.14*0.039) + (.76*0.024) + (.10*0.042).$$
$$= 0.0279.$$

Hence approximately 3 % of the diffuse flux incident upon the fibre bundle face would be reflected back into the sample.

The corresponding reflectance for a sample to glass interface, (such as is used in the integrating sphere), is 0.598, i.e. approximately 60 % of the diffuse flux incident upon the glass slide is reflected back into the sample.

Neither of these calculated interfacial reflections varies by more than 10 % for changes in sample refractive index of +/- 0.05.

APPENDIX III: CALCULATION OF ASYMMETRY PARAMETER OF
KAOLINITE PARTICLES FROM RAYLEIGH-GANS THEORY.

(1) Theory.

Rayleigh-Gans theory [3] gives the scattered intensity I , at a distance r from the scattering particle;

$$I(\theta, \phi) = \frac{I_0 k^4 a^3 (1 + \cos^2 \theta) R^2(\theta, \phi)}{2r^4} \dots (1)$$

Where; k = the wave number of the illuminating radiation in the medium,

a = the polarisability of the scattering particle,

I_0 = the intensity incident upon the particle,

θ = the scattering angle,

ϕ = the azimuth angle.

The asymmetry parameter g ($= \overline{\cos \theta}$), is defined by the expression [13],

$$\overline{\cos \theta} = \frac{\int_0^\pi \int_0^{2\pi} I(\theta, \phi) \sin \theta \cos \theta d\theta d\phi}{\int_0^\pi \int_0^{2\pi} I(\theta, \phi) \sin \theta d\theta d\phi}$$

Hence from (1),

$$\overline{\cos \theta} = \frac{\int_0^\pi \int_0^{2\pi} (1 + \cos^2 \theta) R^2(\theta, \phi) \sin \theta \cos \theta d\theta d\phi}{\int_0^\pi \int_0^{2\pi} (1 + \cos^2 \theta) R^2(\theta, \phi) \sin \theta d\theta d\phi} \dots (11)$$

The function $R(\theta, \phi)$ is known for finite cylinders [3], (see section (9.3.4)), and hence the asymmetry parameter may be calculated by evaluating expression (11).

A BBC Basic programme was written to run on a BBC model B microcomputer to evaluate expression (11). The integrals were evaluated using the trapezium rule over angular steps of 0.01 radians for both θ and ϕ .

(11) Programme coding.

```

10 MODE 3
20 stp1 = 0.1: stp2 = 0.1
30 PRINT:PRINT
40 PRINT "EDGE OR FACE ON ? (E/F) ":Q = GET: IF Q = 69 THEN FC = 0
   ELSE FC = 1
50 PRINT:PRINT
60 IF FC = 1 THEN PRINT; "FACE ON CALC. OF <COS>" ELSE PRINT;
   "EDGE ON CALC. OF <COS>"
70 PRINT:PRINT "INPUT CYL. PARTICLE DIAMETER (MICRONS) "; INPUT D
80 D = D*1E-6:A=D/2*L=D/10
90 PRINT:PRINT
100 NUM=0:DEN=0
110 WV=589E-9:K=2*PI*1.333/WV
120 IF FC = 1 THEN GOTO 140
130 FOR Th1 = 0.00001 TO 2*PI STEP stp1
140   FOR Theta = 0.00001 TO PI STEP stp2
150     IF FC=1 THEN BETA = ACS(-SIN(Theta/2)) ELSE
       BETA = ACS(COS(Theta/2)*COS(Th1))
160     Z = 2*K*A*SIN(Theta/2)*SIN(BETA)
170     T = K*L*SIN(Theta/2)*COS(BETA)
180     PROCJ1N
190     PROCJHLFN
200     F=J1N*2/Z
210     E=JHLFN
220     Int=(1+COS(Theta)*COS(Theta))*F*F+E*E
230     NUM=NUM+Int*COS(Theta)*SIN(Theta)
240     DEN=DEN+Int*SIN(Theta)
250   NEXT Theta
260   IF FC=1 THEN GOTO 280
270 NEXT Th1
280 CS=NUM/DEN
290 PRINT; "DIAMETER (MICRONS) = ";D*1E6:PRINT;"<COS> = ";CS
300 GOTO 30
310
320 DEFPROCJ1N
330 IF Z<-3 THEN PRINT "ERROR IN J1N"
340 IF Z>3 THEN GOTO 390
350 Z1=Z/3
360 J1N=.5-.56249985*Z1^2+.2109357*Z1^4-.03954289*Z1^6+
   .00443319*Z1^8-.000317*Z1^10
370 J1N=J1N*Z
380 GOTO 430

```

```

390 Z2=1/Z1
400 F1=.79788456+.00000156*Z2+.01659667*Z2^2+.00017105*Z2^3-
      .00249511*Z2^4+.00113653*Z2^5-.00020033*Z2^6
410 Th1=Z-2.35619449+.12499612*Z2+.00005650*Z2^2-.00637879*Z2^3
      -.00074348*Z2^4+.00079824*Z2^5-.00029166*Z2^6
420 J1N=1/(SQR(Z))*F1*COS(Th1)
430 ENDPROC
440
450 DEFPROCJHLFN
460 JHLFN=SIN(T)/T
470 ENDPROC

```

(iii) Accuracy of programme.

The programme was executed with decreasing angular step sizes (line 20), to increase the accuracy of the integral approximation. It was found that if the step size was decreased by a factor of 10 (to 0.01 radians) the calculated values of $\overline{\cos\theta}$ altered by approximately 5 %. Decreasing the step size by a further factor of 10 produced changes in the calculated value of $\overline{\cos\theta}$ of less than 1 %. It was therefore concluded that the programme was accurate to within approximately 6 % for an angular step size of 0.1 radians. This was considered to be adequate considering the high degree of polydispersity of the samples.

APPENDIX IV: CALCULATION OF SCATTERING CROSS-SECTION OF
KAOLINITE PARTICLES FROM ANOMALOUS DIFFRACTION THEORY.

(1) Theory.

Anomalous diffraction theory [3] assumes that optical rays incident upon a particle traverse the particle without reflection or refraction. Scattering from the particle is assumed to arise solely from a phase shift due to the path length traversed by the light within the particle. These assumptions define the limits over which anomalous diffraction theory may be accurately applied:

- (i) The refractive index m of the particle is close to that of the medium m , i.e. $m-1 \ll 1$.
- (ii) The size of the particle is large compared to the wavelength of the illuminating radiation, i.e. $x \gg 1$.
- (iii) The absorption of the particle is small.

Interference occurs between the scattered wave and the forward incident wave due to the phase shift induced in the scattered wave. By considering the superposition of the incident and scattered waves over the area of the geometric shadow the following expression is obtained,

$$C_{\text{scat}} = 2 \iint_{x \gg 1} [1 - \cos \phi(x, y)] dx dz.$$

Where $\phi(x, y)$ is the phase shift induced in the scattered wave and the (x, y) plane is parallel to the plane of the advancing optical wavefront.

Champion et al. [58] have calculated expressions for the scattering cross-sections of octagonal particles of axis ratio 10:1 for face, side and edge-on illumination.

Side-on;

$$x_1 = \frac{1}{2} \sqrt{\frac{1}{2} \left(\frac{1+t}{\sqrt{2}} \right)} kd, \quad C_1 = \frac{1+\sqrt{2}}{2x_1} \left[1 + \frac{1}{A} \cdot \frac{\sin A}{1+\sqrt{2}} \frac{-\sin \rho_1 - \cos \rho_1}{\rho_1} \right]$$

where $\rho_1 = 2(m-1)x_1$,

Edge-on;

$$x_2 = \frac{kt}{2}, \quad C_2 = \frac{2kV(1 + \sin(\rho_2/\sqrt{2}) - \frac{\sin \rho_2}{(\sqrt{2}-1)\rho_2} - \frac{(\sqrt{2}-1)\sin \rho_2}{\rho_2})}{x_2}$$

where $\rho_2 = 2(m-1)x_2$.

Face-on;

$$x_3 = \frac{kt}{2}, \quad C_3 = \frac{kV(1 - \cos 2(m-1)x_3)}{x_3}$$

Where; k = the wave number, $2\pi n/\lambda$,

λ = the wavelength of the illuminating radiation,

V = the volume of a single particle,

t = the thickness of the particle,

d = the diameter of the particle = $10t$.

Reasonable agreement between experimental observations and theoretical predictions of C_{ext} (using the above equations) was noted by Champion et al., (who also noted that the side-on and edge-on theoretical values of C_{ext} were graphically identical). A BBC Basic programme was written to run on a BBC model B microcomputer to calculate C_{ext} as a function of particle size for both edge-on and face-on particles. The programme results were found to be in excellent agreement with those of Champion et al. The results for

edge-on and face-on particles were used to calculate a scattering cross-section for randomly orientated particles using the expression,

$$C_r = \frac{1}{3}(C_1 + C_2 + C_3),$$

where; C_r = the average scattering coefficients for a group of randomly orientated particles.

(ii) Programme listing.

```

10 @% = #030406
20 PRINT "INPUT WAVELENGTH": INPUT WV
30 PRINT "INPUT REF. INDEX OF PARTICLE": INPUT M2
40 PRINT "INPUT REF. INDEX OF MEDIUM": INPUT M1
50 K = 2*PI*M1/WV
60 M=M2/M1
70 CLS
80 strt = 0.01E-6
90 stp = 1E-6
100 step = 0.01E-6
110 PRINT TAB(1);"DIA.";TAB(9);C(FACE);TAB(19);"C(EDGE)";
    TAB(28);"C(RAN)"
120 FOR T = 0 TO stp STEP step
130   V = T*PI*(T*5)*(T*5)
135
140   X3 = 0.5*K*T
150   C3 = 2*(K*V/X3)*(1-COS(2*(M-1)*X3))
160
170   X2 = 0.5*SQR(0.5*(1+1/1.414))
180   R2 = X2*K*10*T
190   R2 = 2*(M-1)*X2
200   C2 = (K*V*(2.414)/(2*X2))*(1+(1/R2)*SIN(R2/2.414))-SIN(R2)/
    R2-COS(R2)/(2.414)
210
220   CR = (C3+2*C2)/3
230
240   PRINT TAB(0);T*10;TAB(8);C3;TAB(18);C2;TAB(28);CR
250 NEXT T

```

References.

1. Duffin, W.J., *Electricity and magnetism*, 2nd edition, McGraw Hill, London, (1973).
2. Kerker, M., *The scattering of light and other electro-magnetic radiation*, Academic Press, London (1969).
3. Van de Hulst, H.C., *Light scattering by small particles*, John Wiley, New York, (1957).
4. Born, M. and Wolf, E., *Principles of optics*, 6th edition, Pergamon Press, Oxford, (1985).
5. Bohren, C.F., *Multiple scattering of light and some of its observable consequences*, *Am. J. Phys.*, 55, pp 524, (1987).
6. Van Olphen, H., *Introduction to colloid chemistry*, John Wiley, New York, (1963).
7. Street, N., *The rheology of kaolinite suspensions*, *Australian J. Chem.*, 9, pp 467, (1956).
8. Van Olphen, H., *Clay colloid chemistry*, John Wiley, New York, (1963).
9. Molloy, P.J., *Optical properties of concentrated dispersions*, Ph.D. Thesis (C.N.A.A.), City of London Polytechnic, (1986).
10. Norrish, K., *The swelling of montmorillonite*, *Disc. Farad. Soc.*, 18, pp 120, (1954).
11. Killey, A.K., Meeten, G.H., and Senior, M., *Optical extinction and refraction of concentrated latex dispersions*, *J. Chem. Soc., Faraday II*, 77, pp 587, (1981).
12. Champion, J., Meeten, G.H. and Senior, M., *J. Chem. Soc., Refractive index of particles in the colloidal state*, *Faraday Trans. II*, 74, pp 1319, (1978).
13. Bohren, C.F. and Huffman, D.R., *Absorption and scattering of light by small particles*, John Wiley, New York, (1983).
14. Wickramasinghe, N.C., *Light scattering applications for small particles*, Adam Hilger, London, (1973).
15. Blevin, W.R. and Brown, W.J., *Light-scattering properties of pigment suspensions*, *J. Opt. Soc. Am.*, 51, pp 975, (1960).
16. Brinkworth, B.J., *A scattering efficiency factor for radiative transport*, *J. Phys. D: Appl. Phys.*, 5, pp 476, (1972).
17. Irvine, W.M., *The asymmetry of the scattering diagram of a spherical particle*, *Bull. Astron. Inst. Neth.*, 17, pp 176, (1963).

18. Irvine, W.M., Light scattering by spherical particles: radiation pressure, asymmetry factor, and extinction cross-section, *J. Opt. Soc. Am.*, 55, pp 16, (1964).
19. Mehta, K.T., Estimation of the Kubelka-Munk scattering coefficients from single particle scattering parameters, *Dyes and Pigments*, 5, pp 329, (1984).
20. Brinkworth, B.J., Interpretation of the Kubelka-Munk coefficients in reflection theory, *Appl. Opt.*, 11, pp 1434 (1972).
21. Gate, L.F., Comparison of the photon diffusion model and Kubelka-Munk equation with the exact solution of the radiative transport equation, *Appl. Opt.*, 13 pp 236, (1974).
22. Mudgett, P.S. and Richards, L.W., Multiple scattering calculations for technology, *Appl. Opt.*, 10, pp 1485, (1971).
23. Graaf, R., Aarnoudse, J.G., de Mul, F.F.M. and Jentink, H.W., Light propagation parameters for anisotropically scattering media based on a rigorous solution of the transport equation, *Appl. Opt.*, 28, 12, pp 2273, (1989).
24. Meador, W.E. and Weaver, W.R., Diffusion approximation for large absorption in radiative transfer, *Appl. Opt.*, 18, 8, pp 1204, (1979).
25. Groenhuis, R.A.J., Ferwerda, H.A. and Ten Bosch, J.J., Scattering and absorption by turbid materials determined from reflection measurements. 1: Theory, *Appl. Opt.*, 22, 16, pp 2456, (1983).
26. Taitelbaum, H., Havlin, S. and Weiss, G.H., Approximate theory of photon migration in a two-layer medium, *Appl. Opt.*, 28, 12, pp 2245, (1989).
27. Bonner, R.F., Nossal, R., Havlin, S. and Weiss, G.H., Model for photon migration in turbid biological media, *J. Opt. Soc. Am. A*, 4, 3, pp 423, (1987).
28. Nossal, R., Kiefer, J., Weiss, G.H., Bonner, R., Taitelbaum, H. and Havlin, S., Photon migration in layered media, *Appl. Opt.*, 27, 16, pp 3382, (1988).
29. Keijer, M., Star, W.M. and Storchi, P.R.M., Optical diffusion in layered media, *Appl. Opt.*, 27, 9, pp 1820, (1988).
30. Kubelka, P. and Munk, F., *Z. Tech Phys.*, 12, pp 593 (1931).
31. Kubelka, P., New contributions to the optics of intensely light-scattering materials. Part I, *J. Opt. Soc. Am.*, 38, pp 448, (1947).
32. Judd, D.B. and Wyszecki, G., *Color in business science and industry*, John Wiley, New York, (1952).

33. Baertleson, C.J. and Grum, F., Optical radiation measurements, Vol. 2, Academic Press, London, (1980).
34. Ross, W.D., Theoretical computation of light scattering power, J. Paint Tech., 43, pp 50 (1971).
35. Latimer, P. and Noh, S.J., Light propagation in moderately dense particle systems: a reexamination of the Kubelka-Munk theory, Appl. Opt., 26, 3, pp 514, (1987).
36. Chandasekhar, S., Radiative transfer, Dover, New York, (1960).
37. Wolf, E., (editor), Progress in optics, Vol. 3, North-Holland publishing company, Amsterdam, (1964).
38. Schuster, A., Radiation through a foggy atmosphere, Astrophys. J., 21, pp 1, (1905).
39. Abramowitz, M. and Stegun, I.A., Handbook of mathematical functions, Dover, New York, (1965).
40. Meeten, G.H., Optical properties of polymers, Elsevier, London, (1986).
41. Gate, L.F., The determination of light absorption in diffusing materials by a photon diffusion model, J. Phys. D: Appl. Phys., 4, pp 1049, (1971).
42. Gate, L.F., Light scattering in microporous materials using a photon diffusion model, J. Phys. D: Appl. Phys., 5, pp 837, (1971).
43. Ishimaru, A., Wave propagation and scattering in random media, Vols I and II, Academic Press, London, (1978).
44. Brinkworth, B.J., On the theory of reflection by scattering and absorbing media, J. Phys. D: Appl. Phys., 4, pp 1105, (1971).
45. Fiddick, R.J., North, A.N. and Meeten, G.H., A variable-pathlength optical cell with no moving parts, J. Phys. E: Sci. Instrum. 21, pp 1033, (1988).
46. Nemoto, S., Illumination distribution produced by a fibre bundle, Appl. Opt., 23, pp 2859, (1984).
47. Birkett, R.J., Clark, A. and Meeten, G.H., The effects of cell windows on the optical reflectance of diffusely-scattering materials, Colloids and Surfaces, 24, pp 259, (1987).
48. Borsboom, P.C.F. and ten Bosch, J.J., Fiber optic scattering monitor for use with bulk opaque material, Appl. Opt., 21, pp 3531, (1982).
49. Longhurst, R.S., Geometrical and physical optics, 2nd edition, Longman, London, (1967).

50. Blevin W.R. and Brown, W.J., Effect of particle separation on the reflectance of semi-infinite diffusers, *J. Opt. Soc. Am.*, 51, pp 129, (1961).
51. Churchill, S.W., Clark, G.C. and Sliepcevich, C.M., Light-scattering by very dense monodispersions of latex particles, *Faraday Disc. Chem. Soc.*, 30, pp 192, (1960).
52. Gate, L.F., Light-scattering cross-sections in dense colloidal suspensions of spherical particles, *J. Opt. Soc. Am.*, 63, pp 312, (1973).
53. Hiltner, P.A. and Kreiger, I.M., *J. Phys. Chem.*, 73, pp 2386, (1969).
54. Fitzwater, S. and Hook, J.W., Dependent scattering theory: A new approach to predicting the scattering in paints, *J. Coat. Tech.*, 57, pp 39, (1985).
55. Candau, F. and Ottewill, R.H. (editors), Scientific methods for the study of polymer colloids and their applications, NATO ASI series, series C: Vol 303, pp 247-267, (1990).
56. Ottewill, R.H. and Rowell, R.L. (editors), *Colloid science*, Academic Press, London, (1982).
57. Champion, J.V., Meeten, G.H. and Moon, B.R., Flow turbidity in colloidal kaolinite dispersions, *J. Chem. Soc., Farad. Trans. II*, 75, pp 767, (1979).
58. Moon, B.R., Ph.D. Thesis (C.N.A.A.), City of London Polytechnic, (1978).
59. Champion, J.V., Meeten, G.H., Moon, B.R. and Gate, L.F., Optical extinction of randomly orientated and shear flow orientated colloidal kaolinite particles, *J. Chem. Soc., Farad. Trans. II*, 75, pp 780, (1979).
60. Edsall, J.T., *Advances in colloid science*, Interscience Publishers, New York, (1942).
61. Gate, L.F., (English China Clays International), Private communication, (1990).
62. Jerrard, H.G., Turbulence in apparatus for measurement of streaming double refraction, *J. Appl. Phys.*, 21, pp 1007, (1950).
63. Welzen, J.T.A.M., Stein, H.N., Stevels, J.M. and Siskens, C.A.M., The influence of surface-active agents on kaolinite, *J. Coll. Int. Sci.* 81, 2, pp 445, (1980).

THE BRITISH LIBRARY DOCUMENT SUPPLY CENTRE

TITLE

AN EXPERIMENTAL INVESTIGATION OF DIFFUSE OPTICAL SCATTERING FROM STATIONARY AND FLOWING DISPERSIONS

AUTHOR

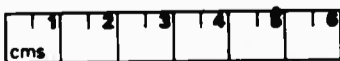
Peter Robert Wood

INSTITUTION
and DATE

City of London Polytechnic
London EC3 1991. C.N.A.A.

Attention is drawn to the fact that the copyright of this thesis rests with its author.

This copy of the thesis has been supplied on condition that anyone who consults it is understood to recognise that its copyright rests with its author and that no information derived from it may be published without the author's prior written consent.



THE BRITISH LIBRARY
DOCUMENT SUPPLY CENTRE
Boston Spa, Wetherby
West Yorkshire
United Kingdom

REDUCTION X ²⁰

CAMERII 2.

DX

96117